CATALYTIC REACTIVITY AND SURFACE INTERACTIONS DURING EARLY STAGES OF SINGLE-WALLED CARBON NANOTUBE FORMATION

A Dissertation

by

MAURICIO CARVAJAL DIAZ

Submitted to the Graduate and Professional School of
Texas A&M University
in partial fulfillment of the requirements for the degree of

DOCTOR OF PHILOSOPHY

Chair of Committee,	Perla B. Balbuena
Committee Members,	Sarbajit Banerjee
	Micah J. Green
	Jorge Seminario
Head of Department,	Arul Jayaraman

December 2021

Major Subject: Chemical Engineering

ABSTRACT

Critical elements in the controlled production of single-walled carbon nanotubes (SWCNTs) methods include the substrate, the catalyst metal particle, and the carbon precursor gas feed. This research targets some of the unanswered questions and hidden relations between the components of the nanotube-particle-substrate system. Highly accurate molecular simulations, along with new experimental observations and the use of high-resolution transmission electron microscopy (HRTEM), have opened the door for a deeper understanding of nanotube formation mechanisms. This dissertation proposes a new theoretical model to explain the intrinsic tube-particle diameter relation and its applicability in various experimental setups. Additionally, new work presented here explains distinct scenarios that may break the tube-particle correlation and shows oxygen as an SWCNT nucleation promoter. Finally, we expose the effect of composition fluctuations on cobalt catalyst particles reactivy using the meta-stable cobalt carbide phases. We observed that the structure-evolving catalyst particle during carbon deposition is a unique environment far from equilibrium where surface reactions and diffusion kinetics may quickly move the scale between inactive and active surfaces.

DEDICATION

To my mom, Edda C. Diaz, my sister, Jennifer A. Carvajal, and my love,

J. Enrique S. Cadena for their unconditional support.

ACKNOWLEDGEMENTS

First, I want to thank my advisor and committee chair, Dr. Perla Balbuena, for their guidance, mentorship, and support from the beginning of my doctoral studies and throughout the development of this research. I'm proud of being a member of her research group and working with all the remarkable scientists and human beings that are part of it and collaborate with us. I have gained invaluable friendships and knowledge interacting with every one of them.

I would like to thank my committee members, Dr. Sarbajit Banerjee, Dr. Micah J. Green, and Dr. Jorge Seminario, for their time and input discussing my research. In addition, special thanks to my former mentors: Dr. James C. Holste and Dr. Kenneth Hall, for inviting me to their research group at Texas A&M University and incentivizing me to start this journey as a member of the aggie family; My friend Dr. Diego Cristancho, for making me aspire to be a great scientist; And, my sister Dr. Jennifer A. Carvajal Diaz, for being a role model of professionalism and endurance.

Infinite thanks to my mother for her unconditional support, love, and encouragement throughout every moment of my life. To my soon-to-be husband, J. Enrique S. Cadena, all my gratitude for his help and patience during long nights of working in this document, and specially for giving me a renewed strength to see this work finished. Finally, thanks to my friends and colleagues and the Department of Chemical Engineering's faculty and staff for making my time at Texas A&M University a great experience.

CONTRIBUTORS AND FUNDING SOURCES

Contributors

This work was supervised by a dissertation committee consisting of Professors Perla B. Balbuena (advisor), Micah Green, and Jorge Seminario of the Department of Chemical Engineering and Professor Sarbajit Banerjee of the Department of Chemistry.

TEM atomic resolution images of SWCNT growth and analyses presented in Chapter I were provided by our collaborators, Dr. Renu Sharma and her team, from the Center for Nanoscale Science and Technology at the National Institute of Standards and Technology (NIST).

All other work conducted for the dissertation was completed by the student independently.

Funding Sources

Graduate study was supported in part by a teaching fellowship from the Department of Chemical Engineering at Texas A&M University.

This work was also made possible by the U.S. Department of Energy, Basic Energy Sciences under Grant Number DE-FG02-06ER15836 and Grant Number DE-SC00193979. Its contents are solely the responsibility of the authors and do not necessarily represent the official views of the U.S. Department of Energy, Basic Energy Sciences.

NOMENCLATURE

SWCNTs	Single-walled carbon nanotubes
TEM	Transmission Electron Microscopy
CNTs	Carbon Nanotubes
MWCNTs	Multiwalled Carbon Nanotubes
CVD	Chemical Vapor Deposition
VSS	Vapor-Solid-Solid
VLS	Vapor-Liquid-Solid
FC-CVD	Floating Catalyst CVD Process
VPE	Vapor Phase Epitaxy
VANTAs	Vertically Aligned SWCNT Arrays
DFT	Density Functional Theory
AC	Armchair
ZZ	Zigzag
HF	Hartree–Fock
KS	Kohn and Sham
DOS	Density of States
vDW	Van Der Waals
LDA	Local Density Approximation
GGA	Generalized Gradient Approximation
XC	Exchange-Correlation

PAW	Projector Augmented Waves
NEB	Nudged Elastic Band
MEP	Minimum Energy Pathway
CINEB	Climbing-Image Method
PBC	Periodic Boundary Condition
PP	Pseudo Potential
FFT	Fast Fourier Transformation
PBE	Perdew-Burke-Ernzerhof
PAW	Projector Augmented Wave
ML	Monolayer
CDD	Charge Density Difference
FTS	Fischer–Tropsch Synthesis
BJ	Becke-Jonson
VASP	Vienna Ab Initio Simulation Package
MD	Molecular Dynamics

TABLE OF CONTENTS

Page

ABSTRACT ii

DEDICATION iii

ACKNOWLEDGEMENTS iv

CONTRIBUTORS AND FUNDING SOURCES v

NOMENCLATURE vi

TABLE OF CONTENTS viii

LIST OF FIGURES xi

LIST OF TABLES xvi

CHAPTER I INTRODUCTION 1

1.1 Motivation 1
1.2 Synthesis of SWCNTs 2
1.2.1 Catalyst Nanoparticles 3
1.2.2 Precursor Gas Chemistry 5
1.2.3 The Role of Oxide Metal Substrates 6
1.2.4 Growth from Molecular Seeds 7
1.2.5 Surface-bound SWCNTs 8
1.2.6 Vertically Aligned SWCNTs 8
1.3 Chirality and Diameter Control 9
1.4 Dissertation Outline 11

CHAPTER II COMPUTATIONAL METHODS AND THEORY 14

2.1 First-principles calculations 14
2.2 Density Functional Theory 15
2.2.1 Electron Density 15
2.2.2 Hohenberg–Kohn Theorems 16
2.2.3 Kohn-Sham Method 18
2.2.4 Ground State Energy from Kohn-Sham Equations 20
2.2.5 Total Energy and Other Properties 23

2.2.6 Van der Waals Forces....23
2.2.7 Hubbard (U) Correction....24
2.3 Exchange Correlation Functionals....24
2.4 Pseudopotential Approach....27
2.5 The Nudged Elastic Band (NEB)....27
2.6 DFT Limitations....28

CHAPTER III CAN SINGLE-WALLED CARBON NANOTUBE DIAMETER BE DEFINED BY CATALYST PARTICLE DIAMETER?....30

3.1 Introduction....30
3.1.1 Theoretical Background and Model Development....32
3.1.2 Dimensional Analysis....36
3.2 Methodology....40
3.2.1 Graphene-Metal Interaction and Evaluation of Model Parameters....44
3.3 Results....46
3.3.1 Probability Distribution Function....47
3.3.2 Test of the Model for the Small Particle Range (d_p < 5nm)....48
3.3.3 Prediction of SWCNT Diameter Distribution....53
3.4 Stability Analysis....54
3.5 Conclusions....58

CHAPTER IV ON THE ROLE OF SURFACE OXYGEN DURING NASCENT CARBON CAP SPREADING AND SINGLE-WALLED NANOTUBE NUCLEATION ON IRON CATALYSTS....61

4.1 Introduction....61
4.2 Methodology....62
4.3 Results....66
4.3.2 Evolution of a Spreading Carbon Shell....70
4.3.3 Energy Corrections and Chirality....73
4.4 Conclusions....75

CHAPTER V EFFECT OF COBALT CARBIDE BULK AND SURFACE COMPOSITION ON THE CATALYST REACTIVITY DURING SWCNT FORMATION....77

5.1 Introduction....77
5.2 Methodology....79
5.3 Results....81
5.3.1 Dissociation Reactions....84
5.3.2 Boudouard Reaction....92
5.3.3 SWCNT – Catalyst interactions....94
5.4 Conclusions....97

CHAPTER VI CONCLUSIONS AND FUTURE DIRECTIONS 99
REFERENCES.....104
APPENDIX A SUPPLEMENTAL INFORMATION CHAPTER III.....138
APPENDIX B SUPPLEMENTAL INFORMATION CHAPTER IV.....140
APPENDIX C SUPPLEMENTAL INFORMATION CHAPTER V 141

LIST OF FIGURES

Page

Figure 1.1. Simulated structure of a nucleated cap system (green/orange) growing over a nanocatalyst (blue) supported on an oxygen-rich insulating substrate ($\boldsymbol{e.g.\ SiO2}$, $\boldsymbol{Al2O3}$). [Top-Right] Nucleated semi-fullerene cap. [Bottom-Right] Curved tubular nanoribbon (orange) at the SWCNT open-end interacting with the catalyst. Reprinted with permission from Diaz et al.[39].....4

Figure 2.1. Typical DFT procedure by iterative self-consistent loop. Modified from Lee (2011).[151].....22

Figure 3.1. ETEM images of SWCNTs growing on Co particles. a - b) Tube diameter smaller than particle diameter, apparent perpendicular growth; c and d) Tube diameter very close to the particle diameter, apparent tangential growth; e) Tube diameter larger than particle diameter, apparent tangential growth; f) Observed correlation between tube diameter and particle diameter. Taken from Diaz et al. [39].....31

Figure 3.2. The laminar sheet of graphene was bent to form a tubular ribbon. 34

Figure 3.3. Cylindrical carbon nanoribbon interacting with a catalyst. The nanoribbon interacts with the catalytic surface and positions itself at an average equilibrium distance $\boldsymbol{\delta 0}$ at the most stable diameter $\boldsymbol{dT}$. For a stable particle with a diameter $\boldsymbol{dp}$, the tube diameter $\boldsymbol{dT}$ is constrained within a diameter range described in Eq. 3.5 as the extension of phase's radial limits. 34

Figure 3.4. Approximations for the model using dimensional analysis. Expressions for $\mathbf{fd}$ and $\mathbf{< dT >}$ were obtained using both extreme scenarios. 39

Figure 3.5. Top and side views for the metal–graphene systems using [100] metal slabs. The black rectangle at the top view corresponds to the periodic unit area, $\boldsymbol{a0}$ and $\boldsymbol{a1}$ are vectors conforming the shape of the simulation box.....41

Figure 3.6. Top and side views for the metal–graphene systems using [111] metal slabs. The black parallelogram at the top view corresponds to the periodic unit area, $\boldsymbol{a0}$ and $\boldsymbol{a1}$ are vectors conforming the shape of the transversal area.....41

Figure 3.7. Test for optimizing the initial lattice vectors $\mathbf{a0}$, $\mathbf{b0}$ in the [100] system. The 0.7 – 1.2 range was tested for the ratio $\mathbf{a0/ac}$, where $\mathbf{ac}$ corresponds to the graphene lattice vector (0.246 nm). 43

Figure 3.8. Surface carbon density ($\boldsymbol{\rho s}$) dependence on chiral angle. Estimated values (•) using periodic units of different chiral tubes. 45

Figure 3.9. Probability distribution $\mathbf{fd}$ using optimized parameters for a cobalt particle. [Left] Probability distribution function ($\mathbf{fd}$) for different particle curvatures (e.g., 1 nm to 5 nm). [Right] Cumulative distribution function. The probability of obtaining a 4 nm diameter tube using different particle sizes (4 nm and 5 nm) is calculated for this scenario. 48

Figure 3.10. Adjusting the parameter $\boldsymbol{\alpha}$ to our SWCNT experimental data. (+) High-resolution TEM experimental data from Diaz et al[39]. (−) Most probable or average diameter and (--) standard deviation limits ($\pm\boldsymbol{\sigma}$) obtained after $\boldsymbol{\alpha opt}$ has been found. 49

Figure 3.11. Adjusting the parameter $\boldsymbol{\alpha}$ to inner diameters in the MWCNTs experimental data[39]. (x) Data collected for iron particles from Tibbets[137]. (−) The most probable or average diameter and (--) standard deviation limits ($\pm\boldsymbol{\sigma}$) obtained after $\boldsymbol{\alpha opt}$ has been found. 51

Figure 3.12. SWCNT's diameter distribution prediction using Iron catalyst particle profiles measured by Zou et al[132]. Figure 3.12 a-c corresponds to the experimental tube diameter distribution profile (orange) vs the model's prediction (blue). Predictions were based on experimental catalyst particle diameters for particles (a) without etching and (b and c) after 10 s to 15 s of etching, respectively. The darkest colored regions show the overlap between the experimental and the theoretical descriptions. 53

Figure 3.13. Stability analysis for the nucleation of carbon allotropes on metal catalysts. Empirically fitted functions for the curvature energy in SWCNTs (E_{cT}) and fullerenes (E_{sF}) and the critical diameter of transition (d_c) for a cobalt catalyst. 55

Figure 3.14. Diameter stable regions during the growth process of SWCNTs and high probability zones within one standard deviation from the most probable diameter ($< \mathbf{dT} > \pm\boldsymbol{\sigma}$). (+) High-resolution TEM experimental Data for Co catalysts. (--) Upper limit for the radial extension of phase ($\mathbf{dup}$). (···) Transition critical diameter ($\mathbf{dc}$) between stable fullerene and tube allotropes. (−) Most probable or average diameter and standard deviation limits ($\pm\boldsymbol{\sigma}$). In the purple region, the probability of finding a diameter d_T is ≈ 0. 56

Figure 4.1. Fe (110) Slab with five layers, the graphitic carbon shell corresponds to the pre-nucleated cap of a (5,5) AC tube. [a-d] Initial possible positions for the oxygen atom location before relaxation. Color code for atoms: surface

O: red, surface Fe: orange; subsurface Fe: pink. The central pentagon and C atoms connecting the pentagon to the cap edge: maroon; hexagon edge atoms: light blue. 63

Figure 4.2. [Top] Oxygen atom positions after each addition cycle. We selected the structure with the strongest O-surface interaction energy after each new addition. [Bottom] Interfacial energy per oxygen atom after increasing oxygen concentration;(◊) Interaction O-surfaceenergy for all possible oxygen configurations; (▲) Strongest O-surface interaction energy . Color code for O and Fe atoms as in Figure 4.1. 65

Figure 4.3. Top: Pre-nucleated shell interacting with two oxygen-rich Fe (110) surfaces. S1 and S2 differ in the adsorbed C:O ratio, with 0:1 and 1:1, respectively. Bottom: [a] Interfacial energy per carbon in the rim for both surfaces. [b] Average charge of the metal surface and carbon atoms in the shell for S1. [c] Direct C_{rim}-O interaction at 0.24 ML, atomic position, charge, and CDD are shown 67

Figure 4.4. Charge density difference and Bader Analysis of the S1 oxidized surfaces. The color shows the Badder charge of all atoms in a range of -1.13 $\mathbf{e}-$ to 0.78 $\mathbf{e}-$ using a scale from blue to red respectively, where the O atoms present the highest electron charge ($\approx$ 1.1 $\mathbf{e}-$) and the oxidized Fe atoms the lowest. The closest carbon-oxygen distance ($\mathbf{dO-C}$) for eah system is highlighted on a yellow circle. Color Code for the CDD: yellow: electron depletion; cyan: accumulation. 69

Figure 4.5. Crim – Oxygen bonds at 0.2 ML O concentration. Three C-O bonds are formed (above 0.16ML concentration) causing interfacial energy stabilization and charge transfer. 70

Figure 4.6. Carbon shell spreading on a reduced and partially oxidized (0.16 ML) iron surface.[Top] The structure evolves to a pentagon-rich and then hexagon-rich edge after increasing the amount of carbon in the active area. Side view only includes the first two upper iron layers and the carbon shell. [Bottom] Interfacial energy evolution during the different stages of spreading and cap formation..... 71

Figure 4.7. Stages of a SWCNT formation.[Top] Evolution from a carbon shell to AC or ZZ SWCNTs. [Bottom] Interfacial energy ($\boldsymbol{EInt/Crim}$) between carbon structures and iron surfaces, the PBE no dispersion (PBE-ND) energy and dispersion force corrections are shown. 74

Figure 5.1. Cobalt carbide slabs and adsorption sites used in the precursor gas reaction calculations. Co_2C (011) and Co_3C (111) correspond to the Co-top surface termination. Co_2C (011) and Co_3C (020) correspond to the CoC-top

termination. Color code: surface Co: orange; subsurface Co: pink. Carbon: grey. 80

Figure 5.2. CO adsorption site at the strongest interaction with the cobalt carbide surface. Color code: surface Co: orange; subsurface Co: pink. Carbon: grey. Oxygen: red. 82

Figure 5.3. C_2H_2 adsorption site at the strongest interaction with the cobalt carbide surface. Color code: surface Co: orange; subsurface Co: pink. Carbon: grey. Hydrogen: white. 83

Figure 5.4. Reaction pathway for the dehydrogenation reaction of C_2H_2 on Co_2C. [Top] H-C dissociation reactions and the C-C bond breaking for the Co_2C(011) with Co-top termination. [Bottom] H-C dissociation reactions and the C-C bond breaking for the Co_2C (011) with CoC-top termination. Color code: surface Co: orange; subsurface Co: pink. Carbon: grey. Hydrogen: white. 86

Figure 5.5. Reaction pathway for the dehydrogenation reaction of C_2H_2 on Co_3C. [Top] H-C dissociation reactions and the C-C bond breaking for the Co_3C(111) with Co-top termination. [Bottom] H-C dissociation reactions and the C-C bond breaking for the Co_3C (020) with CoC-top termination. Color code: surface Co: orange; subsurface Co: pink. Carbon: grey. Hydrogen: white. 87

Figure 5.6. Activation and reaction energies for the dehydrogenation of C_2H_2 on Co2C(011) with Co-top and CoC-top terminations, Co3C(111)-Co-top and Co3C(020)-CoC-top terminations. The relative energy values were calculated with respect to the initial system energy. 88

Figure 5.7. Charge distribution of C_2H_2 on top cobalt carbide during the first H-C dissociation. The darker-red color corresponds to positively charged atoms, and the light-yellow color corresponds to the negatively charged atoms.....89

Figure 5.8. [Top] Activation (Ea) and reaction energies ($\boldsymbol{\Delta Grxn}$) for C-O dissociation. [Bottom] a.) CO dissociation reaction mechanism on Co2C and Co3C surfaces; b.) Charge distribution during the C-O bond breaking. Color code: surface Co: orange; subsurface Co: pink. Carbon: grey. Oxygen: red. 91

Figure 5.9. [Top] Activation (Ea) and reaction energies ($\boldsymbol{\Delta Grxn}$) for CO disproportionation. [Bottom] a.) CO disproportionation reaction mechanism on Co2C and Co3C surfaces; b.) Charge distribution during the C-O bond breaking. Color code: surface Co: orange; subsurface Co: pink. Carbon: grey. Oxygen: red. 93

Figure 5.10. AC(5,5) and ZZ(9,0) SWCNTs interacting with Co_2C and Co_3C carbide surfaces. 95

Figure A.11. Reduced functions obtained for the case ($\boldsymbol{\beta / dup \gg 1}$) scenario in the dimensional analysis. Both approximations were compared against Tibbets's experimental set (Right) and Diaz et al. experimental data (Left)..138

Figure A.12. Reduced functions obtained for the second case ($\boldsymbol{\beta dup \ll 1}$) scenario in the dimensional analysis. Both approximations were compared against Tibbets's experimental set (Right) and Diaz et al. experimental data (Left)..138

Figure A.13. Optimization of the parameter $\boldsymbol{\alpha}$. (+) High-resolution TEM experimental Data from Diaz et al[39]. (x) Data collected from Tibbets[137]. A comparison between the optimized value $\boldsymbol{\alpha opt}$ and the value from Gulseren et al[181] is shown. 139

Figure B.14. Initial Calibration of the Hubbard U Parameter. [Left] Bulk structure of Iron Oxide. [Right] Lattice and Bulk energy error using different U values. 140

Figure C.15. Different tested adsorption sites for acetylene and CO.....141

LIST OF TABLES

Page

Table 2.1. Typical exchange-correlation functionals commonly used in DFT calculations. 26

Table 3.1. Metal slabs parameters for the modeled system. 40

Table 3.2. Percentage of change from the graphene lattice constant due to mismatch with the metal slab. 42

Table 3.3. Metal structure effect in the interaction energy between catalyst and graphene. Adhesion Energy, Metal-Carbon interaction, and equilibrium distance are calculated for [100] and [111] metal surfaces. 46

Table 5.1. Lattice parameters a, b, and c corresponding to the length of unit vectors in the x y plane and z-direction respectively, for the cobalt carbide unit (1x1) cell. 79

Table 5.2. Adsorption Energies (eV) for C_2H_2 and CO on top of cobalt carbide surfaces with (011), (020) and (111) facets and different surface terminations. The corresponding facet is next to the adsorption energy value. 81

Table 5.3. Adsorption energy between C_2H_2 and Co2C(011) with Co-top and CoC-top terminations, Co3C(111)-Co-top and Co3C(020)-CoC-top. The cobalt carbide systems' average charge for bulk and surface (sfc) atoms is tabulated before the dissociation reactions. 89

Table 5.4. Adsorption (Eads), activation ($\boldsymbol{Ea}$), and reaction ($\boldsymbol{\Delta G}$) energies for CO in the cobalt carbide surfaces. 92

Table 5.5. Adsorption (E_{ads}) and interfacial energies (E_{int}) between AC and ZZ SWCNTs and the cobalt carbide surfaces. 96

CHAPTER I

INTRODUCTION

1.1 Motivation

The hollow structures of carbon fiber, referred to as carbon nanotubes (CNTs), were evidenced by transmission electron microscopy (TEM) as early as 1952[1]. It was not until 1991 that Sumio Iijima explained what they were and named them[2]. These needle-shaped structures were revealed to be multiwalled carbon nanotubes (MWCNTs) comprised of coaxial tubes with more than two shells[2]. Carbon nanotubes having a single shell were later synthesized by co-evaporation of transition metal and graphite utilizing the arc-discharge method [3,4]. For the past two decades, single-walled carbon nanotubes (SWCNTs) have been at the forefront of nanotechnology research.[5–7]

The properties of SWNTs are usually described in terms of those of graphene due to their structural similarity. In graphene, each carbon atom is covalently bonded with three other carbon atoms by sp^2 hybridization[8]. Such covalent sp^2 bonds are maintained in SWCNTs, rendering them one of the strongest and stiffest materials discovered thus far[9]. SWCNTs also have tunable electrical and optical properties (i.e., semiconducting or metallic depending on their helical angle).[10,11] Recent innovations and further understanding of the underlying mechanisms behind the synthesis processes are increasing the number of applications in several industries.[12–14] Among the potential uses, the most promising implementations are optoelectronics, sensors, composites, batteries and novel nanoelectronics.[15–17]

It is anticipated that the scaling of complementary silicon metal–oxide–semiconductor (CMOS) devices ends during the next decade[18]. Prototype field-effect transistors (FETs) made from semiconducting SWCNTs demonstrate high mobility, low turn-on voltages, and subthreshold slopes near the thermal limit, which exceeds the properties of modern Si technologies.[19] In 2013, the first computer whose central processor is based entirely on SWCNT-based transistors was fabricated.[20] In 2019, significant progress toward fabricating a commercial chip was made by creating a 16-bit processor.[21] The fabrication of high-performance integrated circuits requires controlling the structural and electronic properties during large-scale production. The difficulties of the SWCNT computer are partly due to the imperfection of the SWCNT materials. Assembling billions of identical SWNTs onto predetermined places on a chip[22] is among the most challenging tasks in the SWCNT research field.

1.2 Synthesis of SWCNTs

The synthesis methods for SWCNTs include arc discharge, laser ablation, and chemical vapor deposition (CVD)[23–25]. CVD has been the most promising in lowering costs and scaling to large production from all of them.[26–29] The continuous gas phase CVD process is a favorite at producing high-quality SWCNTs in large quantities[30], but the products are randomly oriented and contain diverse sets of structures. CVD batch processes are favorable for electronic device applications due to their low cost and increased control over properties.[15,31,32]

The interlocking net of factors that determine the diameter, chirality, number of walls, and nanotubes defects during nucleation and growth is not entirely understood yet.

In CVD methods, the growth environment radically affects the yield, selectivity, and length of SWCNTs. The role of reactive species (including oxidants and promoters), the chemical reaction pathways, and carbon dynamics leading to the effective SWCNT nucleation, growth, and termination are at the frontline of SWCNT research.

1.2.1 Catalyst Nanoparticles

Metal catalyst particles are crucial elements in the formation and nucleation of SWCNTs. Traditionally, iron (Fe), cobalt (Co), nickel (Ni), and their alloys are the catalysts of choice for SWCNT growth[33]. They usually serve as reaction promoters and templates, shaping the final structure of the nanotube.[33,34] In general, transition metals are considered powerful catalysts due to their partially filled *d* orbitals and their ability to dissolve carbon.[35]. For most vapor-solid-solid (VSS) and vapor-liquid-solid (VLS) mechanisms, the precursor gases dissociate or react on the catalyst surface, adding carbon (and other elements) and forming the graphitic seed that evolves toward the SWCNT. Four steps are distinguished during the SWCNT formation: 1. The spreading phase, where the graphitic structure forms and expands, reducing the surface energy until it develops a stable cap with six pentagons;[36] 2. The nucleation, where the "*bulk*" sp^2 carbon shell uplifts from the metal surface, forming a cap, and the new tube's edge dominates the SWCNT/surface interaction (Figure 1.1); 3. The growth phase, where available carbon atoms in the active surface attach to the cap edges via reaction or diffusion, allowing the SWCNT to grow vertically; and 4. Termination, in this step, the carbon feed is interrupted due to catalyst-tube detachment, particle inactivation, or insufficient carbon intake due to a reduction in catalytic reactions.

The structure of catalyst nanoparticles, including size, composition, morphology, and their evolution during the CVD process (e.g., interaction with adsorbate gases and substrate), play a critical role in the growth of SWCNTs[37]. The chemical state of transition metal particles during CNT growth is somewhat a debated subject. For example, the use of carbon oxide mixtures as precursors (CO_x) will allow the dissociative adsorption of carbon and oxygen atoms on the iron surface, creating different combinations of carbides and oxides that alter the composition and structure of the catalyst[38].

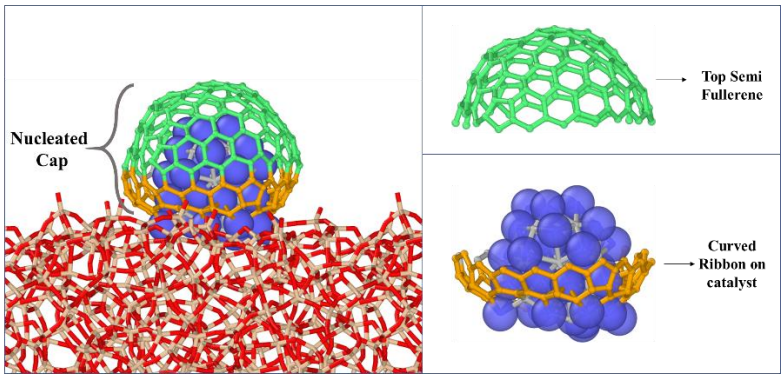

Figure 1.1. Simulated structure of a nucleated cap system (green/orange) growing over a nanocatalyst (blue) supported on an oxygen-rich insulating substrate ($\boldsymbol{e.g.\ SiO_2, Al_2O_3}$). [Top-Right] Nucleated semi-fullerene cap. [Bottom-Right] Curved tubular nanoribbon (orange) at the SWCNT open-end interacting with the catalyst. Reprinted with permission from Diaz et al.[39]

The atomic arrangements of the W_6Co_7 nanocrystals are believed to play key roles in selective SWCNT growth. Under optimized carbon feeding conditions, SWCNTs specific helicities can be synthesized[40]. Another example of high melting-point catalysts is the recent report by Zhang et al.[41], where they demonstrated the growth of *(2m,m)* SWCNTs from Mo_2C and WC nanoparticles. Other strategies for controlling the SWCNTs structure include: Perturbing the growth temperature to tune the tube-catalyst

interface,[42] tuning the catalyst–support interaction[43], such as Fe, Co, and Ni nanoparticles on MgO supports, to grow high chiral angle SWCNTs[44–46], and influencing particle surface reconstruction by the adsorption of gases such as water vapor[47].

1.2.2 Precursor Gas Chemistry

While researchers have analyzed the impact of catalyst and catalyst/substrate interactions on the resultant SWCNT product, less attention has been devoted to the carbon feedstock beyond the hydrocarbon metal solubility and, to some extent, its "cracking" behavior. However, bodies of evidence have emerged over the past decade demonstrating the multiple critical roles of reactive gas feed stocks.

Oxygen-containing species can influence lifetime through oxidative polishing[48], growth temperature by promoting dehydrogenation[49], and diameter control by influencing catalyst sintering behavior[50]. For example, SWCNT synthesis by disproportionation of carbon monoxide ($2CO \rightleftharpoons CO_2 + C$) is one of the most used gas-phase processes nowadays.[30,51] At high pressures, this method is commonly known as the HiPco process,[25] and recently, the low (atmospheric) pressure setup on a CVD reactor has been denominated the floating catalyst CVD process (FC-CVD)[52]. During the FC-CVD approach, iron particles catalyzing the carbon monoxide (CO) dissociation have shown an excellent behavior for controlling narrow diameters[53] and chirality selectivity.[54]

In contrast, hydrocarbons and their reaction products can influence nucleation efficiency, catalyst reduction, CNT alignment, growth rate, and defect density. These last points add support for early arguments[55,56] that specific gas precursors, in particular

those with alkyne moieties (i.e., triple bonds), can incorporate into growing CNTs as intact molecules (*e.g.*, in lengths of C_2, C_4 and possibly larger)[57–61]. While this idea remains central for research efforts, chirality-directing functional groups or heteroatoms could be delivered to preselected locations along the growth axis if side groups attached to an alkyne can be directed into a growing CNT without impacting the lattice stability.[62] This could enable more precise helicity control that is either synergistic or an independent control parameter distinguished from catalyst control alone. Furthermore, this could enable directed defect placement or geometries[63], SWCNTs with various engineered heteroatoms, and SWCNTs that could be covalently modified by wet- or dry-chemical post processing[64]. An important area where the choice of precursor might have a significant impact is toward scale-up and more environmentally benign production of CNTs. Various renewable sources, from naturally occurring materials (oils, biodiesel, food-based products) and vegetable and animal waste products, have proven effective in producing CNTs (mostly MWCNTs). [65]

1.2.3 The Role of Oxide Metal Substrates

The substrate's material, surface morphology, and texture properties affect the SWCNTs' yield and quality. Physical interactions, e.g., Van-der-Waals and electrostatic forces between catalyst and substrate, prevent catalyst particle movement and reduce thermally driven diffusion and sintering of metal particles on the substrate material[66]. The substrate acts as a medium for support in the CVD technique and interacts chemically and physically with the growth environment. The nonreducible oxides are ideal support materials because they are chemically inert and exhibit high-temperature

resistivity. In contrast, reducible oxides made of transition or rare-earth metals plus oxygen have an intrinsic redox potential because the cationic species can change oxidation states. Various substrates used in CVD for the growth of CNT are silicon[67,68], silicon carbide[69,70] graphite[71,72], quartz[32,73], silica[74,75], alumina[76,77], magnesium oxide[78,79], calcium carbonate (CaCO3)[80], zeolite[81] and NaCl[82], etc.

Supported catalytic metal particles have shown greater catalytic reactivity due to charge transfer from the support. An increasing number of theoretical and experimental investigations have suggested that transition metals used as dopants in metal oxide supports induce charge transfer to species adsorbed on the oxide's surface, enhancing chemical reactivity.[83,84] A catalytically active role by the support in the growth of CNT can also explain the success of oxidizers (H_2O or O_2) in enhancing the growth of substrate-based CVD synthesis of SWCNTs.[68]

1.2.4 Growth from Molecular Seeds

A different approach toward chirality control is using a collection of short nanotube "seed" segments with predefined cap structures or chirality.[85] The objective is to elongate these seeds into SWCNTs while preserving the initial helicity (i.e., chiral angle). Early pioneering work demonstrated the use of short Fe-nanoparticle-docked SWCNTs as growth templates and succeeded in growing much longer SWCNTs with unchanged diameters[86]. Later, Liu et al. reported a metal-free growth approach termed "cloning" by using open-ended short nanotube fragments cut from long nanotubes to template SWCNT growth of preserved helicity[87]. Recently, Zhou et al. developed a direct-synthesis approach, named vapor phase epitaxy (VPE)[88], to produce single-

helicity SWCNTs, starting with DNA-separated SWCNT seeds[89,90]. With this metal-free VPE process, seeds of three different chiral SWCNTs, (7,6), (6,5), and (7,7), have been elongated (using methane or ethanol as carbon source) from a few hundred nanometers to tens of micrometers, successfully inheriting the chirality of the nanotube seeds.[85]

1.2.5 Surface-bound SWCNTs

When grown on flat substrates, SWCNTs are generally surface-bound unless the interactions among sufficiently dense SWCNTs force their vertical growth[91,92]. The formation of these surface-bound SWCNTs requires a dispersed distribution of catalyst particles so that forces exerted by the substrates on the SWCNTs can either horizontally align them in parallel to each other or distribute them in a random network. Horizontally aligned arrays of SWCNTs exceed the performance of traditional crystalline channel materials (*e.g.*, silicon, GaAs) in digital[93–99] and analog or radio frequency (RF) electronic[100–102]. On the other hand, random networks of SWCNTs may replace amorphous silicon and organic materials in flexible electronics and flat panel displays[103–108]. Both arrangements of SWCNTs are also considered for use in applications such as transparent electronics[109–111] and bio/chemical-sensors[112–114].

1.2.6 Vertically Aligned SWCNTs

Vertically aligned SWCNT arrays (also called forests, carpets, and VANTAs) are formed by a bottom-up, self-organization process, which renders a hierarchical and anisotropic morphology[115,116]. The multitude of interactions among neighboring CNTs growing in concert causes individual CNTs to self-align. Researchers have been

exploiting this paradigm since 1996[117] to synthesize relatively well-ordered MWCNTs and SWCNTs without requiring post-processing steps, promising to transform a wide range of applications.

SWCNT forests are primarily grown from arrays of catalytic nanoparticles that form via solid-state dewetting upon thermal annealing of a thin metal film. While the support layer controls the physical stability of the catalyst nanoparticles, recent success in controlling CNT diameter through mixtures or alloys of more than one element of the catalyst has encouraged researchers to explore the periodic table beyond the more conventional combinations of Fe/Mo[118,119] and Co/Mo[120–122]. There has even been an exploration into ternary mixtures of Fe/Ni/Cr.[123]

Wafer-scale growth has already been demonstrated in a lab-scale tool.[124] Moreover, Zeon Nano Technology Co. Ltd., recently established an industrial-scale SWCNT production plant.[125] In collaboration with the National Institute of Advanced Industrial Science and Technology (AIST) in Japan, Zeon Corp. has developed a continuous, belt conveyor process to synthesize aligned SWCNTs on flat 50 × 50 cm^2 metal substrates for ton-scale production of long, pure, and high surface area aligned SWCNTs.

1.3 Chirality and Diameter Control

The key to controlling SWCNT's chirality is its hemispherical cap structure and size. The cap is composed of six pentagons whose distribution defines the structure of each nanotube. In the CVD growth of SWCNTs, cap formation on the catalyst is the initial step of nucleation[126,127]. Earlier studies have highlighted the thermodynamics-

driven nature of the SWCNTs nucleation process[128] and its connection with chirality selectivity[129]. For all chiral angles χ, the energy scale variability associated with the SWCNT caps is small compared to that of the SWCNT to catalyst interface[130]. High interfacial surface stress between metal and carbon tends to peel off the cap. This process creates an incipient nanotube nucleus composed of a thin curved tubular nanoribbon interacting with the metal surface and topped by a semi fullerene cap, as shown in Figure 1.1. The nucleation is followed by lift-off and subsequent elongation (growth) of the tube[131].

Parameters that control chirality and diameter of single-walled CNTs (SWCNTs) have been the subject of extensive studies. Generally, narrow small diameter distributions often reflect a high SWCNT chirality selectivity, especially for solid catalyst growth.[34,120] There is some consensus among experimentalists about the diameter-controlled synthesis of SWCNTs grown using a supported nanocatalyst: A uniform distribution of supported small solid catalyst particles is suggested to produce a homogeneous narrow nanotube's diameter distribution[74,132–134]. These works show a strong relationship between the solid nanocatalysts' size and the tube diameter profile. The catalyst phase (i.e. solid or liquid) has been suggested as an important factor for reducing the variability of possible chiral structures[135,136]. Statistical analyses establishing the ratio between the diameters of catalyst particles and those of SWCNTs[53,137,138], together with observations regarding the growth mode, have given birth to additional understanding, such as the tangential vs. perpendicular growth classification[139].

Over the past decade and a half, a growing number of studies analyzing nanotube helicity at the "population" level in various growth experiments indicated a predominance of near-armchair (*n*,*n*-1) types[44,140–144]. These puzzling observations led to a theory of chiral angle-dependent SWCNT growth[145] that reconciles earlier thermodynamic[146] and kinetic[147] arguments.

1.4 Dissertation Outline

Our research's primary goal is to elucidate the tube-particle-substrate system relations and study the interactions that allow the formation of SWCNTs. Further understanding among the reaction components is fundamental for the controlled production of SWCNTs. Chapters I and II give a current state of the SWCNT research and give a context of the theory behind density functional theory (DFT), respectively. This dissertation focuses on three main aspects of the SWCNT synthesis, 1. Nanotube's cap stability, 2. Metal nanoparticle composition and surface, and 3. The precursor gas dissociation.

Chapter III proposes a new theoretical framework based on experimental and computational observations to expand the understanding of nanotube nucleation and diameter selectivity. We used statistical-mechanics tools to correlate the final tube diameter with the potential strain energy stored by the graphitic wall on top of a spherical catalyst particle. The carbon-metal interaction strength, the distance between the graphitic and metal surfaces, and other model parameters were obtained from DFT calculations. Finally, we combined the stability of cap nucleation, the classification of

growth (tangential vs. perpendicular), and our model to expand the current understanding of CNT-particle diameter relation.

Chapter IV analyzes the surface oxygen role in the SWCNT nucleation. Iron catalyst particles show promising results for the controlled-diameter growth, and their apparent independent relation with particle diameter makes them an exciting study case for SWCNT growth. First-principles calculations were used to study the effect of surface oxygen concentration in the SWCNT-metal interaction. Charge distribution and electron density allowed a better understanding of the rim–oxygen bond and its effect on interfacial energy.

Chapter V explores the surface reactivity of metastable cobalt carbide phases. Transition metal particles (e.g., Fe, Ni, Co) often have an evolving bulk and surface composition during the SWCNT nucleation. In this chapter, we studied the differences between two cobalt carbide phases (Co_2C and Co_3C) and their top surface terminations, one rich in Co (Co-top) and the other with adsorbed sub-surface C atoms (CoC-top). It is experimentally reported that cobalt carbide particles have certain preferred crystal planes to nucleate and grow.[148] DFT calculations were used to obtain activation energies for the dissociative reaction of acetylene (C_2H_2) and carbon monoxide (CO). We identified interesting trends involving the bulk composition and surface contributions on the catalyst reactivity during C deposition with the energy barriers and charge distributions. Lastly, we analyzed the interfacial interaction strength between achiral SWCNTs (armchair and Zig-zag) and different combinations of surface termination, bulk composition, and crystal planes.

At last, Chapter VI presents the conclusions of this dissertation, and some future directions are given concerning the work realized.

CHAPTER II

COMPUTATIONAL METHODS AND THEORY

The present dissertation uses molecular modeling and first-principles calculations to study the behavior of multiple gas-catalyst-substrate interactions and reactions involved in the formation of SWCNTs. This chapter described some of the theories, history, and models that are the foundations for the results presented in the following chapters.

2.1 First-principles calculations

Ab initio quantum chemistry has been an essential tool in the study of atoms, molecules, and diverse materials modeling problems in physics, chemistry, and multiple branches of engineering during the last decades.[149,150] The underlying core technology is the computational solution of the electronic Schrodinger equation (eq. 2.1 and 2.2). In its exact form, the electronic Schrodinger equation is a many-body problem whose computational complexity grows exponentially with the number of electrons.[151] The Hamiltonian operator ($\widehat{H}$), is a sum of all energy terms involved and E is the eigenvalue of $\widehat{H}$ associated with the wave function, Ψ.

$$\widehat{H}\Psi(r_i) = E\Psi(r_i) \quad (2.1)$$

$$\widehat{H} = E_{kin} + \sum\nolimits_{i,j} U_{i,j} \quad (2.2)$$

Wavefunction-based approaches expand the electronic wavefunction as a sum of Slater determinants,[152] orbitals, and coefficients optimized by various numerical procedures.[153,154] Hartree–Fock (HF) theory is the simplest method of this type,

involving optimization of a single determinant. HF is a mean-field approach that produces good results for many properties. However, it cannot fully describe reactive chemical events in which electron correlation has a significant role.[149,151] The second class of theoretical approaches is based on density functional theory (DFT). For investigation of reactive chemistry in medium-large systems, DFT is at present the preferred approach [150].

2.2 Density Functional Theory

This method uses the Hohenberg–Kohn theorem[155] to establish the system's total energy as a function of electron density. The electron density depends on only three coordinates instead of the 3N coordinates of N electrons, thus rendering DFT highly attractive for computational implementation. The computational effort required to calculate DFT equations is comparable with that required for Hartree–Fock theory.[149] At present, two principal classes of functionals have been extensively deployed and tested in large-scale applications and small molecule benchmarks: gradient-corrected[156,157] and hybrid functionals[156,158].

2.2.1 Electron Density

The electron density $\rho(r)$ is defined as the number of electrons per volume at the point r in space, and it decides everything in an *n*-electron quantum system. It is a physical quantity, and theoretically, can be measured.[151] In the DFT scheme, we first assume that electrons do not interact with each other. For this noninteracting reference

system with decoupled coordinates, the electron density is written as a simple sum of noninteracting (i.e., occupied) orbitals ϕi:

$$\rho(r) = \sum_{i} |\phi_i(r)|^2 = 2 \sum_{i}^{occupied} |\phi_i(r)|^2 \quad (2.3)$$

The usual wave functions, ψ_i, is replaced by orbitals ϕ_i, implying that ϕ_i are now the so-called Kohn and Sham (KS) orbitals in a noninteracting reference system. In the above equation, each orbital's amplitudes (positive or negative) are converted to a positive density of electrons. If we add up all the electron densities over the entire space, it will naturally return the total number of electrons, n:

$$\int \rho(r) dr = n \quad (2.4)$$

In addition, if we sum up all the overlapping electron densities of atoms, they will accumulate and come closer to the electron densities of solids. For this reason, if we know an atomic electron density, we can approximately generate the electron density for a solid made from that atom. The electron density in a system represents wave function, orbital, and the total number of electrons and is also directly related to potentials, energies, and thus all properties.

2.2.2 Hohenberg–Kohn Theorems

The electron density's decisive role in electronic calculations was subject to formal verification in 1964 when Hohenberg and Kohn finally proved it with two theorems.[155] This theoretical frame provided a sound foundation for the designation of electron density as the key player in the DFT.

The first theorem states that we can find a unique external potential, U_{ext}, solely determined by the ground-state electron density. Therefore, it is evident that there will be a direct relationship between ρ(r) and U_{ext}. The term *external* refers to the fact that the Coulomb attraction by nuclei is external and is thus system-dependent from the electron's viewpoint. Therefore, different external potentials will always generate different electron densities. The system-independent internal potential (i.e., the electronic kinetic energy plus the electron-electron potential) has a universal character, and it can be applied to any other system once it is known. The base of all conventional DFT calculations start with the assumption that we confine our interests only within the ground-state properties of the system. In that case, the sole knowledge of the electronic density at a given external potential is sufficient to deduce the total energy or other properties.

The second theorem identified a method to find the minimum energy of a system. At a given U_{ext}, if we minimize the system energy varying electron density, we will reach the very bottom of the energy well, yet not below it.[151] This is often called the variational principle within the framework of DFT, and therefore the electron density that minimizes the system energy is known as the ground-state electron density, ρ_0:

$$E[\rho(r)] = F[\rho(r)] + E_{ext}[\rho(r)] \geq E_{gs} \quad (2.5)$$

Equation 2.5 offers a very flexible and powerful means of finding the ground-state energy and other properties. One extra point is that the search can start with energy calculated by any educated guess for the electron density. In practice, for a solid, we

usually start with the energy calculated at the electron density generated by overlapping atomic densities.

2.2.3 Kohn-Sham Method

In 1965,[159] Kohn and Sham, constructed a fictitious system of one-electrons whose Hamiltonian operator is shown in equation 2.6. Here, r_i and r_j are coordinates of electrons, and r_I and Z_I are coordinates and charges of the nuclei. Earlier attempts to adopt electron density without any wave functions within the first-principles calculations were not very effective.[160] The main reason is due to the poorly written electronic kinetic energy in terms of electron density.[151]

$$\widehat{H} = -\frac{1}{2}\sum_{i=1}^{n}\nabla_i^2 - \sum_{I=1}^{N}\sum_{i=1}^{n}\frac{Z_I}{|r_i - r_I|} + \frac{1}{2}\sum_{i\neq j}^{n}\frac{1}{|r_i - r_I|} \quad (2.6)$$

In equation 2.6, the first term denotes kinetic energy (E_{kin}), the second term represents external potential ($U_{ext} \rightarrow E_{ext}$), and the last term is the Hartree potential ($U_H \rightarrow E_H$) with a correction factor of 1/2 for double counting. The calculation of the last term covers all cases where $i \neq j$ to exclude any self-interaction. A significant difficulty lies in the last term, the coupled interactions ($U_x \rightarrow E_x$) between all n electrons. This last term contains numerous interactions that are difficult to formulate for calculable equations.

Kohn and Sham (KS) first assumed that each electron was noninteracting and that the system was at the ground state. Then, they decomposed the energy of n-electron system into that of *n* one-electrons. In other words, mapping the n-electron system

(interacting) on the one-electron system (noninteracting) under the given external energy. All the interacting effects are identified as:

$$E = E_{kin} + E_{ext} + E_H + E_x \quad (2.7)$$

$$E_{kin} = E_{kin}^{non} + E_{kin}^{int} \quad (2.8)$$

$$E_H + E_x \rightarrow E_H + E_x + E_c^{int} \quad (2.9)$$

E_{kin}^{non} and E_{kin}^{int} represent noninteracting and interacting (correlating) kinetic energies. The new correlation energy is counted as E_c^{int}, which is neglected in the HF method. We can regroup all the interacting terms together as a single term called the exchange-correlation energy, E_{xc}:

$$E_{xc} = E_x + E_c^{int} + E_{kin}^{int} = E_x + E_c \quad (2.10)$$

E_{kin}^{int} and E_c^{int} sum up to be the correlation energy E_c, since both are energies due to correlation. Then, the ultimate expression of the total energy within the framework of DFT consists of four energy terms:

$$E = E_{kin}^{non} + E_{ext} + E_H + E_{xc} = F[\rho(r)] + E_{ext} \quad (2.11)$$

The classical E_H (positive) becomes close to the actual quantum electron-electron interaction energy by accounting for the quantum E_{xc} (negative) in the KS system. The first three terms are relatively easy to calculate, while the last term is unknown. For DFT, we just approximate the unknown E_{xc}, and stay away from the problems of the n-electron.[151] Finally, the repulsive interaction energy between the nuclei is added as a constant within the Born–Oppenheimer approximation. The corresponding Hamiltonian is:

$$\widehat{H}_{KS} = E_{kin}^{non} + U_{ext} + U_H + U_{xc} = -\frac{1}{2}\nabla^2 + U_{eff} \quad (2.12)$$

U_{eff} is the effective potential and includes three potential terms. It manipulates the non-interacting system's ground-state electron density to be identical to the actual interacting system. This reformulation provides a much easier and effective way of calculation. Over the years, it has been proven that the scheme mimics the actual ground-state density and is able to describe the interacting system quite accurately. The non-interacting electron density and the effective potential, $U_{eff}(r)$, are consistent in the KS scheme and designed to return the true (or interacting) density and energy.

2.2.4 Ground State Energy from Kohn-Sham Equations

The energy can be minimized by finding a self-consistent result to a set of one-electron KS equations whose orbitals are subject to constraints of the orthonormality or fixed number of electrons.[151,153]

2.2.4.1 Self Consistency

Electron densities, KS orbitals and Hamiltonian are all interconnected during the DFT calculation. Self-consistency refers to the process of finding a collection of KS orbitals that results in a KS Hamiltonian whose solutions are the KS orbitals we first input. The KS orbitals compute the electron densities; the electron densities calculate the KS Hamiltonian; the KS Hamiltonian calculates the new electron densities and KS orbitals, and so on.

2.2.4.2 Variational principle

The variational process for a functional is no different from the normal minimization process for functions: finding a minimum at $dE/d\rho = 0$. The change in density $\delta\rho(r)$ is constrained so that the total number of electrons remains fixed:

$$\int \delta\rho(r)dr = 0 \quad (2.13)$$

The density minimizes variational energy at the ground state, and the energy becomes stationary with respect to small changes in density everywhere.

2.2.4.3 Constraints

The minimization of the total energy must be carried out under the constraints of orthonormality of orbitals or a fixed total number of electrons:

$$n = \int \rho(r)dr \quad (2.14)$$

$$\int \phi_i^*(r)\phi_j(r)dr = \delta_{ij} \quad (2.15)$$

where δ_{ij} is the kronecker delta (0 if i ≠ j, 1 if i = j). Without the constraints, the density could be any number, or the energy might reach below the ground-state energy, which is unphysical. The KS orbitals inbuilt the Slater determinant are initially indeterminate but will get better following the above constraints (Eq 2.14-15) to be antisymmetric and unique, thus fitting into the quantum world. We can use any of these constraints to solve the KS equations and keep the process on track.

2.2.4.4 Direct Diagonalization

The straightforward route to calculate the KS equations is by the full and direct diagonalization of the KS Hamiltonian matrix. This approach is best suited especially when an atom-centered basis set is employed for orbitals. Since the localized basis set requires only a small number of basis, direct diagonalization is efficient and relatively easy. For large systems extended with a large number of plane waves, however, the direct method becomes very inefficient because 10^4–10^5 plane waves may be needed for diagonalization of a typical DFT run to have only the lowest $\sim n/2$ eigenvalues.[151] This method is not suited for materials calculations.

2.2.4.5 Iterative Diagonalization

The DFT calculation involves two energy minimizations in series for solids and materials, as shown in Figure 2.1. Electronic and ionic minimizations.

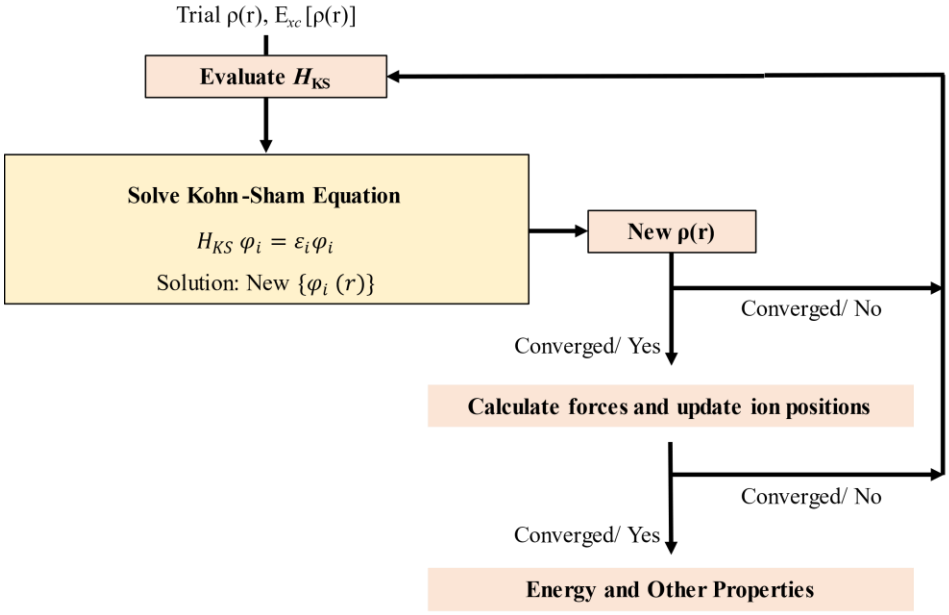

Figure 2.1. Typical DFT procedure by iterative self-consistent loop. Modified from Lee (2011).[151]

The iterative variational approach[161] is recognized as the most efficient for electronic minimization, and the classical-mechanics treatment is just sufficient for ionic minimization.

2.2.5 Total Energy and Other Properties

Several fundamental properties can be calculated once the total energy of a system is obtained. For example, bond lengths, stable structures and angles, cohesive energies from the energy minima, elastic constants, bulk modulus, surface reconstructions, defect formation energies, vibrational features from the energy curvature, and pressure-driven phase transitions. The first partial derivatives of the energy with respect to volume (V), atom position (r_I), and strain (ε_{ij}) give bulk modulus (B), pressures (P), forces (F), and stresses (σ_{ij}), respectively:

$$B = V\frac{\partial^2 E(V)}{\partial V^2},\ \ P = -\frac{\partial E}{\partial V},\ \ F_I = -\frac{\partial E}{\partial r_I},\ \ \sigma_{ij} = \frac{\partial E}{\partial \varepsilon_{ij}} \qquad (2.16)$$

Moreover, the ground-state calculation is a starting point for advanced calculations such as minimum-energy path, barrier energies, band structures, and the density of states (DOS). In addition, with further computational efforts, the second derivatives of energy provide a force constant matrix (i.e., forces acting on all other atoms when each atom is displaced in each direction), phonon spectrums, reaction rates, and thermodynamic quantities.[151]

2.2.6 Van der Waals Forces

For the vDW forces, a density-independent term is simply added to the energy density functional.[162] The added dispersion term contains a long-range interaction term and a dispersion coefficient. The formalism of these two constituents has been improved to dampen the divergence of the long range interaction term and to include more, if not all, chemical elements in the dispersion coefficient term.

2.2.7 Hubbard (U) Correction

The repulsive self-interaction of an electron and itself is not completely cancelled in DFT functionals. This results in large errors in calculations in strongly correlated systems which give rise to such self-interaction of electrons. Example of such systems are transition metal atoms which have tight-binding and localized d and f electron orbitals. To account for these interactions, a simple "+U" (Hubbard U) correction to the DFT functionals such as LDA and GGA was proposed.[163,164] This correction is only applied to the localized orbitals and not to the remainder of the valence electrons.[163] In recent years, and introduced by Dudarev et al[165], an even simpler approach has gained popularity by which the Coulomb interaction is coupled with exchange correction in a single parameter $Ueff$, given as $Ueff = U - J$. There are two approaches to finding the value of the $Ueff$ parameter. One is to take a property of the system under study and find the $Ueff$ which can reproduce the experimental value of this property. The second approach is to use other kinds of ab initio methods that can estimate this parameter.[150]

2.3 Exchange Correlation Functionals

As the name indicates, the exchange-correlation energy (E_{xc}) represents the lively activities of electrons among each other. In the DFT method, all terms are exact, with a strong basis in quantum mechanics, except for the E_{xc}, where the troublesome and the unknown terms are cast. Generally, this energy is less than roughly 10% of the total energy, but it involves determining materials properties, such as spin-polarization, bonding, and band gap formation.

The antisymmetry of orbitals requires electrons with an equivalent spin to occupy different orthogonal orbitals, forcing a spatial separation between those electrons. This reduced electron density is named the exchange hole. Two electrons with distinct spins can occupy the same orbital, but they avoid one another due to their same negative charges. This electronic correlation also generates a reduced electron density around the electron, thus generating a small attractive energy. This effect is known as a correlation hole.

At high electron densities, the exchange component predominates in the exchange-correlation (XC) hole since its origins are rooted in the Pauli Exclusion Principle, which becomes more prominent when electrons are closer to each other. However, the correlation component becomes relatively significant and comparable with the exchange part at lower electron densities. Given that most parts of the kinetic energy and the long-range Hartree energy are considered separately, the remaining E_{xc} energy can be assumed to be local or semilocal functionals of electron density. In addition, the shape of the exchange-correlation hole is conveniently assumed to be spherical in three-

dimensions. The local exchange-correlation energy per electron (ε_{XC}) is the electrostatic interaction energy of an electron at r with XC hole density at r':

$$\varepsilon_{XC}[\rho(r)] = \frac{1}{2}\int \frac{\rho_{XC}^{hole}(r,r')}{|r-r'|}dr' \qquad (2.17)$$

Then the E_{xc} energy functional is the integral over the complete space of the density multiplied by the local energy per electron ε_{XC}:

$$E_{xc}[\rho(r)] = \int \rho(r)\varepsilon_{xc}(r,\rho)dr = \frac{1}{2}\int\int \frac{\rho(r)\rho_{XC}^{hole}(r,r')}{|r-r'|}drdr' \qquad (2.18)$$

The treatment of the XC hole is similar to the Hartree interaction. The full XC hole is subject to the sum rule, which equals exactly one electron, as expected:

$$\int \rho_{XC}^{hole}(r,r')dr' = -1 \qquad (2.19)$$

As a result, a deep exchange hole will be highly localized. The XC functional fully accounts for both holes in the DFT method but only in the approximated formulations. By assuming the exchange-correlation to be potential local or semilocal during the approximation process, the calculation becomes much easier than the nonlocal HF approach. Various accuracies and computing costs were reported for a variety of functionals. The three most popular and generally used groups are functionals of the generalized gradient approximation (GGA), local density approximation (LDA), and the hybrids.

Table 2.1. Typical exchange-correlation functionals commonly used in DFT calculations.

Classification	**Examples**
Local	LDA

Semilocal	GGA
Seminonlocal	Meta-GGA
Hybrid	B3LYP

2.4 Pseudopotential Approach

This method describes the core electrons and corresponding nuclei simplified by subjecting the valence electrons to an effective potential.[166] The pseudopotential method led to the possibility of simulation of the whole periodic table. Popular approaches are the projector augmented waves (PAW),[167] norm-conserving and ultrasoft pseudopotentials as developed by Troullier and Martins[168] and Vanderbilt[169]. These approximations reach accuracy comparable to all-electron methods.[170] Therefore, in the 1970s, the pseudopotentials ab initio methods became the most powerful tool for accurately describing many-electron systems.

Another significant advance in DFT was the treatment of materials imposing links on translational symmetry, via Bloch's theorem[171], known at the time as “Large Unit Cell”. This procedure allowed the study of more realistic systems such as surfaces, defects, and impurities in amorphous systems, clusters, etc.

2.5 The Nudged Elastic Band (NEB)

NEB is a valuable DFT-based method used to find the minimum energy pathway (MEP) of a reaction and its energy barrier.[172] This method divides the path between the reactant and product (the two minima determined a priori) into several images that serve as an initial guess and are connected by an “elastic band”. This elastic band is optimized,

meaning that the perpendicular forces along the band are minimized during an NEB calculation. Hence, the saddle point and energy barrier are found, and all images are then along the MEP. The climbing-image method[173] (CI-NEB) is an improvement on NEB. It identifies the high energy image early on in the calculations, modifies the force on this image, and raises it higher on the minimum energy path. Thus, CI-NEB finds the saddle point more efficiently.

2.6 DFT Limitations

It is crucial to understand the various approximations used in DFT calculations while setting up the calculation and interpreting the results. The data collected can often be useless by ignoring the corresponding limitations and the sources of errors.

In the first-principles calculations, anything that deviates from the real n-electron picture has the potential to cause errors, for example, the Born–Oppenheimer approximation, the non-relativity approximation, mean-field approximation, the one-electron DFT approximation, single slater determinant approximation for wave functions, and XC energy approximation.[151]

Using solids in the framework of the DFT, we use additional approximations: PP (pseudopotential) approximation, supercell and PBC (periodic boundary condition) approximations, basis expansion, energy cutoff, k-points sampling, FFT (fast fourier transformation) grid, and smearing, summation replacing integration, numerical truncations, etc.

All of these simplifications are well justified and, in most cases, do not result in substantial errors if we carefully set up the system and run conditions. Because it

comprises numerous approximated energy factors, the XC functional (e.g., LDA, GGA, etc.) is usually the primary source of errors in all DFT calculations. We know that the KS scheme is precise only if we get the exact E_{xc} energy, but we also know that we may never get the exact E_{xc} energy. [151] The *XC* functional adequately describes the general picture of electronic systems but cannot collect the delicate features of the actual landscape in subatomic systems.

CHAPTER III

CAN SINGLE-WALLED CARBON NANOTUBE DIAMETER BE DEFINED BY CATALYST PARTICLE DIAMETER?*

3.1 Introduction

The need to design and control single-walled carbon nanotube (SWCNT) properties is a challenge in a growing nanomaterials-related industry. Recently, significant progress has been made experimentally to control SWCNT diameter and chirality selectively. However, there is not yet a complete understanding of the synthesis process, and there is a lack of mathematical models that explain nucleation and diameter selectivity of stable carbon allotropes. In-situ analysis of chemical vapor deposition SWCNT synthesis confirms that the nanoparticle to nanotube diameter ratio varies with the catalyst particle size (Figure 3.1). It is found that the tube diameter is larger than that of the particle below a specific size (dc ≈ 2nm) and above this value is smaller than particle diameters.

We develop a statistical mechanics-based model that correlates possible energy states of a nascent tube with the catalyst particle size to explain these observations. This model incorporates the equilibrium distance between the nucleating SWCNT layer and the metal catalyst (e.g. Fe, Co, Ni). The "most probable" diameter result explains and predicts the observed correlation between tube and solid particle size during supported

* The contents of this Chapter were reprinted with permission from Diaz, M. C.; Jiang, H.; Kauppinen, E.; Sharma, R.; Balbuena, P. B. *Can Single-Walled Carbon Nanotube Diameter Be Defined by Catalyst Particle Diameter?*. J. Phys. Chem. C 2019, 123 (50), 30305–30317.. Copyright 2019 American Chemical Society

SWCNTs' growth. This work also brings together previous observations related to the stability condition for SWCNT nucleation. Tests of the model against various published data sets show good agreement, making it a promising tool for evaluating SWCNT synthesis processes.

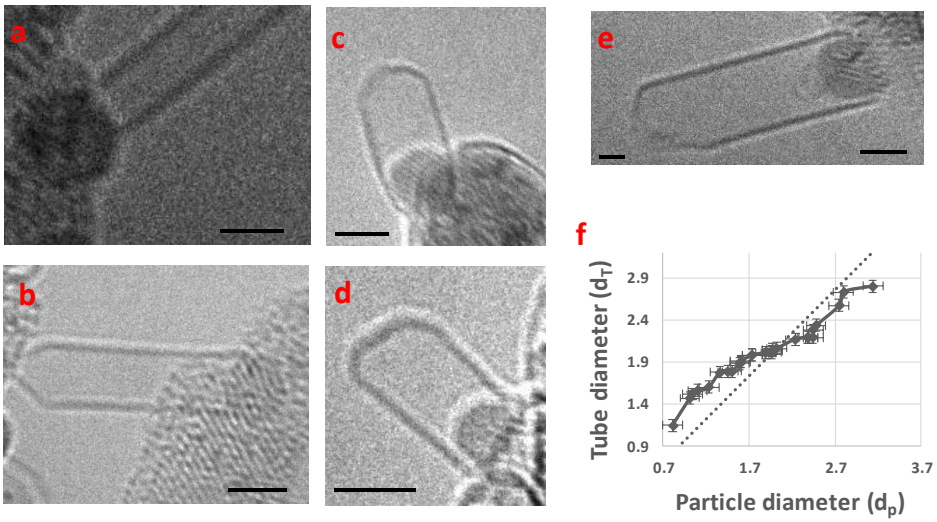

Figure 3.1. ETEM images of SWCNTs growing on Co particles. a - b) Tube diameter smaller than particle diameter, apparent perpendicular growth; c and d) Tube diameter very close to the particle diameter, apparent tangential growth; e) Tube diameter larger than particle diameter, apparent tangential growth; f) Observed correlation between tube diameter and particle diameter. Taken from Diaz et al. [39]

A critical part of the model and the basis to understand nanotube formation and its relationship to the nanocatalyst properties rely on studying the nascent tube's stability and the associated catalyst-nanoribbon interaction. A deeper analysis of the interfacial interaction between the metal surface and the graphene layer is crucial to comprehend the forces involved during the tube's nucleation. We use DFT to quantify the interaction between some common metal catalysts and carbon structures. These calculations are necessary to find a suitable model parameter value for the distance between the nascent

nanotube wall and the catalyst surface. Additionally, we use experimental data to assess the proposed model and analyze its capabilities and limitations.

3.1.1 Theoretical Background and Model Development

We model a system conformed by an infinitesimal section of the incipient SWCNT wall referred here as the tubular nanoribbon. This tubular nanoribbon has a single degree of freedom, the radial position on a curved surface (i.e. tube diameter). According to the dislocation theory[174], the presence of free radicals at the edge of the early sp^2 carbon structure allows the carbon atoms in contact with the surface to spread into new planes (edge dislocations), forming pentagons and hexagons until the complete cap is formed. The stepped spreading of the nascent cap[175] allows the system to find a local minimum in the carbon structure's curvature energy, and therefore a stable tube diameter (d_T). The probability function $f_d(d_T)$ of a tube having a certain diameter d_T can be evaluated with a statistical-mechanical model.

We define the diameter distribution f_d as a probability function of generalized coordinates (p, q) such that the statistical equilibrium condition can be expressed mathematically using Equation 3.1. This condition of statistical equilibrium dictates that the system evolves in a way that conserves the density of states and probability function f_d within a multi-dimensional space ($\prod dp_i dq_i$), called the extension of phase[176]. For our system, this condition is fulfilled by defining the probability f_d as a function of energy and including only conservative forces.

$$\sum\nolimits_i \left(\frac{df_d}{dp_i}\dot{p}_\iota + \frac{df_d}{dq_i}\dot{q}_\iota\right) = 0 \qquad (3.1)$$

We assumed that the carbon atoms on the tubular nanoribbon have a negligible velocity. The only relevant potential energy describing the intermolecular interactions is the energy stored as strain energy within the system, thanks to the material's flexible nature. The strain energy (E_{strain}) is defined in terms of Young modulus (Y), tubular nanoribbon length (L), nanoribbon wall thickness (a), and tube diameter (d_T), as shown in Equation 3.2.

$$E_{strain} = \frac{YLa^3\pi}{6d_T} \qquad (3.2)$$

The energy (dW_{bend}) needed to bend a flat 2D graphene nanoribbon with moment M through an angle $d\theta$ to form a tubular nanoribbon, as shown in Figure 3.2, corresponds to the total strain energy stored in the nanoribbon's bonds with a curvature $1/d_T$. The curvature energy (E_c) is defined as the strain energy normalized by N, the total number of C atoms, and reduced to the expression in Equation 3.3. The parameter α is usually assumed constant for a defect and impurity-free material like the nanoribbon and is defined in Equation 3.3. Kudin et al. have shown the relation of α to the flexural rigidity using the continuum shell approach[177]. Equations 3.2-3 are based on previous works[137,178–181] addressing diameter stability.

$$E_c = \frac{E_{strain}}{N} = \frac{Ya^3}{6\rho_s d_T^2} = \frac{\alpha}{d_T^2} \qquad (3.3)$$

$$f_d(d_T) \propto e^{-\frac{E_c(d_T)}{k_B T}} \qquad (3.4)$$

$$d_0 < d_T < d_p + \delta_0 \qquad (3.5)$$

The probability $f_d(d_T)$ of a tube having a certain diameter d_T is proportional to the curvature energy E_c microstate as described by Equation 3.4. The extension of phase's radial limits in Equation 3.5 accounts for all possible tube diameter (d_T) configurations, and it is related to the nanocatalyst diameter (d_p) in the upper limit ($d_{up} = d_p + \delta_0$). Here, d_0 is the minimum equilibrium distance between two graphene layers in a graphite structure at the absolute zero temperature (≈ 0.34 nm), and δ_0 is approximately the equilibrium average distance between the metal catalyst's surface and the carbon nanoribbon, as shown in Figure 3.3.

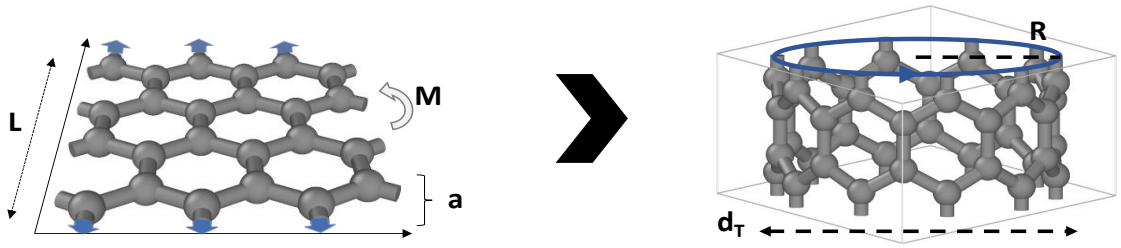

Figure 3.2. The laminar sheet of graphene was bent to form a tubular ribbon.

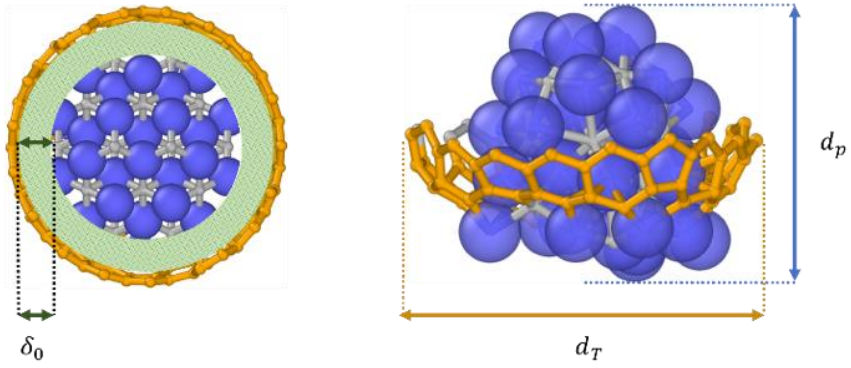

Figure 3.3. Cylindrical carbon nanoribbon interacting with a catalyst. The nanoribbon interacts with the catalytic surface and positions itself at an average equilibrium distance $\boldsymbol{\delta_0}$ at the most stable diameter $\boldsymbol{d_T}$. For a stable particle with a diameter $\boldsymbol{d_p}$, the tube

diameter $\boldsymbol{d_T}$ is constrained within a diameter range described in Eq. 3.5 as the extension of phase's radial limits.

For a nascent carbon cap supported by a metal particle, the interfacial stress bends the carbon structure to find a stable curvature. This quasi-static process follows an intrinsic energetic path under the principle of least action. Therefore, we propose a probability function in the pseudo-canonical ensemble (Equation 3.6) with a phase function distributed according to the Boltzmann probability function. In principle, this can be better understood as an *a priori* probability.

$$f_d(d_T, T) = \frac{Boltzmann\ Energy\ Distribution}{Sum\ over\ all\ possible\ states} = \frac{e^{-E_c(d_T)/k_B T}}{\int_{d_0}^{d_p+\delta_0} e^{-E_c(x)/k_B T}\, dx} \qquad (3.6)$$

At a fixed temperature, d_T is the only variable describing every possible microstate of the tubular nanoribbon. Therefore, we can use the expression for curvature energy found in Equation 3.3 to integrate the denominator in Equation 3.6. The limits in the integral shown in the denominator of Equation 3.6 match the boundaries in Equation 3.5 to account for all possible configurations. The resultant expression given in Equation 3.7 is a function only of the particle diameter (d_p), temperature (T), and the additional parameters (α, d_0, δ_0). As such, it depends strongly on the carbon and nanocatalyst intrinsic properties, as well as on the tube/nanocatalyst interactions.

$$f_d(d_T, T) = \frac{e^{-\left(\frac{\alpha}{d_T^2 k_B T}\right)}}{\left[\sqrt{\frac{\pi\alpha}{k_B T}}\,\mathrm{erf}\left(\frac{\sqrt{\alpha/k_B T}}{x}\right) + x e^{-\left(\frac{\alpha}{x^2 k_b T}\right)}\right]_{x_1 = d_0}^{x_2 = d_{up}}} \qquad (3.7)$$

$$< d_T > \; = \int_{x_1 = d_0}^{x_2 = d_p + \delta_0} x\, f_d\left(x, d_p, T\right) dx \quad (3.8)$$

The experimentally observed diameter is predicted by calculating the most probable value ($< d_T >$) according to the probability density distribution (f_d) given by Equation 3.7. The properties of the catalyst and catalyst/carbon interactions (mainly reflected in the δ_0 parameter) are determined from first principles as shown in the Methodology section. The result can be obtained by solving the expression in Equation 3.8. Moreover, the standard deviation (σ) can be found using the definition in Equation 3.9 and the probability distribution obtained previously (f_d). The standard deviation provides a measure of the most probable region where SWCNTs can grow, and it depends on temperature T and the particle diameter (d_p) through the upper integration limit d_{up}.

$$\sigma^2 = Var(d_T) = \int_{d_0}^{d_{up}} x^2 f_d(x, T)\, dx - < d_T >^2 \quad (3.9)$$

We note that some other conditions may affect the proposed representation of SWCNT curvature stability and the model parameters. For example, the growing tube's intrinsic properties, such as chirality and defects, may cause slight changes of quantum origin on the physical properties of the tube[182] (e.g. elasticity Young modulus). Additionally, the distribution of accessible diameters should be discrete based on known distances between covalently bonded carbon atoms[178–180].

3.1.2 Dimensional Analysis

The dimensional analysis is helpful to reduce some of the expressions obtained in the previous section. We can start by defining the characteristic diameter β as a temperature-dependent function, allowing us to separate the temperature effect in a simple expression (Equation 3.10) and group the particle effect using the variable $d_{up} = d_p + \delta_0$ (i.e. the upper limit in the extension of phase).

$$\beta(T) \equiv \sqrt{\frac{\alpha}{k_B T}} \quad (3.10)$$

We obtain a friendlier form of the probability distribution f_d (Equation 3.11) reducing the expression in Equation 3.7 with the new variables β, and d_{up}. In this expression, the denominator is a function of the dynamic particle curvature (d_p), and the strength of interaction (δ_0), both contained in d_{up}. For simplicity, we call the function evaluated at the denominator for both limits of the extension of phase $\phi(x)$. $\phi(x)$ is almost constant for an independent SWCNT growth event due to the slight variation of particle diameter during the dynamic process.

$$f_d(d_T, \beta) = \frac{e^{-(\beta/d_T)^2}}{\left[\sqrt{\pi}\beta \operatorname{erf}\left(\frac{\beta}{x}\right) + xe^{-(\beta/x)^2}\right]_{x_1 = d_0}^{x_2 = d_{up}}} = \frac{e^{-(\beta/d_T)^2}}{\phi(d_{up}) - \phi(d_0)} \quad (3.11)$$

The probability distribution is only valid for diameters within the extension of phase. Then, It is logical to assume that the probability of reaching a diameter with a value bigger than d_{up} or lower than d_0 is null ($d_T > d_{up}\ or\ d_T < d_0 \rightarrow f_d(d_T) = 0$). For this reason, we can constraint the Equation 3.11 multiplying the probability distribution by the Heaviside function[183] $H(d_T)$ and fulfill the previous condition.

$$f_d(d_T, \beta) = \frac{e^{-(\beta/d_T)^2}}{\phi(d_{up}) - \phi(d_0)} \left[H(d_T) - H(d_T - d_{up}) \right] \qquad (3.12)$$

Equation 3.12 could be used easily to calculate the probability of obtaining a specific diameter range for different independent particle conditions. Taking the limit when $d_0 \to 0$, we can observe that $\phi(d_0) \to \sqrt{\pi}\beta$, this value is used in the simplifications that follow instead of the evaluated value for $d_0 (= 0.34\ nm)$.

Figure 3.4 shows the simplifications for the probability distribution function (f_d) and the average diameter ($< d_T >$) using both approximations for the first case. It is remarkable to observe that the model foresees an approximate linear behavior corresponding to the upper limit in the extension of phase d_{up} for the lower stable region. This result agrees with our experimental data (Figure 3.1).

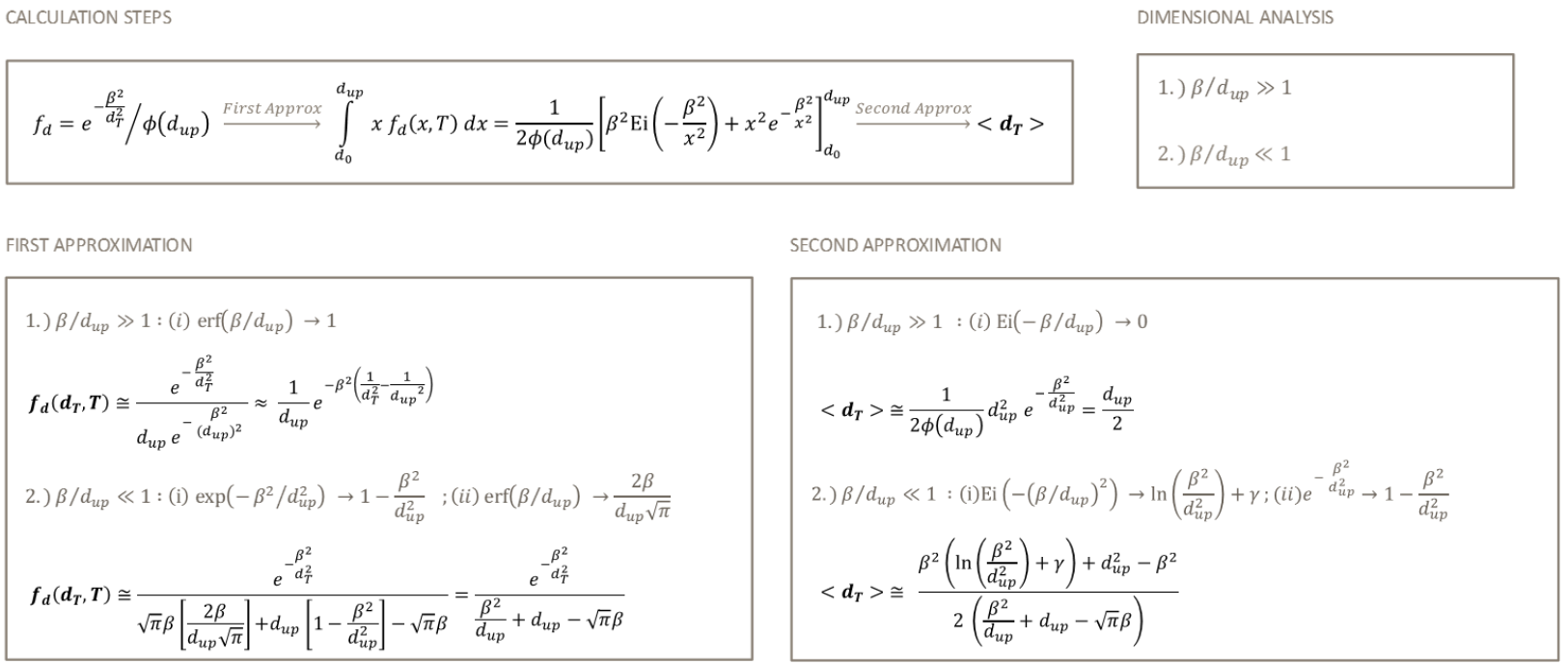

Figure 3.4. Approximations for the model using dimensional analysis. Expressions for $\mathbf{f_d}$ and $< \mathbf{d_T} >$ were obtained using both extreme scenarios.

3.2 Methodology

We perform DFT calculations for geometry relaxations and adhesion energy for graphene on metallic slabs (e.g Nickel, Cobalt, Iron) with [100] and [111] orientation (Figure 3.5-6). The exchange-correlation functional given by the Perdew-Burke-Ernzerhof (PBE) approximation[184], and the Projector Augmented Wave Method[167,185] (PAW) was employed for calculating core-electron energies. All metal-graphene systems were modeled using periodic boundary conditions (PBC) to recreate two infinite long flat surfaces at absolute zero temperature. The Monkhorst-Pack scheme[186] was used for Brillouin zone's k-point sampling with a characteristic length ($\boldsymbol{l_c}$) optimized for each metal. Table 3.1 shows the optimization results for $\boldsymbol{l_c}$, K-points, and the energy cut-off used in every system.

Table 3.1. Metal slabs parameters for the modeled system.

Metal Slab System	Length ($\boldsymbol{l_c}$)	K-points-Mesh	Energy Cutoff (eV)
Nickel	40	9 x 16 x 2	700
Cobalt	60	25 x 15 x 4	600
Cobalt Carbide (Co_2C)	50	10 x 12 x 3	700
Iron	40	16 x 5 x 2	700

The graphene–metal system has been studied extensively for transition metals like cobalt[187–190] (Co) and nickel[190–198] (Ni), and to a lesser extent for the iron[199,200] (Fe) and cobalt carbide[201] (Co_2C) surfaces. The general trend observed in these DFT studies is that the interfacial interaction energy between graphene and the metal is strongly dependent on the correlation used to calculate the dispersion energy.

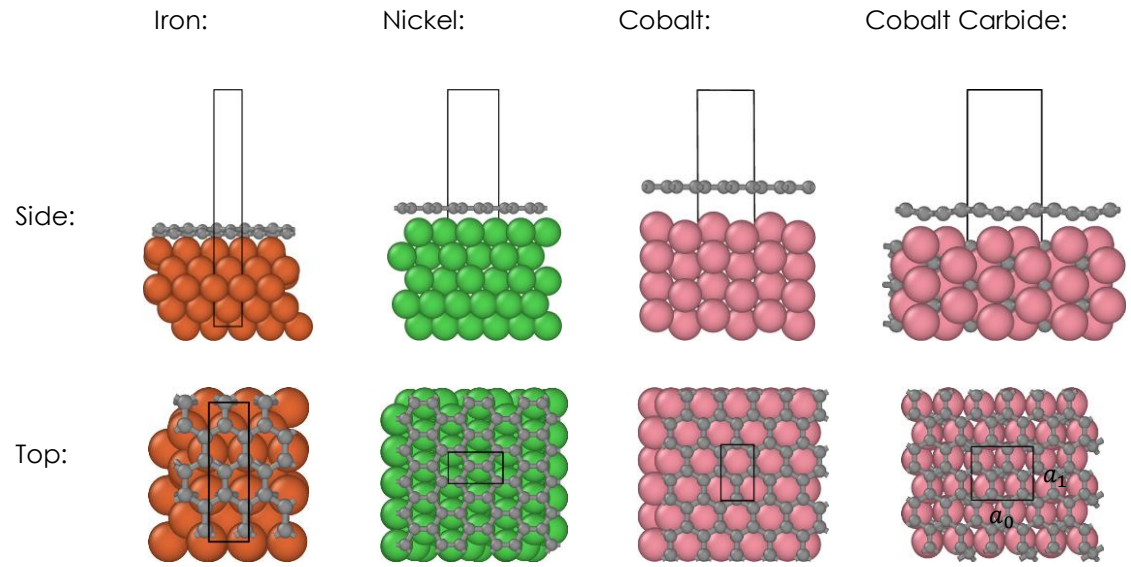

Figure 3.5. Top and side views for the metal–graphene systems using [100] metal slabs. The black rectangle at the top view corresponds to the periodic unit area, $\boldsymbol{a_0}$ and $\boldsymbol{a_1}$ are vectors conforming the shape of the simulation box.

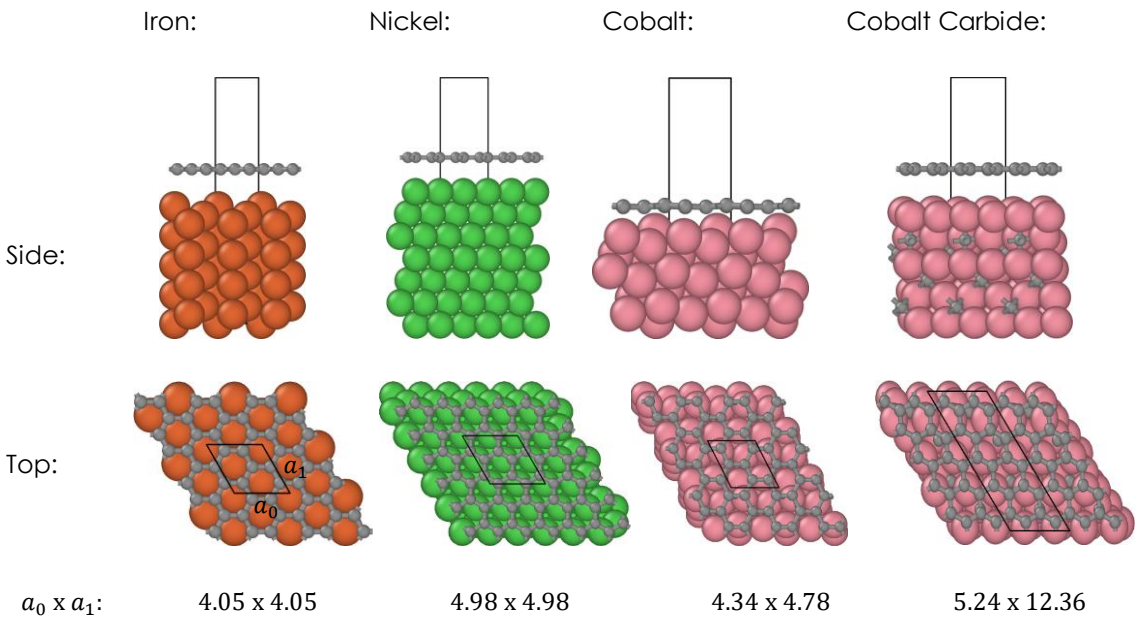

Figure 3.6. Top and side views for the metal–graphene systems using [111] metal slabs. The black parallelogram at the top view corresponds to the periodic unit area, $\boldsymbol{a_0}$ and $\boldsymbol{a_1}$ are vectors conforming the shape of the transversal area.

Other factors like the rotation of the graphene layer above the metal slab, crystal structure, and lattice mismatch may also affect this interaction. GGA-type density functionals with a long-range dispersion correction are exceptionally good for noncovalently bound systems, including many pure van der Waals (vdW) complexes[162]. Additionally, the use of exchange-hole dipole moment dispersion correction has recently improved the DFT studies' prediction compared to experimental results.[194,202]

For this reason, the dispersion correction to the Kohn-Sham energy was implemented using the DFT-D2[162] based method of Steinmann and Corminboeuf[203] (DFT-dDsC). This Van-der Waals energy correction method has the special characteristic that the dispersion coefficients and damping function are charge-density dependent[204]. Note that our model requires the equilibrium distance only.

Table 3.2. Percentage of change from the graphene lattice constant due to mismatch with the metal slab.

System	[100]	[111]
Cobalt Carbide (Co_2C)	1.32%	6.61%
Cobalt (Co)	-3.02%	15.79%
Nickel (Ni)	0.69%	1.31%
Iron (Fe)	1.75%	-4.87%

We constructed a vacuum space of 10 Å for every slab, and it was reduced to 7 Å after the graphene was coupled to the metal system. The (1x1) unit cell corresponding to the metal slab lattice vectors ($a_0 \; x \; a_1$) was used in most [100] and [111] systems. However, the Fe (100) and Co_2C (111) systems were optimized with a (3x1) and (2x1) supercell respectively to reduce the lattice mismatch with the graphene periodic unit.

The approach for the [111] structures was different, the metal slab lattice was kept fixed, and the graphene layer was rotated until reducing the mismatch with the periodic image. All the systems started with an initial separation of approximately 0.3 nm between the graphene and metal slab layers. They were relaxed until reaching the energy tolerance of $1\ x\ 10^{-6}\ eV$. Table 3.2 shows the maximum stretch or compression after the relaxation for the graphene lattice constant[205] (a_c = 0.246 nm).

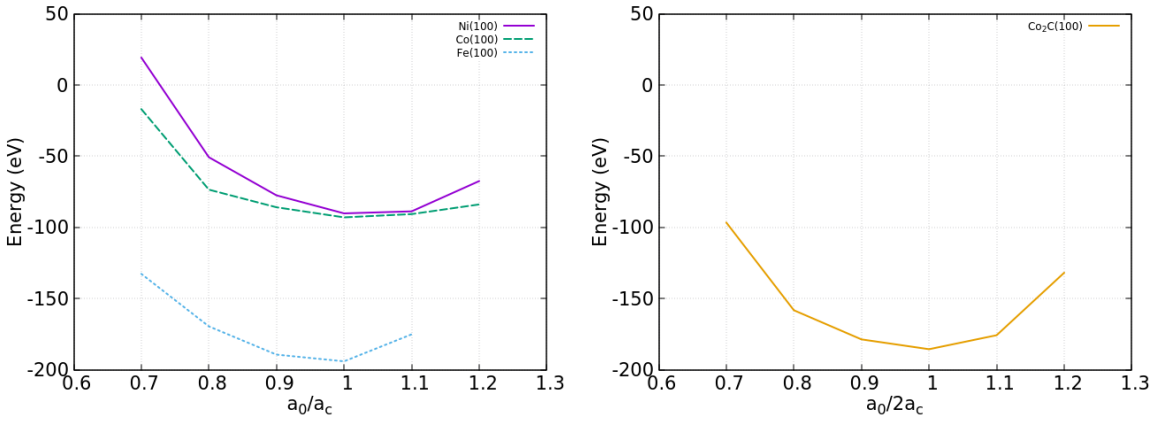

Figure 3.7. Test for optimizing the initial lattice vectors $\mathbf{a_0}, \mathbf{b_0}$ in the [100] system. The 0.7 – 1.2 range was tested for the ratio $\mathbf{a_0/a_c}$, where $\mathbf{a_c}$ corresponds to the graphene lattice vector (0.246 nm).

Figure 3.7 shows the test for the [100] structures in the graphene-metal slab system. We changed the lattice parameters and observed the variation in the system energy. We searched within the 0.7 – 1.2 range for the a_0/a_c ratio to ensure an energy minimum of the initial system and reduce the graphene's curvature (lateral stress).

3.2.1 Graphene-Metal Interaction and Evaluation of Model Parameters

The interfacial interaction energy (*Δ*Eint) values are calculated using Equation 3.13, $E_{slab\&grap}$ is the energy of the metal-graphene systems shown in Figures 3.5 and 3.6, E_{slab}, and E_{grap} are the energies of the isolated slab and graphene, respectively.

$$\Delta E_{int} = E_{slab\&grap} - E_{slab} - E_{grap} \qquad (3.13)$$

The metal-carbon interaction energy (E_{MC}) and the adhesion energy (E_{adh}) were obtained dividing the interfacial interaction energy (ΔE_{int}) by the number of carbon atoms and by the transverse area of the simulation box, respectively. E_{MC} is crucial because it defines the region where multiple stable carbon allotropes start to form[206,207] (e.g. fullerene vs. nanotube). In other words, the metal-carbon strength of interaction is an indicator of the encapsulation-growth transition. As such, it can help us to determine the minimum tube diameter value (d_T) where deactivation of the particle due to encapsulation becomes possible and may be used to characterize the stability regions as discussed further in the stability analysis.

An interesting observation based on the work-energy principle (Equations 3.2 and 3.3) is that carbon surface density (ρ_s) has a role in defining the curvature energy function, or more explicitly, the α parameter. For this reason, we evaluated the surface carbon density dependency on chirality for SWCNTs with a similar diameter. A quick analysis of the smallest repetitive section of different chiral tubes shown in Figure 3.8 indicates that the surface carbon density is almost independent of the chiral angle and has a constant average value of 38.2 atoms nm^{-2}.

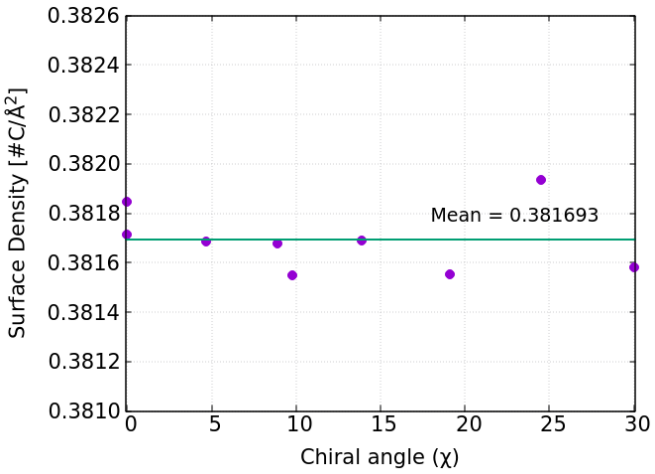

Figure 3.8. Surface carbon density ($\boldsymbol{\rho_s}$) dependence on chiral angle. Estimated values (•) using periodic units of different chiral tubes.

The equilibrium distance (δ_0) is a parameter of the model that defines the extension of phase upper boundary ($d_{up} = d_p + \delta_0$) and therefore the number of accessible microstates. However, this value changes dynamically depending on the surface local environment. Here, we use the infinite layer approximation, two periodic metal – graphene layers interacting in the interface. This method is excellent to obtain a measure of the non-bonding, van der Waals interaction, and carbon-metal distance (δ_0^{∞}). Usually, bulk carbon atoms in a graphene sheet have a coordination number of three; however, edge carbon atoms may have a reduced coordination number. For example, the δ_0^{∞} equilibrium distance in the cobalt slab (0.338 nm) decreases to 0.190 nm, 0.179 nm, and 0.161 nm by reducing to two, one, and zero, respectively, the number of neighbor carbon atoms coordinating with a central bulk graphene atom. This decrease in the equilibrium distance is related to a stronger interaction due to free electrons available to form bonds at the edge of the tube ($\delta_o^{edge} \approx [0.5 - 0.6]\, \delta_0^{\infty}$). The tubular nanoribbon

region, on which the model is based, comprises a bulk–edge combination of carbon atoms. For this reason, we assumed that δ_0 in the upper limit of the radial extension of phase (d_{up}) is approximately equal to the infinite layer value ($\delta_0 \approx \delta_0^{\infty} \approx 2\delta_0^{edge}$) for the entire diameter.

3.3 Results

Table 3.3 shows variations for the adhesion energy, metal-carbon interaction, and equilibrium distance for the different metal-graphene structures showed in Figures 3.5-6 and 8. Graphene-like ribbons allow a stronger interaction thanks to carbon dangling bonds at the edges[199], the infinite layer approximation used here focuses on the metal-carbon regions where the bulk sp^2 structure is interacting weakly with the metal.

Table 3.3. Metal structure effect in the interaction energy between catalyst and graphene. Adhesion Energy, Metal-Carbon interaction, and equilibrium distance are calculated for [100] and [111] metal surfaces.

System	Crystal Structure	E_{adh} $[eV/nm^2]$		E_{MC} $[meV/\text{atom}]$		δ_0^{∞} $[nm]$	
		[100]	**[111]**	**[100]**	**[111]**	**[100]**	**[111]**
Iron (Fe)	Bcc	-2.81	-2.66	-74.20	-63.11	0.204	0.306
Nickel (Ni)	Fcc	-0.94	-2.04	-24.77	-54.85	0.205	0.309
Cobalt (Co)	Hcp	-2.22	-6.68	-55.49	-205.86	0.338	0.219
Co Carbide (Co_2C)	Orthorhombic	-2.96	-2.63	-77.59	-68.66	0.220	0.348

The difference in the equilibrium distance δ_0 between surfaces [100] and [111] is expected due to different surface interactions and graphene alignment. Previous works in Nickel[194] and different other metals[191,195,202] have shown that even for the same facet, the chemisorption/physisorption behavior is observed due to a double minimum in the

interaction energy. It is then reasonable to assume most works report one of the two minimum equilibrium distances in the energy profile. Table 3 shows that one of the metal facet converges to either the chemisorption distances (~0.2 nm) or the physisorption distances (~ 0.3 nm) for the interaction with the graphene layer. The model doesn't distinguish between facets due to the approximately spherical shape assumption, but neither α_{opt} nor the tube profiles predicted for the iron particles show significative changes for the range 0.2 – 0.3 nm.

3.3.1 Probability Distribution Function

The probability distribution (Equation 3.7) for five particle sizes between 1 nm to 5 nm is shown in Figure 3.9 (left). We can see that the distribution collapses to zero above d_{up}, this is due to the Heaviside function $H(d_T - d_{up})$ constraint. However, it naturally converges to zero in the lower limit due to the rapid increase in curvature energy ($E_c \rightarrow \infty$), reducing the probability of reaching this microstate according to the Boltzmann energy distribution ($e^{-\infty} \rightarrow 0$). The f_d distribution evolves from a very pronounced Dirac-like form for a small catalyst to almost a uniform distribution when the particle gets bigger.

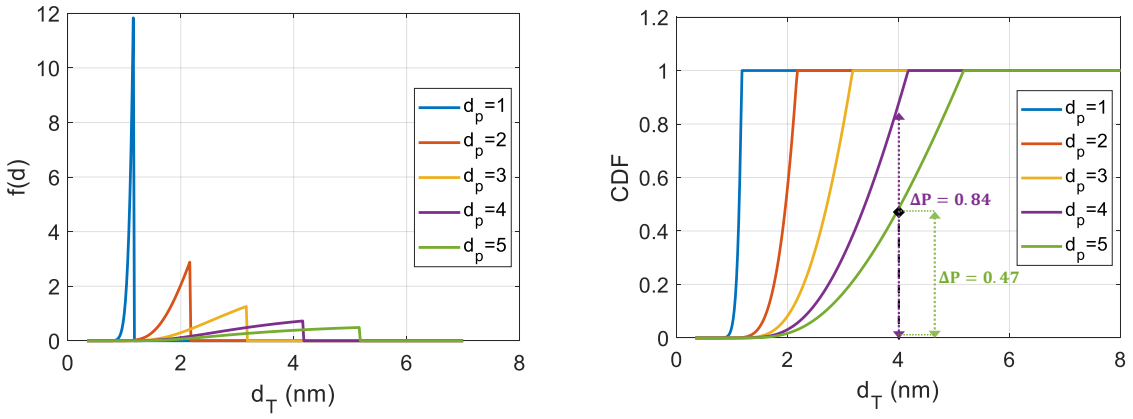

Figure 3.9. Probability distribution $\mathbf{f_d}$ using optimized parameters for a cobalt particle. [Left] Probability distribution function ($\mathbf{f_d}$) for different particle curvatures (e.g., 1 nm to 5 nm). [Right] Cumulative distribution function. The probability of obtaining a 4 nm diameter tube using different particle sizes (4 nm and 5 nm) is calculated for this scenario.

A quick example for the probability calculation is proposed with the parameters fitted from our experimental data set (e.g. α_{opt}). Figure 3.9 (right) shows the cumulative distribution function (CDF) in Equation 3.14 for our model.

$$CDF(d_T) = \int_{-\infty}^{d_T} f_d(x,T)dx \qquad (3.14)$$

Using the CDF properties, we can calculate the probability of obtaining a tube within a certain diameter range. The probability of obtaining a tube diameter of at least 4 nm is 84% with a particle diameter of 4 nm and only 47% with a particle diameter of 5 nm.

3.3.2 Test of the Model for the Small Particle Range (d_p < 5nm)

We first attempt to replicate the experimental data trend relating the particle diameter d_P to the tube diameter d_T (Figure 3.1). The interfacial distance δ_0 found

previously for cobalt is used to define the upper integration limit d_{up}. The parameter α as discussed previously, can be estimated using Equation 3.3 from the work-energy theory for elastic materials presented in the first part of the supplemental information. This relation makes α exclusively dependent of tube properties like Young modulus (Y), the atomic surface density (ρ_s) and the wall thickness (a). Values of Young moduli obtained from prior atomistic studies are largely scattered, varying from (0.95 TPa to 5.5 TPa) for Y and [0.06 nm to 0.69 nm] for wall thickness (a) [208–212]. The uncertainty on the definition and estimated values for these properties can impact α greatly. For this reason, a convenient procedure for including the variations in the carbon nanoribbon properties is to numerically optimize the α value from the experimental data and compare it with previous estimations.

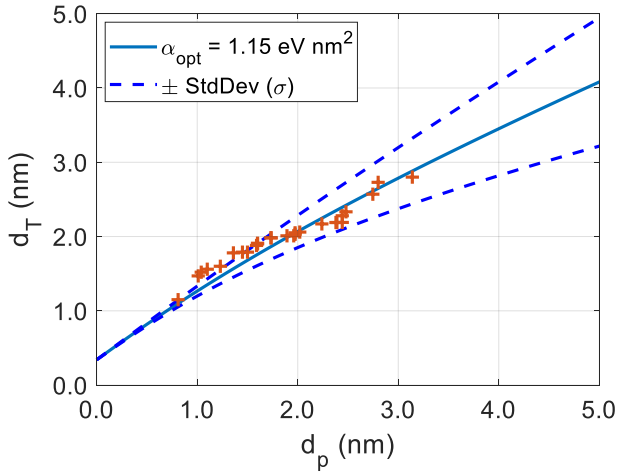

Figure 3.10. Adjusting the parameter $\boldsymbol{\alpha}$ to our SWCNT experimental data. (+) High-resolution TEM experimental data from Diaz et al[39]. (−) Most probable or average diameter and (--) standard deviation limits ($\pm\boldsymbol{\sigma}$) obtained after $\boldsymbol{\alpha_{opt}}$ has been found.

Figure 3.10 shows the results of fitting the model to our experimental data. The optimized α_{opt} value for our SWCNT data using a cobalt catalyst is 1.15 eV nm^2 atom^{-1}.

The inflection point (i.e. the point where the ratio d_T/d_P is approximately one) in the diameter's behavior can be observed and explained within the model. For very small particles (< 2 nm), the most probable diameter (solid line) is close to the upper limit ($d_T \rightarrow d_p + \delta_0$) in the extension of phase. This is due to the small range of possible states that results from a very sharp narrow probability distribution (Figure 3.9). On the other hand, the probability distribution for large particles is broader, and the average is expected to be in an intermediate value between both limits of the range [d_0, d_{up}]. Hence, the most probable tube diameter in small particles is larger than d_p, and the growth should be tangential to the particle ($d_T > d_p$), whereas the growth for large particles is expected to be perpendicular ($d_T < d_P$).

It is important to further analyze the meaning of the α parameter. For this reason, it is also necessary to consider previous evaluations of this parameter. For example, Gülseren et al reported a value of α = 0.0214 eV nm^2 atom^{-1} obtained from ab-initio calculations[181] ($E_c = \alpha/R^2 = E_{CNT} - E_{grap}$). This value is equivalent to α = 0.0856 eV nm^2 atom^{-1} in our curvature energy representation ($E_c = \alpha/d_T^2$). However, α_{opt} (1.15 eV nm^{2}atom^{-1}) is one order of magnitude higher than the one predicted by Gülseren et al. This difference in α values can be related to the uncertainty in the evaluation of the SWCNT wall thickness where approximations also vary in orders of magnitude[208,209,212]. In an atomic thin shell model, the wall thickness is considered to be the graphite inter-layer spacing (0.34 nm), Cai et al. demonstrated that this value also corresponds closely to the thickness of the SWCNT electron cloud[211]. To test the accuracy of our α, we estimated the Young modulus (Y) using the optimized α_{opt} value. Thus, using the 2D

approximation (bending tubular carbon nanoribbon) in Equation 3.3, the previously calculated surface carbon density ρ_s , α_{opt} , and the value of 0.34 nm for the tubular nanoribbon thickness, we estimate a value of 1.07 TPa for the Young's modulus of SWCNTs, that is within the range of many model approximations[210,213,214] (0.97 TPa to 5.5 TPa), and very close to the few experimental values reported for SWCNTs[215–217] (1.20 TPa to 1.25 TPa).

Test of the model for large particle range (d_p > 5 nm)

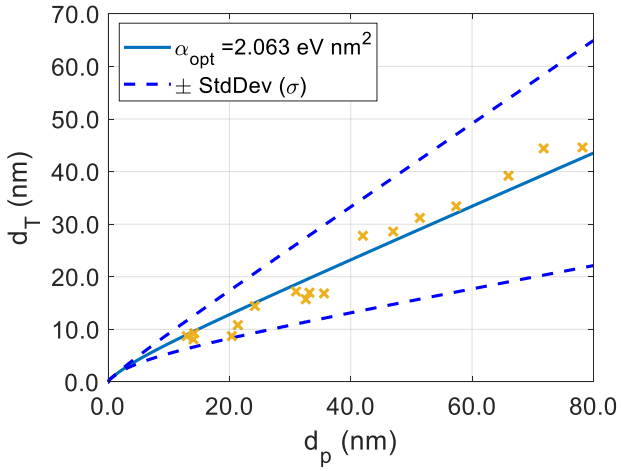

Figure 3.11. Adjusting the parameter **α** to inner diameters in the MWCNTs experimental data[39]. (x) Data collected for iron particles from Tibbets[137]. (−) The most probable or average diameter and (--) standard deviation limits (**±σ**) obtained after $\boldsymbol{\alpha_{opt}}$ has been found.

Next, we used the experimental set by Tibbetts[137] that reports inner diameters of multi-walled carbon nanotubes (MWCNTs) for very large particles. Although the growth mechanism of MWCNTs is not yet clear, we assume that the inner tube structure nucleation occurs under similar conditions to the ones mentioned previously for SWCNTs. Figure 3.11 shows that the *inner* diameters in MWCNTs can also be adjusted

to our model, yielding an α_{opt} value of 2.063 eV nm^2 atom^{-1} using δ_0 for iron (Table 3). To explain the difference between the α_{opt} for SWCNTs in small particles and MWCNTs in larger particles, it should be noted that the inner diameter in an MWCNT may be affected by the presence of compressive/attractive forces generated by the external walls causing an increase in the ability to store potential elastic energy within the curvature of the tube. An increase in the bending momentum stored by the carbon atoms at the edge of the tube is expected to affect the flexural rigidity (bending stiffness) and the α value in the inner tube structure of MWCNTs. The difference could also be attributed to the van der Waals forces between the inner nuclei and the concentric layers of an MWCNT. These additional forces can modify the mechanical properties of the inner tube. Using the same approximation utilized for the SWCNT thickness (0.34 nm) and the α_{opt} obtained for MWCNTs, a Young's modulus of 1.93 TPa is estimated, that is in reasonable agreement with reported Young moduli for MWCNTs[218].

We remark that the range of particle diameters in the two sets of data shown in Figures 3.10 and 3.11 is extensive. To compare and test the applicability of the α values, we additionally evaluated both data sets with the α_{opt} obtained for the smallest tubes and the value reported from Gülseren[181] (Appendix A, Figure A3). The model predicts a good estimate of the inner diameter value in large particles.

It is found that the predicted tube diameters are much more sensitive to the α value in the small tube range. The α dependence becomes weaker for larger tubes, where the probability function is distributed over many possible configurations. We note that although α_{opt} was obtained for the previously described sets of data, it could be applied

to other metal catalysts because its calculation only involves tube properties. For this reason, the prediction of an SWCNT diameter distribution on a bed of iron nanoparticles is proposed as a final test for α_{opt}.

3.3.3 Prediction of SWCNT Diameter Distribution

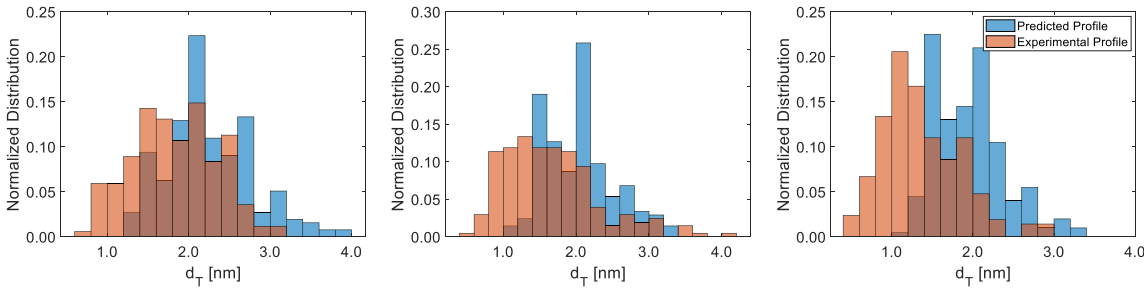

Figure 3.12. SWCNT's diameter distribution prediction using Iron catalyst particle profiles measured by Zou et al[132]. Figure 3.12 a-c corresponds to the experimental tube diameter distribution profile (orange) vs the model's prediction (blue). Predictions were based on experimental catalyst particle diameters for particles (a) without etching and (b and c) after 10 s to 15 s of etching, respectively. The darkest colored regions show the overlap between the experimental and the theoretical descriptions.

Further validation and a possible application of this model is shown in Figure 3.12. The model was used to predict the SWCNT diameter distributions corresponding to catalyst diameter profiles measured on a support of Si-SiO_2 wafer by Zou et al[132]. The predictions were obtained using the diameter profiles for the catalyst particles at different etching times to define the upper limit (d_{up}). This is because the range of the particle diameter distribution is reduced after exposure to a longer etching time. The experimental data was normalized using Equation 3.15 and the parameters used for the prediction (Equations 3.7 and 3.8) were the equilibrium distance δ_0 for Iron (Table 3) and the parameter α_{opt} (1.15 eV nm^2/atom).

$$Normalization = \frac{Frequency}{\#\, Measurements} \quad (3.15)$$

We observe that all the predicted profiles in 13a-c are in good agreement with the reported experimental sets. The slight right shift at the distributions of the three examples is attributed to assumptions on the estimation of δ_0 and α_{opt}. The equilibrium distance approximation for the nanoribbon ($\delta_0 \approx \delta^{\infty} \approx 2\delta^{edge}$) as discussed before, will affect the probability distribution for small particles. An overestimation of δ_0 may cause this type of shift due to an increase in the upper limit (d_{up}) and the number of possible accessible microstates. However, for the δ_0 range found in this and previous studies (0.2 to 0.35 nm) the shift due exclusively to δ_0 will not account for the total difference. A lack of information in the inactive particles and non-growth events may contribute to overestimating the number of tubes from the particle distribution.

3.4 Stability Analysis

This section analyzes the stability conditions and shows the estimated tube diameter prediction within the growth stability limits. This discussion relates only to systems where the reaction conditions favor a slow carbon supply rate on the catalyst surface (e.g., low precursor gas pressure). Reducing the carbon supply flow would likely allow the carbon structures to evolve to low energetic configurations[219].

An important question relates to the probability of a nascent cap to evolve into a stable SWCNT or encapsulate the catalytic particle (stable fullerene). Early studies in carbon allotropes have established the relation between curvature energy and tube diameter[137,178–181,219] as described in the theoretical background (i.e. Equations 3.2, 3.3).

Burgos et al., for example, showed a direct relation between adhesion energy, curvature, and nucleation[206], as expressed in Equation 3.16. Furthermore, an approximated support-particle interaction analysis showed that the support nature strongly influences the catalyst structure, shape (i.e., curvature), and tube's diameter[220,221].

$$\underbrace{E_{cT}}_{Tube\ Curvature\ Energy} \leq \underbrace{\underbrace{E_{cF}}_{Fullerene\ Curvature\ Energy} - \underbrace{E_{MC}}_{Metal-Graphene\ interaction\ energy}}_{Metal\ supported\ Fullerene\ Energy} \tag{3.16}$$

Comparing the curvature energy per atom of the tube (E_{cT}) with the one for a fullerene with a similar diameter (E_{cF}), it shows that the tube is always more stable. However, the attractive metal-graphene interaction (E_{MC}) may reduce the energy necessary to bend the carbon bonds and therefore the curvature energy per atom of the fullerene capsule ($E_{sF} = E_{cF} - E_{MC}$).

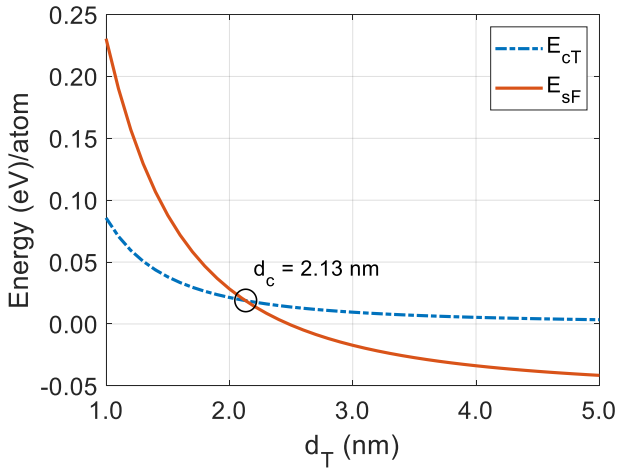

Figure 3.13. Stability analysis for the nucleation of carbon allotropes on metal catalysts. Empirically fitted functions for the curvature energy in SWCNTs (E_{cT}) and fullerenes (E_{sF}) and the critical diameter of transition (d_c) for a cobalt catalyst.

Hafner et al. introduced the stability criteria graphically using empirically fitted functions to represent the curvature energy of tubes and fullerenes[219]. Following Hafner's work, Figure 3.13 shows that the energy difference between both states is in the order of meV.

We used the cobalt-carbon calculations (Table 3) to estimate the fullerene capsule energy (E_{sF}) in Figure 3.13. We observe that even if a tube is less stable for diameters approximately above d_c in a cobalt particle, the energy difference is minimal, and in many cases, nanotubes are observed to grow with a nucleation probability proportional to $e^{(-E_{MC})/k_bT}$. An interesting observation is that d_c corresponds to the point where the ratio between d_T/d_P is approximately one for our experimental data, and the growth behavior changes from tangential to perpendicular. Therefore, we could use this value as a point of reference and merge the stability analysis with our model.

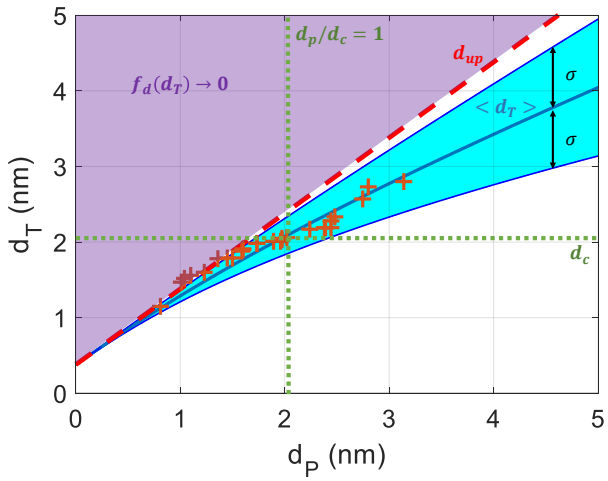

Figure 3.14. Diameter stable regions during the growth process of SWCNTs and high probability zones within one standard deviation from the most probable diameter ($< \mathbf{d_T} > \pm \boldsymbol{\sigma}$). (+) High-resolution TEM experimental Data for Co catalysts. (--) Upper limit for the radial extension of phase ($\mathbf{d_{up}}$). (···) Transition critical diameter ($\mathbf{d_c}$) between stable fullerene and tube allotropes. (−) Most probable or average diameter and standard

deviation limits ($\pm\boldsymbol{\sigma}$). In the purple region, the probability of finding a diameter d_T is $\approx$ 0.

Curvature stability plays a role in delineating the stable tube growth regions. These are tube diameter stable zones for specific particle diameter regions. The small particle zone ($d_p/d_c \ll 1$) has the d_c line as an upper limit on stability. In this zone, the tube is always trying to reduce its curvature energy, making the transversal area as big as possible until $< d_T >$ or a value energetically accessible is reached. We can also observe that most of the experimental data is close to d_{up} for this zone, this is due to the existence of a very low standard deviation, leading to a small region with a high probability of nucleating the tube. Above d_{up} the probability distribution f_d rapidly collapses to zero ($f_d \to 0$) so wider tubes beyond this limit do not grow. In our model, the accuracy of the d_{up} limit depends on δ_0 estimation that has an associated error as discussed in the model parameters section. Figure 3.14 shows that the tube diameter is slightly smaller than the particle diameter in the transition zone (for $d_p > d_c$ and d_p smaller than 2.5 nm).

For SWCNTs growing on large particles ($d_p/d_c \gg 1$), the upper limit of stability is the line corresponding to d_{up}. In this region, the tube tries to minimize its internal strain energy by reducing the transversal area until reaching the most probable diameter region with a value close to d_c. That is why we see an inversion in the data trend between the two zones (i.e. the tube diameter is no longer bigger than the particle). This zone is also characterized by a co-existence between fullerenes and tube allotropes. For carbon allotropes with weak metal-carbon interactions ($< 1\ eV$) the curvature energy favor

nucleation, but a strong metal-carbon binding energy (1 eV to 2 eV) favors encapsulation in every event for particles with a diameter above the transition diameter (d_c).

The nature of the metal catalyst affects the value for d_c. For example, iron, with strong metal-carbon interaction, should have a smaller d_c affecting the probability of encapsulation and the transition between tangential and perpendicular growth.

3.5 Conclusions

Using a combination of experimental data, quantum mechanical calculations, and statistical mechanics, we developed a model to describe the relationship between catalyst size and SWCNT diameter. The proposed model offers a simple description of the correlation between tube diameter and catalyst particle diameter for a growing SWCNT on an approximately spherical solid active nanocatalyst. Our model could include multiple curvatures in large particles/substrates ($k = 1/d_p$) as individual events represented in the probability distribution function f_d.

The DFT calculations of interlayer adhesion energies provide essential information about the strength of interaction between common metal catalyst particles and graphene. We show that the value obtained (α_{opt}) is only dependent on intrinsic properties of a graphene-like structure such as surface carbon density, wall thickness, and Young modulus and could be used in many systems independently of the catalyst selection. The Young moduli obtained from the optimized parameter for SWCNTs and MWCNTs are in good agreement with experimental values.

The rim-metal interaction analysis shows the stability of specific edge configurations and the effect on chirality selectivity. Nevertheless, the study suggests that the catalyst particle size's influence on the nucleation probability must be added separately. The results showed that the careful estimation of model parameters like α_{opt} and the tube wall-catalyst surface distance δ_0 is a requirement for a good accuracy of the model. We have noticed, for example, the ability of δ_0 and α for shifting the predicted tube diameter profile based on experimental catalyst size distributions. Thus, changes in δ_0 increase or reduce the number of possible states in the proposed continuous function approximation for the tube diameter probability distribution (f_d).

Finally, our work's central focus was on whether catalyst particle diameters define single-walled carbon nanotube diameters. We identified a critical diameter that separates regions of stable nanotube and stable fullerene. Such critical diameter depends on the intrinsic catalyst properties and their interactions with carbon. For d_T larger than such critical diameter, the growth behavior changes, and the tube diameter tend to become smaller than the particle diameter, leading to a perpendicular growth. This transition to the perpendicular mode of growth coincides with a much broader probability distribution function, allowing an extensive range of possible tube diameters for the defined particle size. Interestingly, the model has also proved helpful in predicting the inner diameters of MWCNTs and reproducing d_T distributions using the catalyst diameter distribution profile for supported CVD particles.

We recognize that particle composition and surface stability play an important role in the SWCNT nucleation vs. catalyst encapsulation dynamics. Magnin et al. [222] recently

highlighted a correlation between the carbon concentration in the particle and graphene/catalyst wetting properties, thus leading to tangential vs. perpendicular growth. Our subsequent work suggests that different surface compositions may also be responsible for the change of growth mode.

CHAPTER IV

ON THE ROLE OF SURFACE OXYGEN DURING NASCENT CARBON CAP SPREADING AND SINGLE-WALLED NANOTUBE NUCLEATION ON IRON CATALYSTS[†]

4.1 Introduction

Single-walled carbon nanotubes (SWCNTs) are commonly grown in oxygen-rich environments. The precursor gas for the SWCNT synthesis reaction typically provides oxygen atoms either as a pure gas or as an oxygen-containing compound. Similarly, metal oxide substrates are used to support the catalysts or as reactor wall materials and may transfer oxygen atoms while in contact with the catalytic particles. It has been proposed and experimentally observed that the metal catalyst's interaction with specific promoters (e.g., oxygen, sulfur, hydrogen) triggers significant changes in the SWCNT properties during spreading, nucleation, and growth.

Dai et al. introduced the *yarmulke* mechanism[51] during one of the first reported metal-catalyzed disproportionation of CO on pre-formed molybdenum (Mo) particles, pointing to a strong correlation between tube and particle diameters. Recently, CVD experiments for cobalt (Co) have also validated that SWCNT diameter is inherently related to particle size.[39,223] However, the close analysis of transmission electron microscopy (TEM) images of tubes grown by a CO precursor feed on Fe particles shows that the diameter profile of SWCNT does not seem to increase proportionally with the

[†]The contents of this Chapter were reprinted with permission from Diaz, M. C.; Balbuena, P. B. *On the Role of Surface Oxygen during Nascent Single-Walled Carbon Nanotube Cap Spreading and Tube Nucleation on Iron Catalysts*. Carbon 2021, 184, 470–478. Copyright 2021 Elsevier Ltd.

diameter of catalyst particles,[53,54,224] and additionally, the ratio between diameters (d_p/d_T) can be larger than three for very small particles (2-5 nm).[224] This observation is unusual and repetitive not only for setups that use iron, but for SWCNT growth on different oxidized metal catalysts[225] as well. The uncorrelated particle-tube diameter and the large size difference (for $d_p < 3\ nm$) defies common understanding and theoretical mechanisms for nanotube nucleation and growth[39].

Here we suggest that surface oxygen may influence the interaction between the metal and the early cap seed resulting in an unexplained correlation between nanotube diameter and catalyst particle. Our hypothesis is based on evidence from experimental works using Fe catalysts that indirectly point toward oxide-driven growth of carbon nanotubes[226,227] and the active role of oxygen in SWCNT selectivity over CNTs with multiple walls[226] (MWCNTS). Mazzoni et al.[228] showed that large oxidized carbon rims might be unstable due to a rapid sublimation into CO_2. We studied a critical aspect of the nanotube formation in this section: the pre-nucleation conditions and the initial cap structure's evolution on an oxygen-rich iron surface. We used DFT calculations to obtain an insight into the interacting forces between the metallic surface and the nascent cap and comparatively show the effect of oxygen on the interfacial energy. Additionally, we analyze the oxide-driven mechanism proposed for the growth of SWCNT by the disproportionation of CO on iron.

4.2 Methodology

Interfacial adhesion energies were obtained using spin-polarized DFT calculations on an iron slab with (110) orientation. Fe (110) was chosen because it is the most stable

facet for bcc iron[229]. We used a (5x5) Fe (110) supercell with five layers and a vacuum space of 10 Å for our systems. The initial (1x1) Fe (110) slab had a lattice parameter of 2.48 Å. The gamma-centered Monkhorst-Pack scheme[186] was used for the Brillouin zone's k-point sampling with a grid 4x4x1. The exchange-correlation functional given by the Perdew-Burke-Ernzerhof approximation[184] and the Projector Augmented Wave Method[167,185] (PAW) was employed for calculating core-electron energies with a cutoff energy of 700 eV. We performed all DFT energy calculations with an electronic convergence tolerance of $1x10^{-6}$ eV and ionic convergence on the total energy of $1x10^{-3}$ eV using the Vienna Ab Initio Simulation Package (VASP)[230].

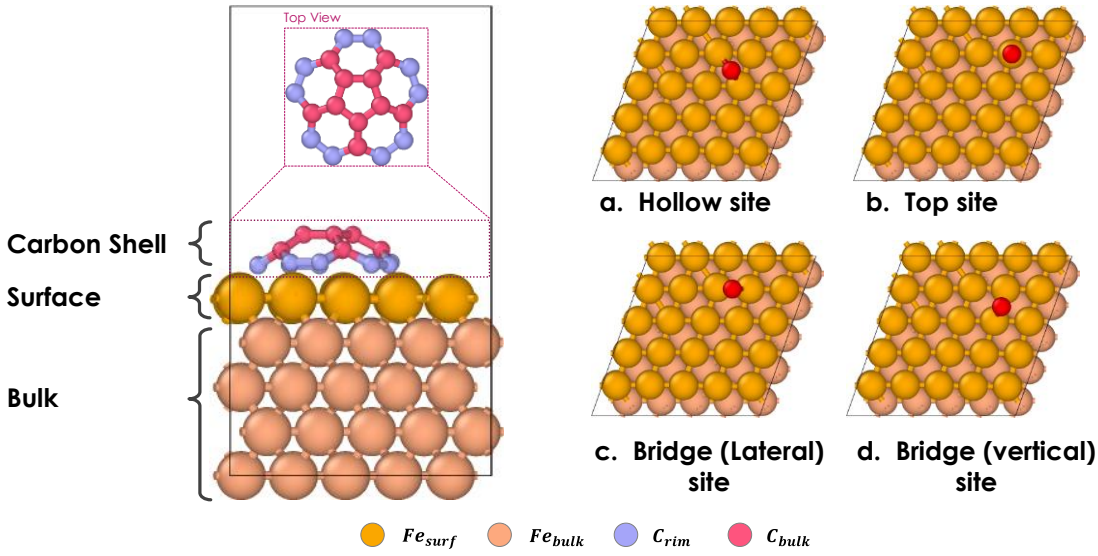

Figure 4.1. Fe (110) Slab with five layers, the graphitic carbon shell corresponds to the pre-nucleated cap of a (5,5) AC tube. [a-d] Initial possible positions for the oxygen atom location before relaxation. Color code for atoms: surface O: red, surface Fe: orange; subsurface Fe: pink. The central pentagon and C atoms connecting the pentagon to the cap edge: maroon; hexagon edge atoms: light blue.

Electronic and magnetic properties of iron oxides by DFT can be troublesome using the local density approximation (LDA) or the generalized gradient approximation

(GGA)[231] because these approximations do not describe correctly the on-site Coulomb interaction of localized electrons. For this reason, it was necessary to use the Hubbard *U* correction (DFT+U) for the calculations with oxidized surfaces. We used the bulk magnetite (Fe_3O_4) structure to find an adequate *U* correction that reduced the lattice parameter errors, the analysis can be found in Appendix B (Figure B1). The value of U = 3.8 eV was observed to reduce the error with or without van der Waals (vdW) dispersion corrections, and it is consistent with previous studies on iron oxides[231].

The iron slab was built by keeping the bottom two layers fixed at their bulk positions and relaxing the remaining layers with DFT optimization. The chosen graphitic carbon shell corresponds to an early stage of a (5,5) armchair (AC) nanotube cap structure (Figure 4.1). The pre-nucleated shell has only one pentagon formed of the five usually needed before complete nucleation occurs. We also modeled partial surface oxidation by O adsorption on the Fe (110) surface. Our calculations, in agreement with previous works,[232] showed that oxygen atoms move freely to the most stable hollow sites after relaxation from an initial top or bridge position. We oxidized the iron slab in an iterative cycle, increasing the oxygen concentration on the slab surface until it reached 0.24 monolayer (ML) coverage. For each addition cycle, we calculated the relaxed energy of all possible non-symmetrical hollow sites for a new O atom insertion and took the one with the highest average interfacial energy ($|E_{sys} - E_{slab}|/N_O$). Figure 4.2 shows the oxygen positions after each addition cycle.

The interfacial binding energy ($E_{interfacial}$) between the carbon shell structure pre- and post-nucleation is calculated using Equation 4.1. Where E_{sys} is the energy of the

combined system, E_{CS} is the energy of the carbon structure (e.g., SWCNT, cap, carbon shell seed) and E_{Fe-O} is the energy of the iron slab (either reduced or oxidized). Here we use the word "reduced" to refer to the pristine Fe surface where the Fe atoms have a neutral oxidizing state (atomic charge = 0 e)

$$E_{interfacial} = E_{sys} - (E_{CS} + E_{Fe-O}) \qquad (4.1)$$

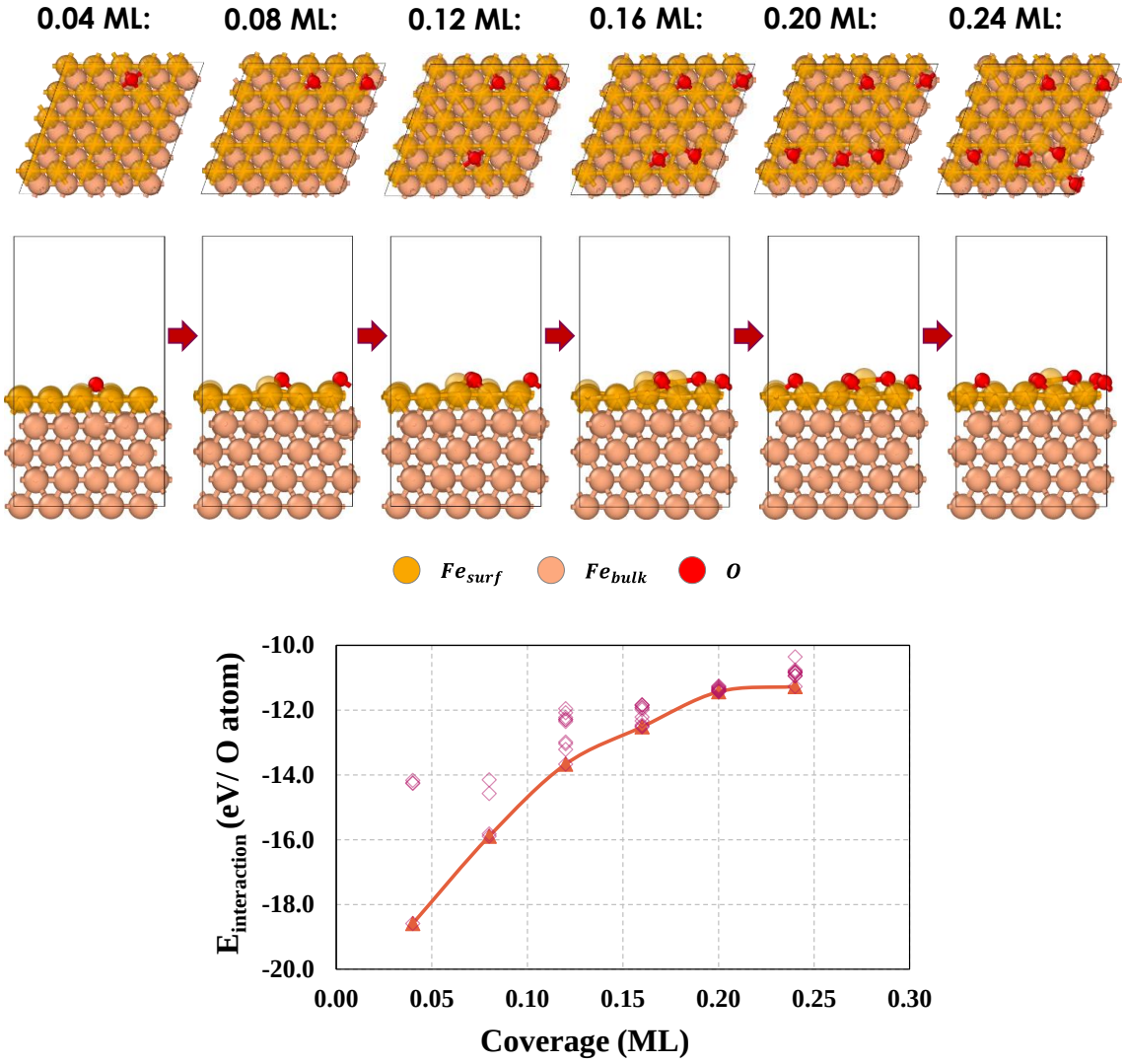

Figure 4.2. [Top] Oxygen atom positions after each addition cycle. We selected the structure with the strongest O-surface interaction energy after each new addition. [Bottom] Interfacial energy per oxygen atom after increasing oxygen concentration;(◊)

Interaction O-surfaceenergy for all possible oxygen configurations; (▲) Strongest O-surface interaction energy . Color code for O and Fe atoms as in Figure 4.1.

4.3 Results

4.3.1 *Pre-nucleated carbon shell on the oxidized iron surface*

In this section we follow the evolution of the interfacial energy between a carbon shell (as shown in Figure 4.1) and the surface, on two partially oxidized iron surfaces. The first surface (S1, first row in Figure 4.3) corresponds to an iron slab with increasing oxygen surface concentration (from 0 to 0.24 ML), that was obtained following the least energy path described in the previous section. The second surface (S2) results from adding a 1:1 carbon to oxygen ratio (C:O) to the surface, C atoms were adsorbed in the surface and allowed to find a stable minimum energy position. We observed that the presence of absorbed carbon (at the same O concentration) did not significantly change the C_{rim}/metal interfacial interaction with the oxidized metal slab. Carbon usually diffuses into the particle subsurface until reaching a maximum saturation concentration. In this work, we have not searched for such saturation point. In addition, if the carbon shell is already formed, the highly active carbon shell's rim will promote the incorporation of the carbon to the structure's edge if the C atom is close enough. The interfacial energy per carbon atom at the rim ($E_{interfacial}/C_{rim}$) between S1 and S2 is within a close difference ($\approx \pm 0.25\ eV$). However, the change of the energy with oxygen concentration has some distinct behavior, as explained next.

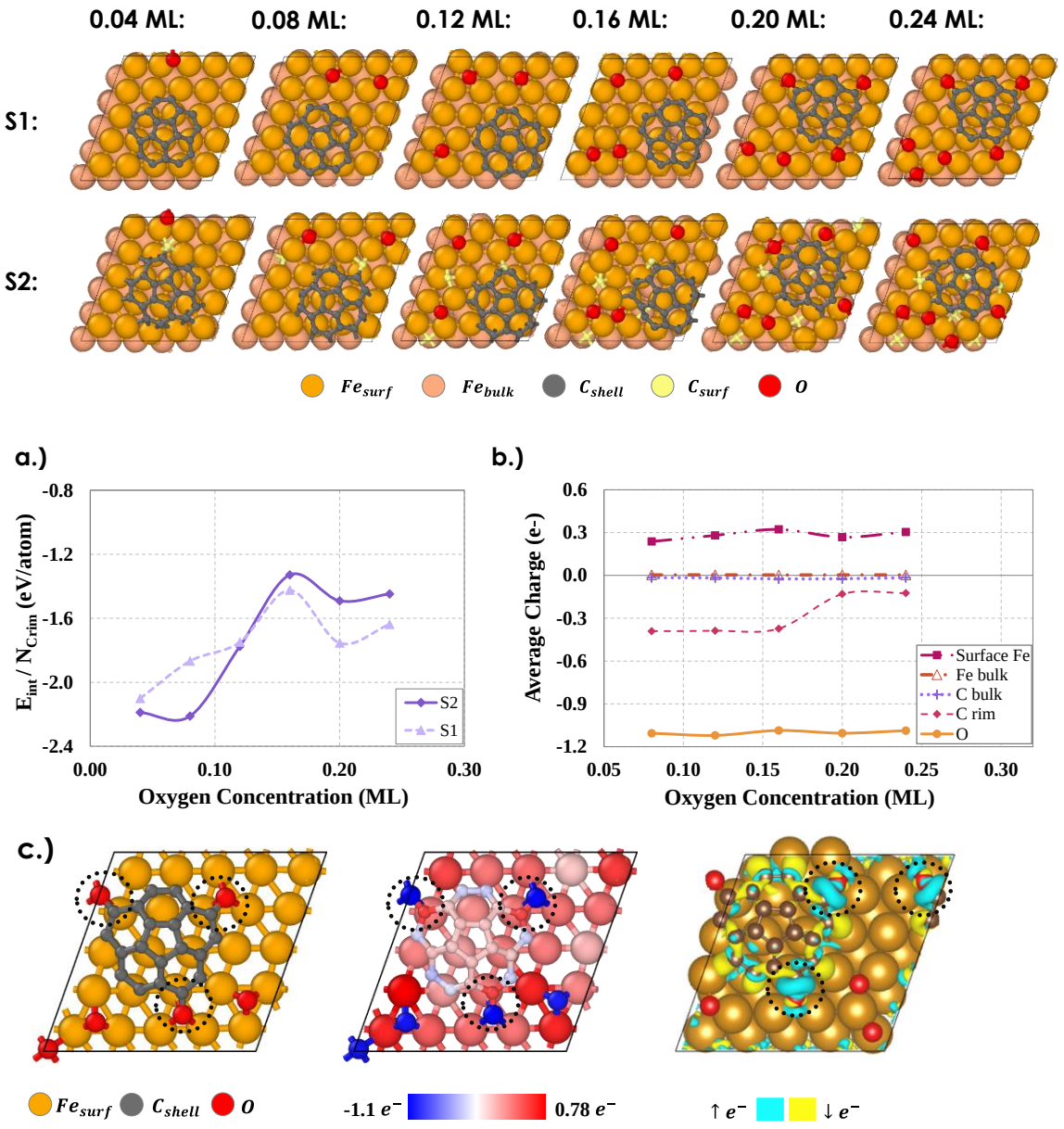

Figure 4.3. Top: Pre-nucleated shell interacting with two oxygen-rich Fe (110) surfaces. S1 and S2 differ in the adsorbed C:O ratio, with 0:1 and 1:1, respectively. Bottom: [a] Interfacial energy per carbon in the rim for both surfaces. [b] Average charge of the metal surface and carbon atoms in the shell for S1. [c] Direct C_{rim}-O interaction at 0.24 ML, atomic position, charge, and CDD are shown

The results in Figure 4.3.a show that the C_{rim}-metal interaction becomes significantly weaker (at least ~0.5 eV/atom) as O is added to both surfaces. For the partially oxidized surface (S1) the binding energy becomes linearly weaker until a concentration of 0.16 ML. For the partially oxidized surface with added C atoms (S2), the binding strength remains constant for the first O addition, and then becomes linearly weaker at a slightly higher rate until 0.16ML of O. Interestingly, this concentration threshold for energy can be understood from the charge analysis. Figure 4.3.b reveals a charge transfer between C_{rim} and surface Fe after 0.16 ML, where the rim provides electrons to the Fe and O atoms in the proximity of a new C_{rim}-O covalent bond. The stabilization in the interfacial energy between 0.16 – 0.24 ML is induced by the formation of multiple C_{rim}-O covalent bonds, as visualized in Figure 4.3.c through the charge density difference (CDD) analysis. The average distances from the surface to the C_{rim} and the nascent shell's top slightly rise, suggesting that the cap lift-off may be favored because of a stable oxide edge formation.

The charge density difference was calculated by subtracting the electron density of the combined *Fe+O+Shell* system ($\Delta\rho_{sys}$) to the individual unperturbed electron density of the partially oxidized slab ($\Delta\rho_{Fe+O}$) and the nascent shell ($\Delta\rho_{shell}$). The electron depletion and accumulation areas (Figure 4.4) indicate a loss of electrons from the surface and the bulk carbon towards the rim C and the formation of three C-O bonds for the concentrations $\geq$ 0.16 ML. The decrease in the interfacial energy and the formation of an oxidized rim allow us to organize the structures and classify them according to the type of interaction between the carbon rim and oxygen.

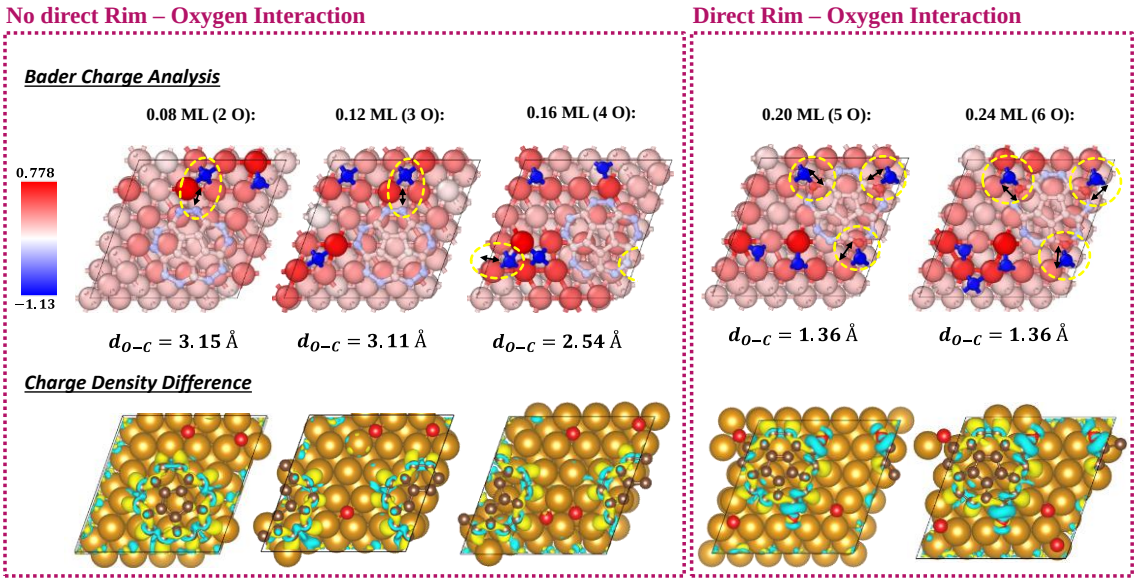

Figure 4.4. Charge density difference and Bader Analysis of the S1 oxidized surfaces. The color shows the Badder charge of all atoms in a range of -1.13 $\mathbf{e}^-$ to 0.78 $\mathbf{e}^-$ using a scale from blue to red respectively, where the O atoms present the highest electron charge ($\approx$ 1.1 $\mathbf{e}^-$) and the oxidized Fe atoms the lowest. The closest carbon-oxygen distance ($\mathbf{d_{O-C}}$) for eah system is highlighted on a yellow circle. Color Code for the CDD: yellow: electron depletion; cyan: accumulation.

Bader charge analysis (Figure 4.3.b and Figure 4.4) indicates that after every O insertion in the [0.08-0.16] ML concentration, the Fe atoms surrounding the adsorbed O are slightly oxidized, whereas O and C_{rim}'s atoms have the highest accumulation of electrons. After 0.16 ML concentration, covalent C_{rim}-O bonds are formed (detailed in Figure 4.5), and the closest carbon-oxygen distance (d_{O-C}), as shown in Figure 4.4, decreases from values higher than 3 to 1.36 Å. The Fe surface reduction and C_{rim} oxidation also reflect the bond formation at higher O concentrations (> 0.16ML). In contrast, the bulk iron and sp^2 bulk carbon atoms remain with a charge approximately neutral for the complete O concentration range.

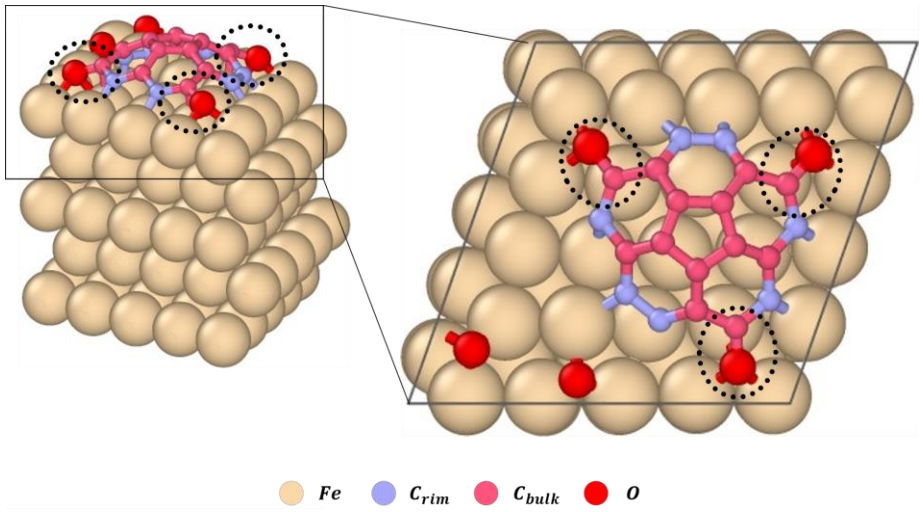

Figure 4.5. Crim – Oxygen bonds at 0.2 ML O concentration. Three C-O bonds are formed (above 0.16ML concentration) causing interfacial energy stabilization and charge transfer.

4.3.2 Evolution of a Spreading Carbon Shell

Here we evaluate the energetics of C addition to a carbon shell adsorbed on the surface. We assume C atoms are available on the surface due to catalysis of a C-containing precursor gas on the metal particle. We model the carbon cap spreading by sequentially adding C atoms to the shell's rim (Figure 4.1) and examining the interfacial energy evolution with the surface. The 0.16 ML O coverage, where there is a transition to a regime where C_{rim}-O bonds are formed, was selected to calculate the interaction strength at different spreading stages. Figure 4.6 indicates the procedure followed to obtain the spreading structures.

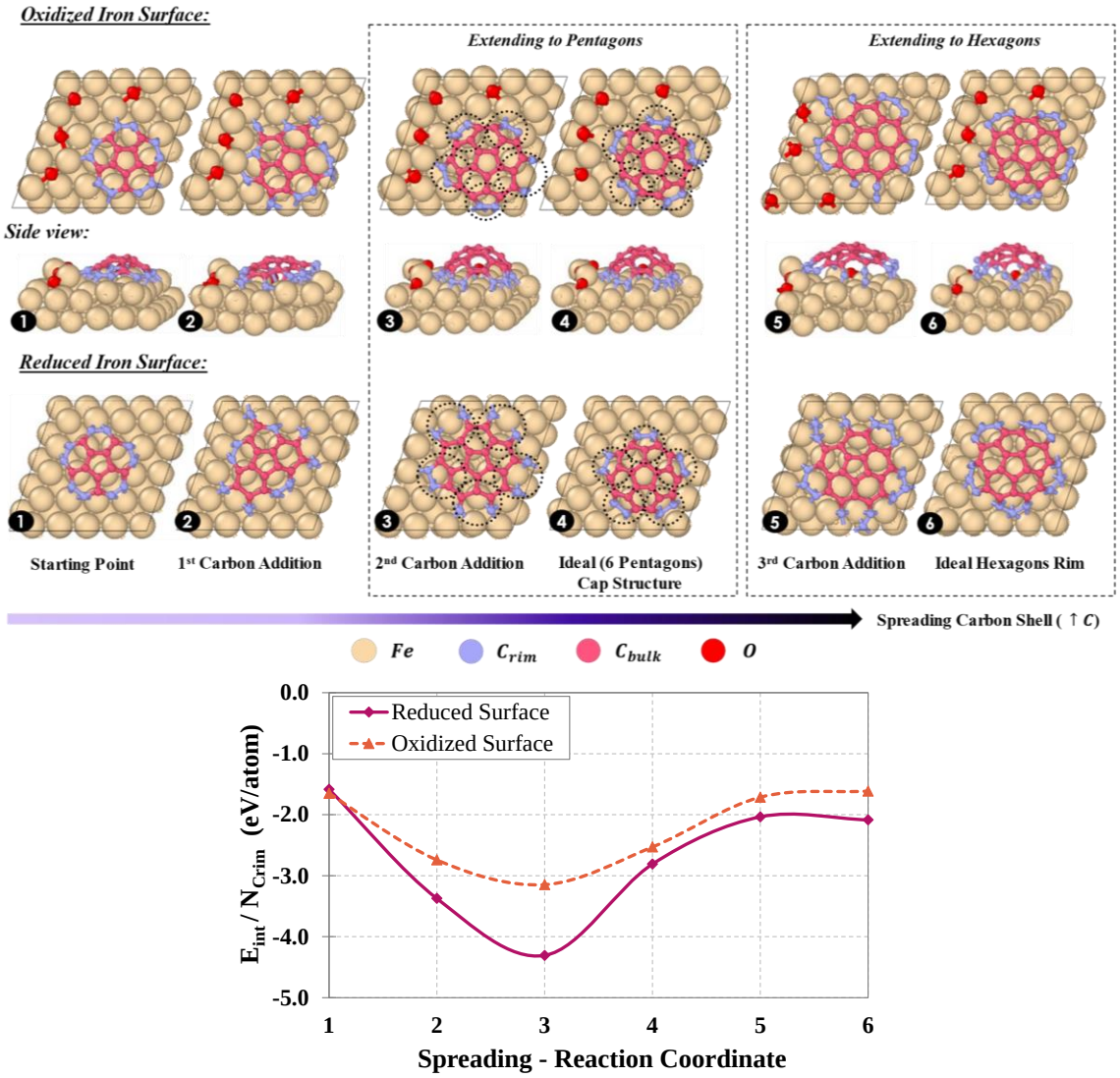

Figure 4.6. Carbon shell spreading on a reduced and partially oxidized (0.16 ML) iron surface.[Top] The structure evolves to a pentagon-rich and then hexagon-rich edge after increasing the amount of carbon in the active area. Side view only includes the first two upper iron layers and the carbon shell. [Bottom] Interfacial energy evolution during the different stages of spreading and cap formation.

We observed that the carbon shell's symmetry breaks after the first addition cycle, allowing the new carbon atoms to pick the edge site that lowers the overall system energy. The second C addition facilitates the formation of new pentagons, helping to the

probable cap's stabilization via curvature energy. A third C addition cycle accounts for a continued spreading of the shell by creating new hexagons in the rim. The E_{int}/C_{rim} evolution while extending to a fully or semi-formed cap (structures 3 & 4), and a carbon structure with hexagons in the rim (structures 5 & 6) is observed in Figure 4.6-Top. "Ideal" or perfectly formed structures were obtained from an AC (5,5) tube's cap (Figure 4.6 – structure 4) and a carbon shell of cone shape (Figure 4.6 – structure 6).

Oxygen atoms create surface instability and atomic reorganization that restricts the carbon shell spreading to the area enclosed by the oxidized surface, consistently favoring closed pentagons' development in the rim (Figure 4.6 - structure 3, top). Contrarily, the carbon shell spreading on the reduced iron surface produces open pentagons that can evolve quickly into a wider carbon shell, favoring the surface spreading over nucleation and potentially larger diameters (Figure 4.6 - structure 3, bottom). The carbon shell consistently had weaker interfacial binding strength on the oxidized surface with a margin > 1 eV for the most stable structure while spreading (see "3" in the energy profile shown in Figure 4.6). The energy profile shows that the formation of pentagons at the structure's rim creates the strongest rim-metal interaction in both oxidized and reduced surfaces. This strong attachment supports the idea that once the cap has lifted and under constant temperature, the SWCNT starts growing vertically instead of spreading on the surface.

The formation of consistent tube diameter distributions, independent of catalyst size, can find its origins in the previously discussed results. Surface oxygen acts as a promoter for the nucleation, generating narrow diameter distributions and favoring

SWCNT perpendicular growth, even for small iron particles (d < 3nm) as previously observed experimentally[54]. A stable oxidized carbon edge can also help control the spreading within a limited active area. Experiments using oxygen concentration as a reaction parameter have started to show the potential of this SWCNT nucleation promoter in the size[233], shape[233], and orientation of growth[234]. High oxygen concentrations environments allow the formation of iron oxide, decreasing the overall catalyst activity but increasing the SWCNT's diameter distribution[235]. Therefore, we could tune the SWCNT properties if we control the concentration of oxygen on the particle surface, regardless of its source, especially during the pre-nucleation stage.

4.3.3 Energy Corrections and Chirality

We further studied SWCNT's chirality effect on the interaction energy as well as on the evolution from carbon shell to SWCNT. Calculations were performed using the PBE potential without dispersion (ND) and including van der Waals force corrections. Dispersion forces' effect in the interaction were applied as proposed by Grimme et al. [236,237] (DFT-D3). We also used the charge-density dependent method by Steinmann et al. [203,204] (DFT-dDsC) as a comparison. All results follow similar energy trends as shown in Figure 4.7, but a shift in the E_{ads}/C_{rim} profile is observed when including the dispersion correction methods, the interfacial energies become stronger by 1-2 eV.

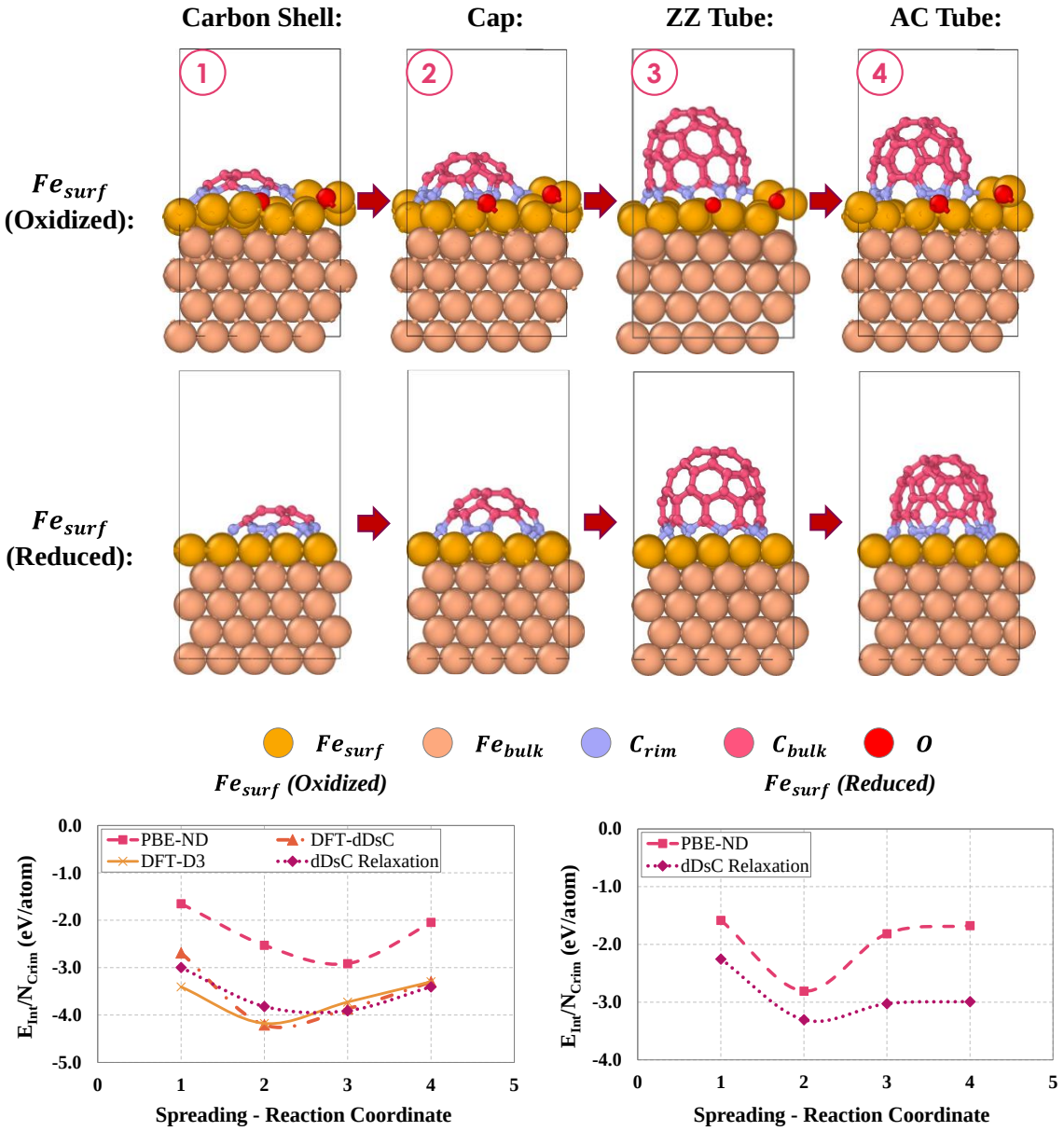

Figure 4.7. Stages of a SWCNT formation.[Top] Evolution from a carbon shell to AC or ZZ SWCNTs. [Bottom] Interfacial energy (E_{Int}/C_{rim}) between carbon structures and iron surfaces, the PBE no dispersion (PBE-ND) energy and dispersion force corrections are shown.

The variation of interfacial energy is a driving factor for chirality selectivity[238,239] and is sometimes related to the surface's symmetry match between the metal and SWCNT[34]. Previous studies investigated the interaction between carbon caps and small

metal particles and exposed a relation between different tube chiralities and the strength of interfacial binding energy.[129,240–242] They showed that both bounds of the chiral angle range (armchair and zigzag tubes) are local energy minima in the SWCNT-catalyst contact interaction. In other words, chiral tubes usually present more 'kinks' or edge imperfections that strengthen the metal – carbon interaction compared with achiral tubes (AC and ZZ). In our study, interfacial energy per C_{rim} (Eq. 4.1) is higher for a ZZ (9,0)-SWCNT, with a value of 2.05 eV compared to 1.94 eV of the AC (5,5)-SWCNT on the oxidized surface. This agrees with previous observations of a stronger carbon-metal interaction between zigzag (ZZ) tubes and nickel or cobalt particles.[129,241,242] This stronger interaction energy usually translates in a similar high energy barrier for the vertical growth, and a near-armchair chirality preference for the resulting nanotube.

4.4 Conclusions

During the first SWCNT formation stages (i.e., spreading and nucleation) we determined that oxygen is an effective promoter for the SWCNT nucleation on the iron catalyst surface. The presence of > 0.16 ML of O on the surface reduces the strength of interaction between the early pre-nucleated cap structure and the metal surface. Therefore, it allows to stabilize the cap, helping with its lift-off. Additionally, as Burgos et al. [206,243] demonstrated, a reduction in the C-metal interaction energy positively affects nucleation vs encapsulation rates.

The spreading evolution of a carbon shell to become a cap had a lower energy path in the oxidized surface. We observed the preferred formation of closed pentagons in the oxidized surface while expanding to a structure similar to the AC(5,5) SWCNT's cap

(Figure 4.6). The surface oxygen in the catalyst particle also limits the active area for SWCNTs' formation. Strong carbon-oxygen bonds are formed when the rim enters in direct contact with the oxidized area (Figures 4.4-5). The reduction of the active growth area, charge transfer, and the lower C-metal interaction strength can explain previously discussed experimental results adding an oxygen source for the controllability of SWCNT properties[53,54,224,233,234]. One noteworthy example is the consistent diameter distributions obtained independently of catalyst size[54]. Knowing the role of crucial intermediate catalyst surface species like partially oxidized surfaces could help improve SWCNTs' selectivity and purity during large-scale production. The discussed results open a new perspective in understanding SWCNT nucleation on metal catalyst particles and the intrinsically related SWCNT diameter-chirality properties.

CHAPTER V

EFFECT OF COBALT CARBIDE BULK AND SURFACE COMPOSITION ON THE CATALYST REACTIVITY DURING SWCNT FORMATION

5.1 Introduction

Studies of the bonding and reactivity of precursor molecules adsorbed on transition metal surfaces are essential for a molecular-level understanding of heterogeneous hydrocarbon catalysis and single-walled carbon nanotube (SWCNT) growth. Cobalt and its carbide phases are commonly used for hydrocarbon formation reactions like the Fischer–Tropsch Synthesis (FTS),[244] and the production of SWCNTs through chemical vapor deposition (CVD)[245].

Using CVD, SWCNTs are produced through the catalytic dissociation of hydrocarbons (C_xH_y),[246,247] alcohols,[248,249] carbon oxides[25,51,250] (i.e., CO and CO_2) and different types of reaction enhancers[68] or byproducts[251] (e.g., H_2O, H_2S, O_2, H_2). Carbon monoxide (CO) has shown great ability to produce homogeneous distributions of selective chiral nanotubes.[54,223,224] Dai et al[51], first reported the SWCNT production using CO disproportionation. Later, the HipCo process[25] and the floating catalyst CVD method[236,252], have shown remarkable progress towards commercial and large-scale applications. Acetylene gas (C_2H_2) has been widely used for studies on the SWCNT formation,[253] mechanism[39] and diameter-chirality control;[254] this precursor is especially useful due to a low dissociation temperature and high reactivity[245]. Control over SWCNT properties (e.g., chirality and diameter) is fundamental for practical

applications that could exploit SWCNTs' extraordinary electronic, mechanical, and optical properties.[255,256]

Since the SWCNT discovery, there has been an increasing interest in the state, and active phase of catalysts during SWCNT formation, especially for the iron catalyst family (i.e., Fe, Ni, Co). The carbon-metal reaction mechanism and the actual composition of the catalyst during the growth of CNTs have been extensively debated.[195,245,257–262] For example, most cobalt phases (i.e., Co, Co_2C, and Co_3C) have been reported as the active phase of the Co catalysts for CNT formation.[201,223,263–265]. Both stable cobalt phases (i.e., Co_2C and Co_3C) are metastable with formation energies between nickel carbide and iron carbide.[257]

Catalyst evolution is expected during the SWCNT formation and nucleation (e.g., catalyst shape, composition, and crystal planes).[263] Lately, SWCNTs nucleation has been attributed to fluctuations in the strength of interaction between graphitic carbon and the different exposed crystal planes of the metal nanoparticle.[148] Multiple coupled interactions inherent to the reaction conditions (e.g., metal particle, substrate, precursor gas, feed rate, etc.) affect the SWCNTs' final yield and structure.[62,266,267]

Recent experimental observations[268] reporting a reduced activity in the cobalt catalyst surface due to carbide phase fluctuations (i.e., Co_2C and Co_3C) require further insight. Here we use cobalt carbide stable phases Co_2C and Co_3C to study the effects of variable bulk composition and surface termination on the precursor decomposition and tube-metal interactions. We analyzed the interaction strength of the surface with C_2H_2 and CO adsorbates, and we characterized their reactivity by evaluating the dissociation

energy barriers of these precursor molecules on the metal carbide surfaces. Furthermore, the carbon deposition using the Boudouard reaction mechanism and the rim-metal interaction for armchair and zigzag SWCNTs were also studied.

5.2 Methodology

We calculated adsorption and activation energies for the dissociation reaction of C_2H_2 and CO on cobalt carbide slabs with two bulk compositions (Co_2C and Co_3C) and various exposed crystal planes. The exposed facets were selected from a previous analysis[148] based on comparisons between experimental and theoretical observations for SWCNT growth and termination. Figure 5.1 shows the pure cobalt (Co-top) and carbide (CoC-top) surface terminations. We used a (2x2) supercell for both Co_2C planes and the Co_3C (020) surface and a (1x1) unit cell for Co_3C (111). The lattice parameters for the unit (1x1) cells are presented in Table 5.1. We analyzed different adsorption sites (Appendix C) to find the structure with the most stable interaction for each precursor gas.

Table 5.1. Lattice parameters a, b, and c corresponding to the length of unit vectors in the x y plane and z-direction respectively, for the cobalt carbide unit (1x1) cell.

Surface	***axb*xc**
Co_2C (011), Co-top	4.16 x 5.28 x 19.24
Co_2C (011), CoC-top	4.16 x 5.28 x 18.96
Co_3C (111), Co-top	7.02 x 7.07 x 18.50
Co_3C (020), CoC-top	4.24 x 4.85 x 18.15

The carbon-metal interfacial interaction energies (E_{int}) of armchair (AC) and zigzag (ZZ) SWCNTs in contact with different types of Co_2C surfaces, and sites defined following the anchoring vs. liftoff classification[148,201] (Fig. 5.1) were calculated as follows:

$$E_{int} = (E_{sys} - E_{slab} - E_{SWCNT})/N_{C_{rim}} \qquad (5.1)$$

We increased the system's size for the SWCNT-metal calculations and used a (3x3) supercell for the Co_2C and Co_3C surfaces to avoid further interaction with the periodic images. Additionally, the z lattice parameter was changed to 21 Å for all systems.

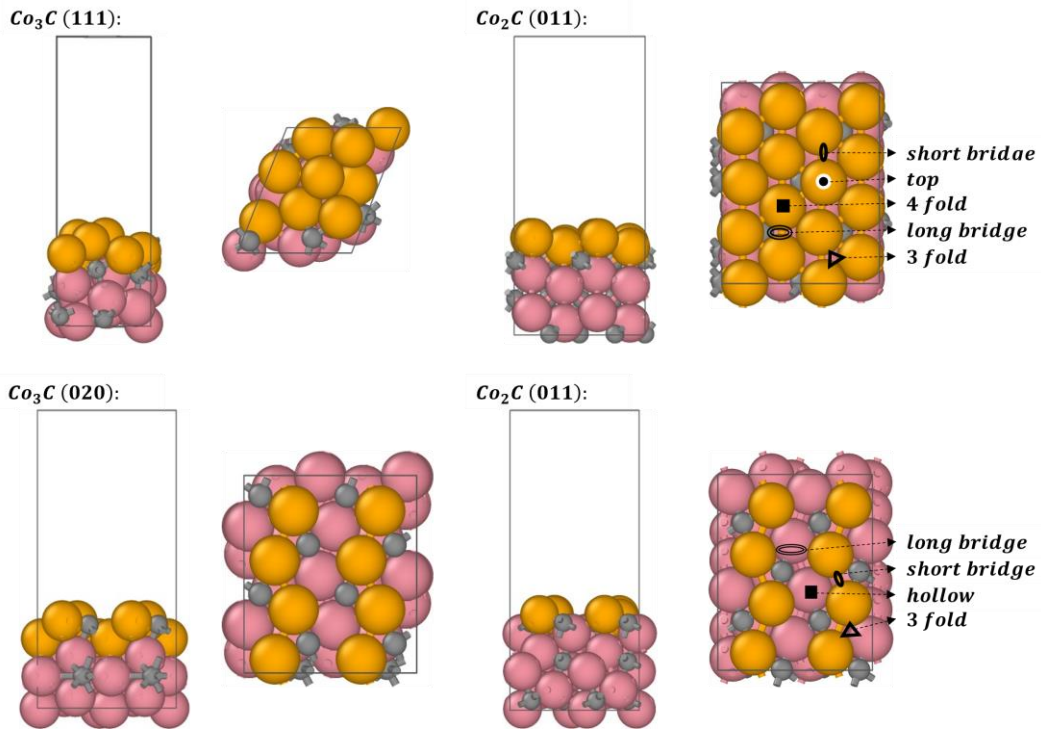

Figure 5.1. Cobalt carbide slabs and adsorption sites used in the precursor gas reaction calculations. Co_2C (011) and Co_3C (111) correspond to the Co-top surface termination. Co_2C (011) and Co_3C (020) correspond to the CoC-top termination. Color code: surface Co: orange; subsurface Co: pink. Carbon: grey.

The gamma-centered Monkhorst-Pack scheme[186] was used for the Brillouin zone's k-point sampling with a grid 4x4x1 for the precursor gas reaction calculations and 4x4x2 for the SWCNT-metal interaction energies. The exchange-correlation functional given by the Perdew-Burke-Ernzerhof approximation[184] and the Projector Augmented Wave Method[167,185] was employed for calculating core-electron energies with a cutoff energy of 700 eV. Long-range interactions were modeled using the Grimme dispersion D3 method[237] with the Becke-Jonson (BJ) damping function[237]. We performed all DFT energy calculations with an electronic convergence tolerance of $1x10^{-6}$ eV and ionic convergence on the total energy of $1x10^{-3}$ eV using the Vienna Ab Initio Simulation Package (VASP)[230].

5.3 Results

C_2H_2 and CO molecules were adsorbed in multiple positions sites on top of the cobalt carbide surface (Appendix C, Figure C1). Table 5.2, shows the adsorption energy values of the sites with strongest interaction (Figure 5.2 and 5.3). Both precursor gases showed a general preference for the adsorption on the short bridge site or the three-fold hollow position, as shown in Figures 5.2 and 5.3.

Table 5.2. Adsorption Energies (eV) for C_2H_2 and CO on top of cobalt carbide surfaces with (011), (020) and (111) facets and different surface terminations. The corresponding facet is next to the adsorption energy value.

Cobalt Carbide Surfaces	**Acetylene (C_2H_2)**		**Carbon Monoxide (CO)**	
	Co -top	**CoC-top**	**Co-top**	**CoC-top**
Co_2C	-3.59; [011]	-2.45;[011]	-2.30; [011]	-2.45; [011]
Co_3C	-2.80; [111]	-1.83; [020]	-2.24; [111]	-1.83; [011]

We can observe that Co-top terminations produce a generally stronger interaction with C_2H_2 and CO in all evaluated crystal facets. These values are within the range of previously reported works for acetylene and carbon monoxide.[269]. Only the $Co_2C(011)$-Co-top surface presents a break of this trend with a slight increase of 0.15 eV in the CO adsorption (-2.30 eV), favoring the attachment to a CoC-top surface termination (-2.45 eV). Dong et al.[269], in a comparative study between carbide and metallic Co surfaces, reported that for some alkenes (i.e. ethylene and propylene) and CO, there is a more stable interaction with Co_2C than with pure Co. Similarly, we observe a stronger strength of interaction directly related to the bulk structure composition.

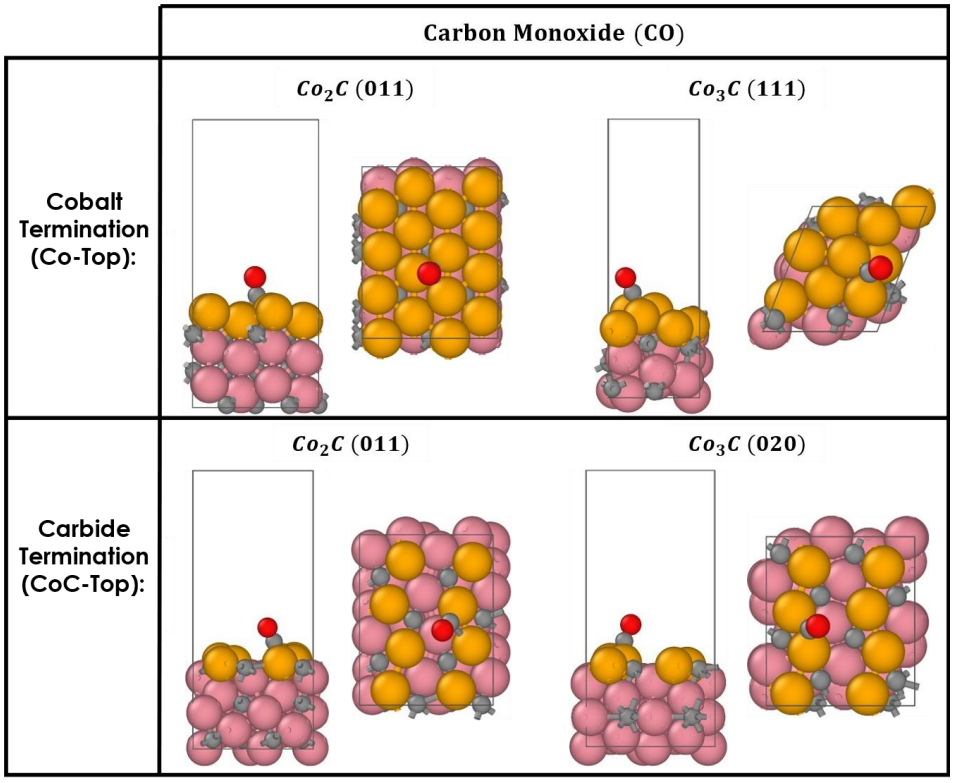

Figure 5.2. CO adsorption site at the strongest interaction with the cobalt carbide surface. Color code: surface Co: orange; subsurface Co: pink. Carbon: grey. Oxygen: red.

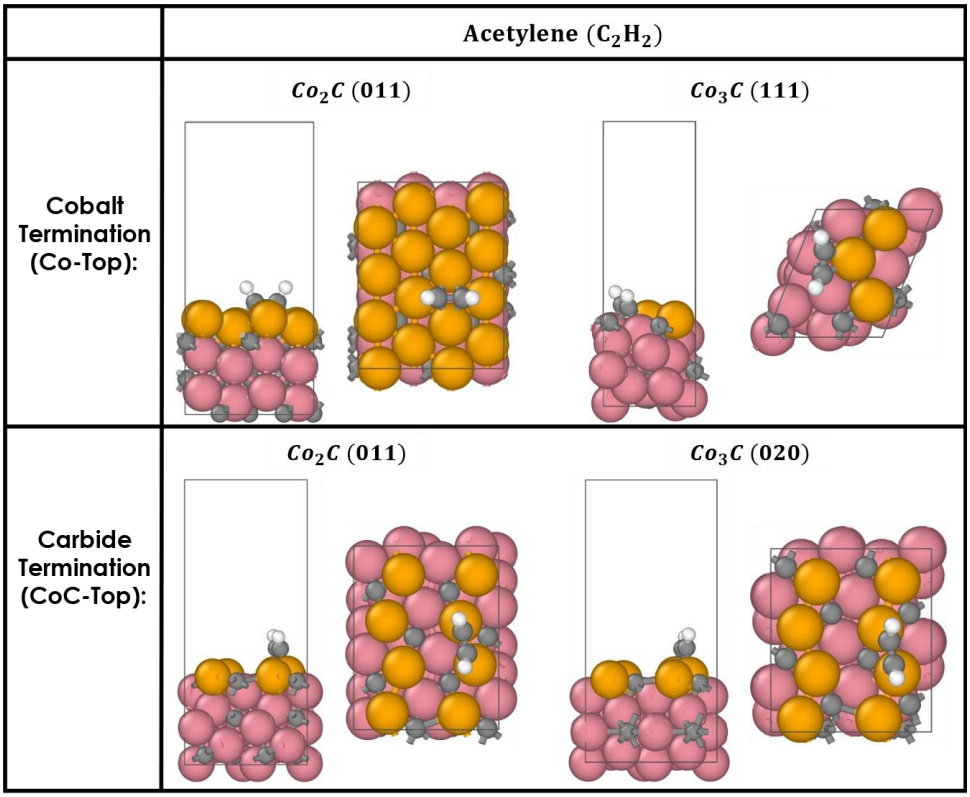

Figure 5.3. C_2H_2 adsorption site at the strongest interaction with the cobalt carbide surface. Color code: surface Co: orange; subsurface Co: pink. Carbon: grey. Hydrogen: white.

In our results, Co_2C shows an enhanced attachment for both precursor gas molecules compared with Co_3C. For C_2H_2, the adsorption energy increase was approximately 17 to 19 %, accounting for all interacting systems (Appendix C). The increase was similar in both terminations, with Co-top presenting a slight enhancement (2-3% higher) than the CoC-top. In the same way, the adsorption energy for CO increased a 19.5% in the most stable position for the CoC-top termination, but only 2.9% for the Co-top termination. $Co_3C(111)$ with a dense metallic Co termination and a stepped-like surface allows for close metal-precursor contact, counteracting the reduced

interaction associated with the bulk composition and facilitating the precursor dissociation.

5.3.1 Dissociation Reactions

The dissociation reaction of precursor gases on the catalyst surface is crucial in forming a new carbon compound. For SWCNT, the precursor feeding rate to the reactive system and the dissociation rate of that carbon-rich precursor in the catalyst surface are both very important.[266,270] A high dissociation rate may result in complete catalyst deactivation,[148,268], and a low rate may decrease the yield[271]. For this reason, we decided to study the activation energies for C_2H_2 dehydrogenation and CO decomposition. Those reactions are two of the most common paths to obtain carbon for nanotube nucleation and growth.

5.3.1.1 Acetylene Dehydrogenation

The mechanism for acetylene dehydrogenation on cobalt, cobalt carbide and other iron family catalysts is reported in several publications[272–275]. In general, hydrogen disproportionation is favored over the C-C bond breaking. We calculated the energy barrier associated with the H-C and C-C dissociation to measure the effect of bulk composition and surface termination on this reaction mechanism. The reaction path is shown in Figures 5.4 and 5.5 for the four systems.

We used the C_2H_2 molecule in the adsorption site with the shortest H-Co distance as the initial system due to a preliminary analysis of the activation energy for the H-C bond dissociation. The preliminary analysis showed that H atoms at the most stable adsorption sites for C_2H_2 are further apart from the catalyst. Therefore, the necessary

bond rotation for hydrogen to reach the surface is energetically costly (1 - 3 eV) due to repulsion from the partially positive charged surface (Figure 5.7). The surface diffusion energy barrier for C_2H_2 is observed to be in the 0.2 – 0.5 eV range. This low diffusion barrier could allow the C_2H_2 molecule to find an optimal adsorption site to dissociate.

Activation energies for the C_2H_2 dehydrogenation (Figure 5.6) show that the first H-C dissociation (i.e., $C_2H_2 \rightarrow C_2H + H$) present the overall lower energy barriers. Co_3C surfaces present the highest energy barriers (0.85 - 0.95 eV) for the first H disproportionation reaction compared with Co_2C surfaces (0.54 – 0.56 eV). Additionally, the reaction is endothermic for Co3C surfaces and exothermic for Co2C. Our calculations found that four-fold and three-fold adsorption sites on the Co-top surfaces and hollow sites on the CoC-top surfaces showed lower activation energies and, therefore, the best conditions for dehydrogenation.

The second H-C dissociation (i.e., $C_2H \rightarrow C_2 + H$) showed a considerable increase in the energy barriers (0.81- 1.36 eV). In this second part of the reaction pathway, the surface termination seems to have a more substantial impact. We can observe that Co-top surfaces have higher activation energies compared with the CoC-top termination. After the first dissociation, the remaining C_2H fragment is further polarized, and H loses electrons. The enlarged positive charge for the remaining H atom creates a repulsive force with the Co surface, increasing the dissociation energy barriers. This repulsive force is counteracted by the highly negative charged carbon surface atoms (C_{sfc}) in the CoC-top termination.

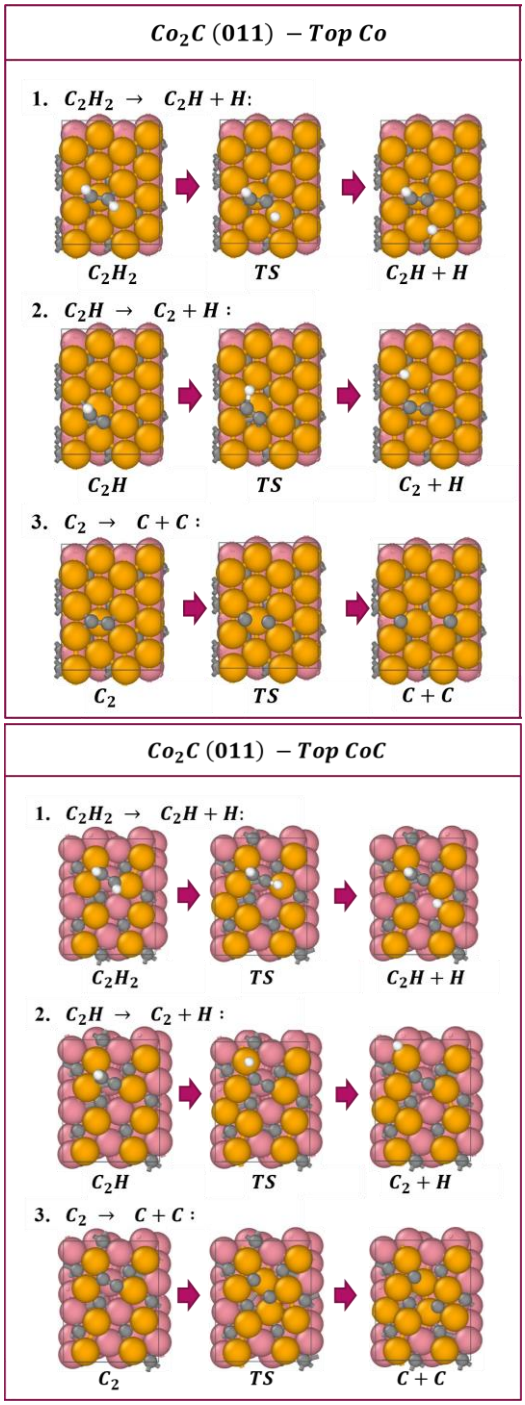

Figure 5.4. Reaction pathway for the dehydrogenation reaction of C_2H_2 on Co_2C. [Top] H-C dissociation reactions and the C-C bond breaking for the $Co_2C(011)$ with Co-top termination. [Bottom] H-C dissociation reactions and the C-C bond breaking for the Co_2C (011) with CoC-top termination. Color code: surface Co: orange; subsurface Co: pink. Carbon: grey. Hydrogen: white.

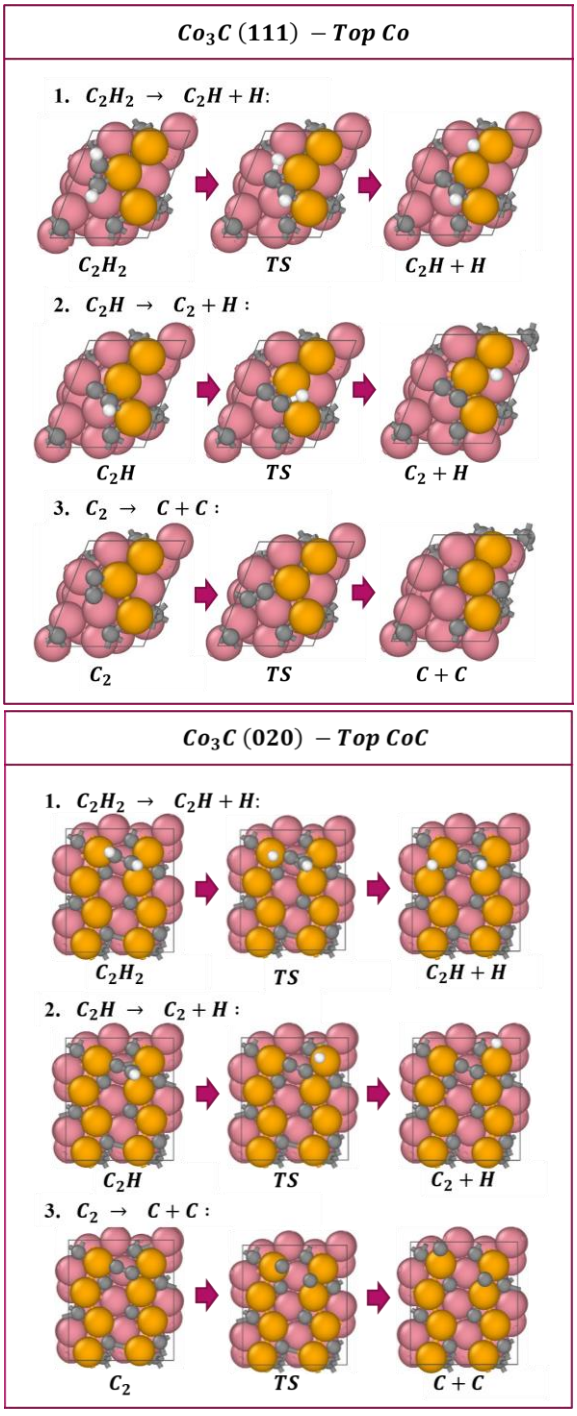

Figure 5.5. Reaction pathway for the dehydrogenation reaction of C_2H_2 on Co_3C. [Top] H-C dissociation reactions and the C-C bond breaking for the Co_3C(111) with Co-top termination. [Bottom] H-C dissociation reactions and the C-C bond breaking for the Co_3C (020) with CoC-top termination. Color code: surface Co: orange; subsurface Co: pink. Carbon: grey. Hydrogen: white.

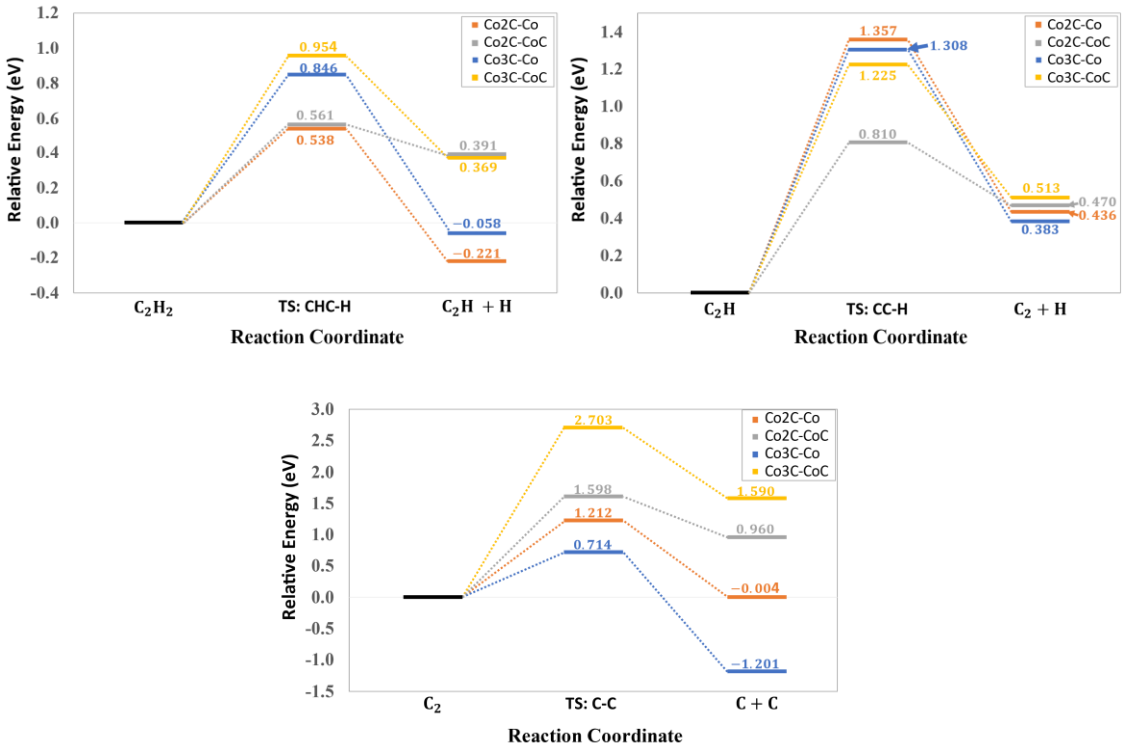

Figure 5.6. Activation and reaction energies for the dehydrogenation of C_2H_2 on Co2C(011) with Co-top and CoC-top terminations, Co3C(111)-Co-top and Co3C(020)-CoC-top terminations. The relative energy values were calculated with respect to the initial system energy.

Previous works have shown that C_2 can exist in this dimer form on the catalyst surface and interact with other free carbon atoms or graphitic structures (e.g., SWCNTs) without the need to dissociate.[273,274] Nevertheless, the C-C bond dissociation's energy barrier can be easily reached at high temperatures and preferentially on certain crystal planes. The results show that the Co-top surfaces present lower energy barriers for the C-C bond breaking (0.71 - 1.21 eV). It is reasonable that a semi-saturated carbide surface shows higher resistance to dissolve additional free carbon. Additionally, the negatively

charged C_{surf} atoms create repulsion forces with the C_2 molecule, making this last reaction step somewhat unstable for CoC-top terminations.

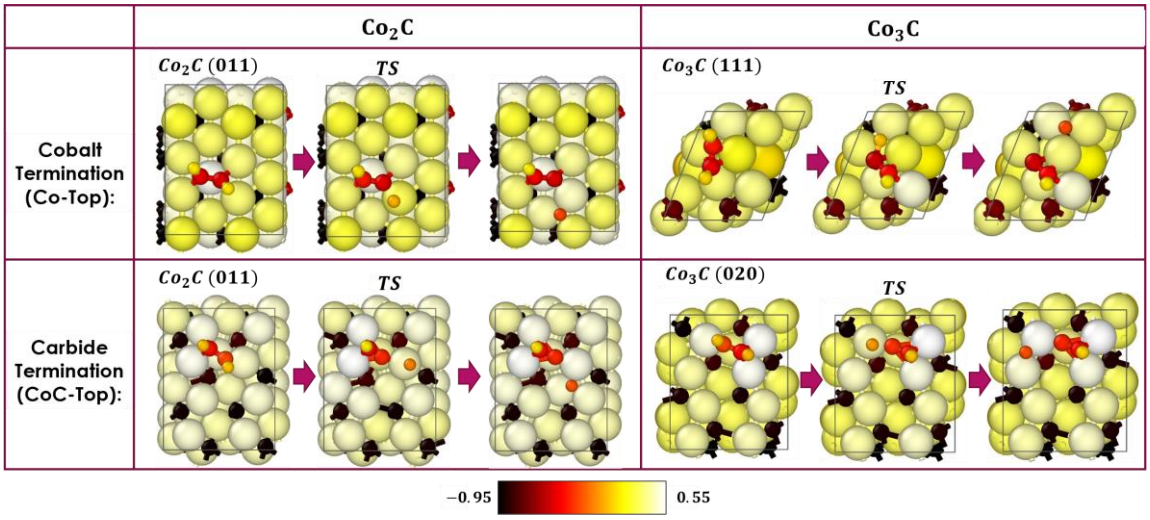

Figure 5.7. Charge distribution of C_2H_2 on top cobalt carbide during the first H-C dissociation. The darker-red color corresponds to positively charged atoms, and the light-yellow color corresponds to the negatively charged atoms.

Table 5.3. Adsorption energy between C_2H_2 and Co2C(011) with Co-top and CoC-top terminations, Co3C(111)-Co-top and Co3C(020)-CoC-top. The cobalt carbide systems' average charge for bulk and surface (sfc) atoms is tabulated before the dissociation reactions.

Surface	Eads (eV)	Eads* (eV)	Co_{sfc} (e^-)	C_{sfc} (e^-)	Co_{Bulk} (e^-)	C_{Bulk} (e^-)	H_{sfc} (e^-)	$C_{2_{sfc}}$ (e^-)
Co_2C-Co	-2.51	-3.59	0.295	-	0.485	-0.813	0.098	-0.471
Co_3C-Co	-2.80	-2.80	0.323	-	0.288	-0.830	0.104	-0.374
Co_2C-CoC	-2.06	-2.45	0.478	-0.883	0.459	-0.912	0.054	-0.283
Co_3C-CoC	-1.59	-1.83	0.478	-0.828	0.262	-0.866	0.054	-0.273

*Adsorption energy on the strongest interaction site

Table 5.3 and Figure 5.7 show the charge distribution in the cobalt carbide surface during the first H-C dissociation. The Co_{sfc} atoms are positively charged, and all

negative charged is distributed between the diluted carbon atoms ($C_{sfc}\ and\ C_{bulk}$), and the acetylene deposited carbon (C_2). Charge analysis allows us to understand some general trends in the C_2H_2 dissociation reactions. For example, during the H-C dissociation, the negatively charged C_{sfc} atoms in the CoC-top termination donate electrons to the H, facilitating the H-C bond breaking.

5.3.1.2 CO Dissociation

The dissociative reaction of CO on cobalt has been studied especially for FTS conditions.[276] It has been found that hydrogen-assisted dissociation on cobalt has lower activation energies than the direct C-O dissociation.[277,278] However, the production of SWCNTs using CO disproportionation generally is usually free of hydrogen supply.[25,51,250] Dihydrogen (H_2) addition to the SWCNT synthesis reaction may produce herringbone helical structures[279] (i.e., carbon nanofibers) instead of SWCNTs or coaxial MWCNTs.[264] The results show that C-O dissociation has energy barriers in the range of 1.74 -2.74 eV for the cobalt carbide slabs with Co-top terminations and 3.64 – 3.77 eV for CoC-top terminations. Therefore, CO is preferentially dissociated on Co-top terminations. The stepped-like surface Co_3C (111) with Co-top termination showed the lowest activation energy (1.74 eV) and exothermic behavior.

The significant increase in the activation energy for CoC-top terminations may be associated with the repulsion of highly negatively charged C_{sfc} atoms and the competition for active sites in the semi-saturated carbonaceous surface (Figure 5.8).

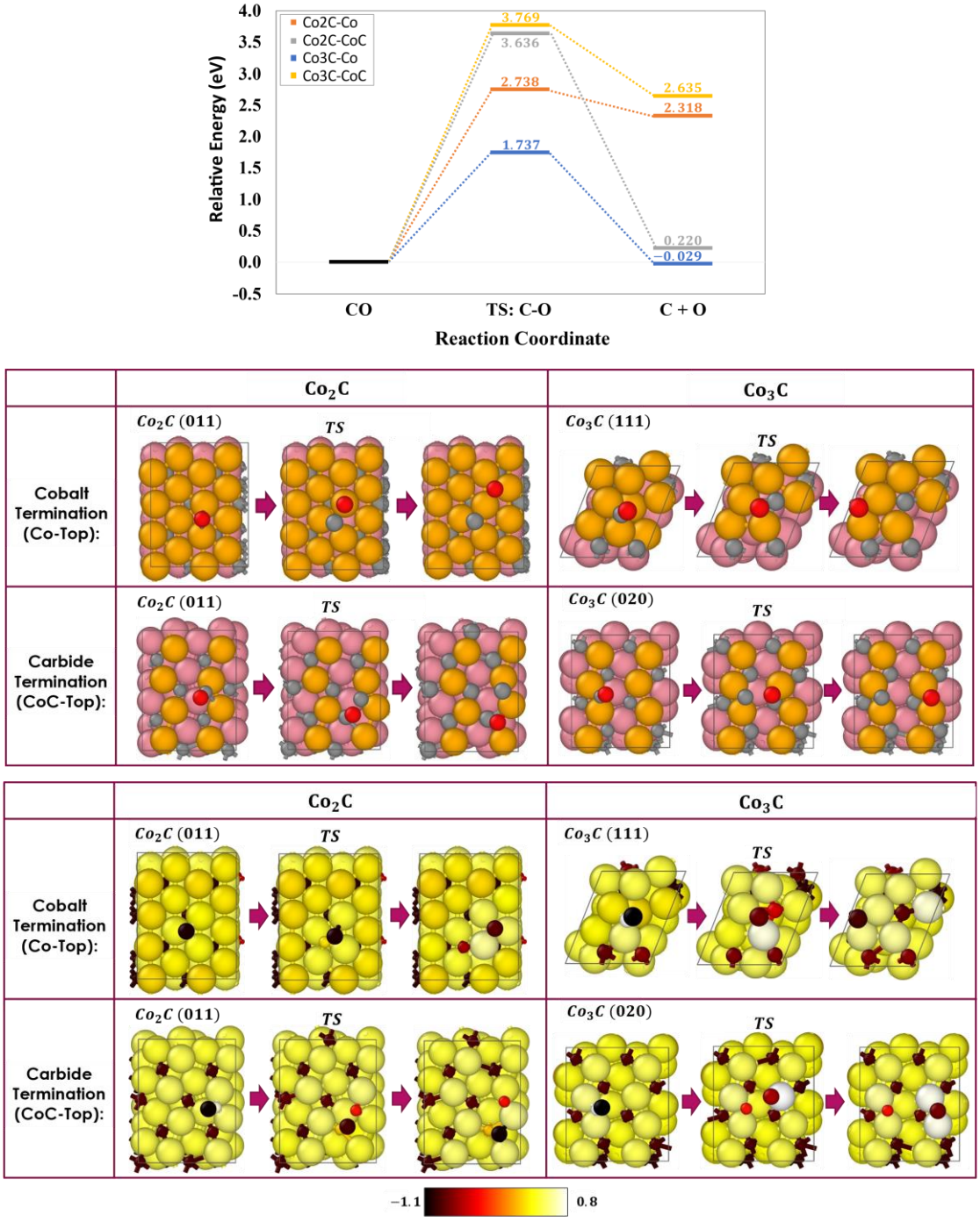

Figure 5.8. [Top] Activation (Ea) and reaction energies (ΔG_{rxn}) for C-O dissociation. [Bottom] a.) CO dissociation reaction mechanism on Co2C and Co3C surfaces; b.) Charge distribution during the C-O bond breaking. Color code: surface Co: orange; subsurface Co: pink. Carbon: grey. Oxygen: red.

Table 5.4. Adsorption (Eads), activation ($\boldsymbol{E_a}$), and reaction ($\boldsymbol{\Delta G}$) energies for CO in the cobalt carbide surfaces.

Surface	E_{ads} (eV)	E_a (eV)	ΔG (eV)
Co_2C – Co-top	-2.30	2.74	2.32
Co_3C – Co-top	-2.24	1.74	-0.03
Co_2C – CoC-top	-2.45	3.64	0.22
Co_3C – CoC-top	-1.84	3.77	2.64

Adsorption energies for the CO chemisorption are in the range of -2.45 to -1.84 eV. The strong interaction of CO with the carbide surface is observed throughout all bulk compositions and terminations, as shown in Table 5.4. Previous experimental and DFT calculations have found the same trends for direct CO dissociation on Co2C surfaces with energy barriers in the range of 1.49 – 2.49 eV.[269,278] For this direct C-O bond breaking mechanism, the surface structure seems to have a more significant impact than the bulk composition contribution.

5.3.2 Boudouard Reaction

The CO disproportionation (i.e., Boudouard reaction: $2CO \leftrightarrow CO_2 + C$) is the primary source of C deposition during the SCWNT formation using CO/CO_2 mixtures as the precursor gas.[51,54] The mechanism studied here corresponds to the reaction between two adsorbed CO molecules. We can observe from the results (Figure 5.9) that the reaction is highly endothermic for all four cobalt carbide systems and with slightly unfavorable energy barriers (2.75 – 6 eV).

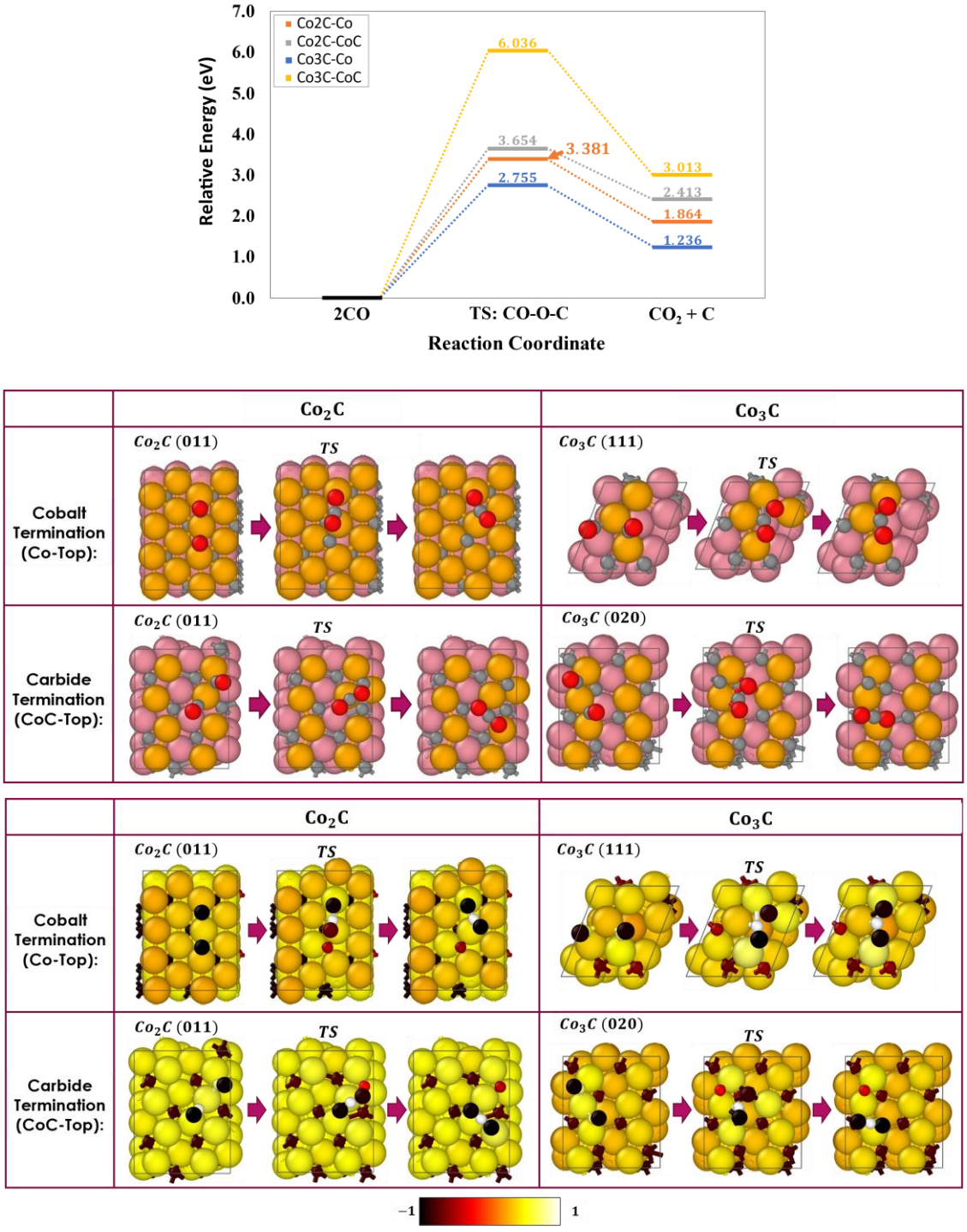

Figure 5.9. **[**[Top] Activation (Ea) and reaction energies ($\boldsymbol{\Delta G_{rxn}}$) for CO disproportionation. [Bottom] a.) CO disproportionation reaction mechanism on Co2C and Co3C surfaces; b.) Charge distribution during the C-O bond breaking. Color code: surface Co: orange; subsurface Co: pink. Carbon: grey. Oxygen: red.

Using the mechanism shown here (Figure 5.9), we observe that the predominant contribution determining the reactivity of the surface for the Buodouard reaction seems to be the surface termination. We also observe that the activation energy correlates closely to the adsorption energy of CO in the carbide surface (Table 5.4). For example, the weakest CO-metal interaction on $Co_3C(020)$ also shows an activation energy of 6 eV. This energy barrier is as high as the excitation energy of CO on the gas phase.[280]

It is known that CO disproportionation occurs on cobalt particles.[264,281] However, these high energy barriers and mostly endothermic behavior for the disproportionation reaction observed in our results may be related to unaccounted CO coverage effects and finite-size (particle) contributions. Peressi[282] reported that the direct C-O dissociation and CO disproportionation became more favorable (i.e., low activation energies) and exothermic using high coverage concentrations on small particle catalysts instead of single-crystal slabs. Furthermore, the use of a substrate slightly enhances the surface reactivity of the catalyst particle.[84,282] The main reason could be that the pure carbide surfaces are not favorable for the reaction. Previous work determined that there is a gradient of carbon concentration for active catalysts that leaves Co atoms at the top of the surface.[148,263] Thus, even if the catalyst has an overall carbide composition, the C distribution allows the particle to be still active. On the other hand, Co_3C surfaces are known to be inactive.[268]

5.3.3 SWCNT – Catalyst interactions

We studied interaction energies between nucleated achiral SWCNTs (AC and ZZ) and six cobalt carbide surfaces, Co_2C (020), Co_2C (011), and Co_3C (020), each with the

Co-top and CoC-top surface terminations. In a recent study by Chao et al.[268], Co_2C was the predominant active catalyst during SWCNT nucleation. Co_3C has been reported as both inactive[148,268] and the preferred[257] phase for CNT nucleation. Wang et al.,[257] pointed that the Co_2C phase might only exist during the growth of small SWCNTs using thermodynamic analysis of the free energies in the three stable phases (i.e., Co, Co2C, and Co3C). For MWCNT conditions Co_3C seem to be the preferred phase.[257] Figure 5.10 shows the SWCNTs interacting with the cobalt surfaces.

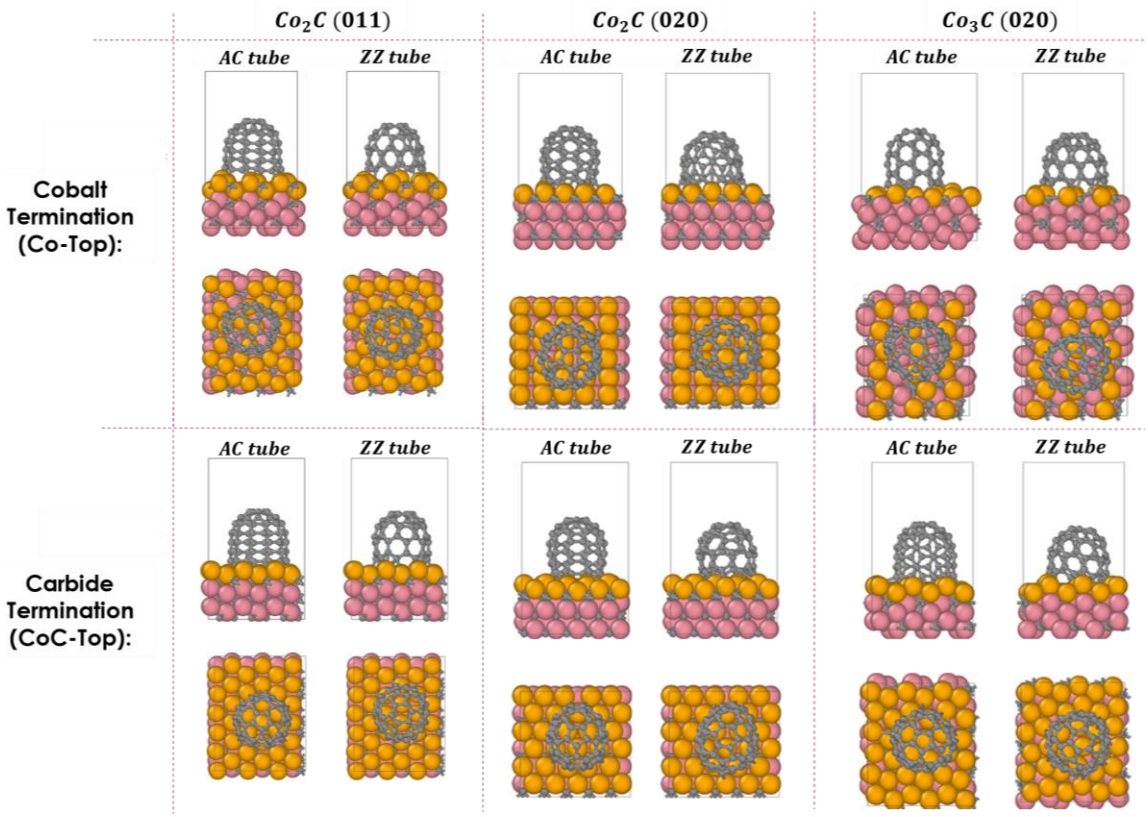

Figure 5.10. AC(5,5) and ZZ(9,0) SWCNTs interacting with Co_2C and Co_3C carbide surfaces.

Table 5.5. Adsorption (E_{ads}) and interfacial energies (E_{int}) between AC and ZZ SWCNTs and the cobalt carbide surfaces.

Carbide Surface	Arm-Chair (5,5)		Zig-zag (9,0)	
	E_{ads} (eV)	**E_{int} (eV/atom)**	**E_{ads} (eV)**	**E_{int} (eV/atom)**
Co_2C (020) – Co-top	-22.74	-2.27	-27.74	-3.08
Co_2C (011) – Co-top	-22.65	-2.26	-24.87	-2.76
Co_3C (020) – Co-top	-21.31	-2.13	-27.62	-3.07
Co_2C (020) – CoC-top	-18.16	-1.82	-23.31	-2.59
Co_2C (011) – CoC-top	-15.84	-1.58	-21.16	-2.35
Co_3C (020) – CoC-top	-18.04	-1.80	-23.12	-2.57

Table 5.5 shows the adsorption ($E_{int} * N_{C_{rim}}$) and cobalt-carbon interfacial (Eq. 5.1) energies between the SWCNT and the different carbide surfaces. Those two energy values are measures of the interfacial strength of interaction between the nanotube and surface. We can observe two significant trends: First, both AC and ZZ SCWNTs have a stronger attachment to Co-top surface terminations. Secondly, ZZ tubes present higher interfacial energies compared with the AC tubes.

A liftoff vs. anchor surface classification has been used to describe the catalyst surface interaction with the SWCNT rim.[148,201] The SWCNT is nucleated on a liftoff surface, and this plane is perpendicular to the direction of growth. For active particles, liftoff surfaces have a predominant CoC-top termination while anchor surfaces have mostly Co-top surface termination.[148] We can observe from these results that the low interfacial energy of CoC-top terminations should indeed favor the detachment from the surface, especially if this surface is surrounded by Co-top planes that work as anchors during the SWCNT growth. In previous experimental works, Co2C(020) has been identified both as anchor[201] and liftoff[148] surface, depending on its surface composition.

$$\Delta E_{int} = (E_{int}^{Co} - E_{int}^{CoC}) * 100 / E_{int}^{CoC} \quad \text{(Eq 5.2)}$$

The interaction energy difference (ΔE_{int}) between CoC-top and Co-top surfaces is larger for AC than ZZ tubes. The increase in the interfacial strength (Eq. 5.2) between CoC and Co surfaces is, on average, 28% for AC and 18% for ZZ SWCNTs. Only Co3C(020) remains with a similar ΔE_{int} for both achiral SWCNTs.

5.4 Conclusions

We showed that bulk-associated electron donation and surface terminations play a significant role during cobalt carbide's precursor gas dissociation reactions. For the C_2H_2 dehydrogenation, we showed that each reaction step was facilitated for different conditions. The first H-C dissociation presented lower energy barriers on Co_2C surfaces (Co-top and CoC-top). This barrier reduction is primarily associated with a bulk-electron transfer that enhances the catalyst surface reactivity. In contrast, the second H-C dissociation was mediated by the surface structure. CoC-top terminations presented lower energy barriers due to a reduced repulsion with the remaining H atom in the C2H molecule. The C-C bond breaking was calculated in the range of 0.7 – 2.7 eV. The stepped-like surface Co3(111) showed the lowest energy barrier for C-C dissociation (0.7 eV), and the CoC terminations presented the highest activation energies.

Both C-O dissociation and Boudouard reactions showed a surface structure dependence with high energy barriers (> 2 eV) and mostly endothermic behavior. Further work is necessary to include finite size and CO coverage effects in the energy barriers for those reactions. Co_3C – CoC-top consistently showed the weakest attraction for both precursor gases (i.e., CO and C_2H_2). The enhanced interaction between the

Co_2C surfaces and the precursor gases may be related to a more extensive electron accumulation around the C_{bulk} atoms. This charge segregation in the sub-surface can cause a larger electron exchange between the metal Co_{sfc} and the adsorbed molecules.

Finally, we conclude that interaction energies between similar surface terminations (Co-top or CoC-top) are within a very close range. It is necessary for viable nucleation that adjacent crystal planes have different surface compositions. The large interaction energy difference between Co-top and CoC-top terminations helps to promote the SWCNT cap detachment and growth.

CHAPTER VI

CONCLUSIONS AND FUTURE DIRECTIONS

Numerous aspects of the SWCNT formation and nucleation mechanism on transition metal nanoparticles were studied using first-principles calculations, experimental data, and statistical mechanics. DFT simulations were used to measure interfacial interactions, SWCNT's stability, catalyst surface reactivity, and charge distributions.

An intrinsic particle – SWCNT relation was found based on the potential energy stored by the nanotube structure. The strain energy, proportional to the curvature of the nanotube, is increased when the nanotube cap seed expands on top of the catalyst particle surface. Therefore, a probabilistic model was offered to describe the relationship between catalyst size and SWCNT diameter. This model based on the dislocation theory of CNT growth assumes a complete active spherical catalyst particle. The probability function $f_d(d_T)$ parameters were calibrated using experimental data from HRTEM. The Young moduli obtained from the optimized parameter (α_{opt}) for SWCNTs and MWCNTs are in good agreement with experimental values.

Interfacial carbon-metal interactions are essential measurements that help classify a graphene-particle system's ability to nucleate or remain inactive. The stability of SWCNT nucleation is related to the combined interaction strength with the catalyst particle and substrate. Chapter I found that the critical diameter (d_c) in the nucleation vs encapsulation stability correlates with the tangential to perpendicular growth regime

transition. This type of grow transition is observed as well from the slope change around (d_p/d_c) for the most probable diameter $< d_T >$ obtained with the model. In Chapter IV, an increasing concentration of surface oxygen resulted in a decreased carbon-metal interaction. A reduction in the interfacial strength affects the nucleation vs. encapsulation rate. This result helped explain some experimental observations, where the use of oxygen-rich compounds (O_2, CO_x, H_2O, $C_xH_yO_z$) was selectively promoting a short range of SWCNT chiralities. Finally, the energy profile of a pre-nucleated cap spreading on top of a partially oxidated iron surface showed a preference for closed pentagons in the SWCNT's rim compared with the reduced Fe surface.

The effect of variable bulk and surface composition on surface cobalt atoms' reactivity during SWCNT nucleation was also studied. It is widely known that nanoparticles' shape, composition, and surface structure evolve during SWCNT nucleation. The carbon solubility, etching agents, diffusion, and reaction energy barriers play a role in the formation, nucleation, and subsequent growth. Chapter V comparative analysis of two meta-stable cobalt carbide phases (Co_2C and Co_3C) with its corresponding rich-Co (Co-top) and diluted carbon (CoC-top) terminations found that the dissociation reactions of C_2H_2 and CO had mostly surface-dominant contributions. The larger bulk composition contribution was observed during the first H-C dissociation reaction. Here, Co_2C surfaces presented the lower energy barriers. Lastly, we further corroborated that those drastic changes in the interaction strength between the SWCNT rim and different surface terminations of the same catalyst particle may promote nucleation.

The results presented in this work showed significant progress towards a better understanding of the nanotube-particle-substrate system and the controlled SWCNT growth. Some areas that may require further study and additional future directions are enumerated next:

1. A great deal of study needs to be done to understand the effects of physical and chemical interactions between the substrate, the catalyst material, and the SWCNT. The substrate's hidden effect during nucleation and growth for producing different types of SWCNTs could be explored. Metal-substrates interactions can help clarify some experimental observations in the type of growth (base vs. tip growth). The preference of growth from the substrate (i.e., "root growth") for certain catalyst-substrates combinations suggests a dominant interaction that controls the vertical growth[227]. DFT simulations can correlate changes in the CNT-metal strength of interaction while varying the substrate.
2. It has been suspected for a long time that many catalyst-substrate interactions affect the growth mechanism of the SWCNTs. One example is the possibility to induce charge transfer from the substrate to species adsorbed on the supported particle. Low-coordinated cations or anions,[283] isolated cation[284]/anion vacancies,[285,286] hydroxyl groups,[287] peroxo groups,[288] and grain boundaries[289], can potentially alter the substrate reactivity. Studying the impact of substrate doping on the dissociation reaction is a subject of great interest.
3. In chapter IV, we reported the role of surface oxygen in the nucleation process. Similarly, the study of surface's saturation with some specific functional groups,

such as hydroxy (OH), may elucidate the effect behind the so-called "supergrowth" generated by water-assisted CVD.[68,290]

4. The limit of oxidation to enhance nucleation is yet to be discovered. We saw in Chapter IV the added benefits of having small oxidated areas on the particle surface. However, too much oxidation could inactivate the particle as well. Further studies are necessary to find the equilibrium between nucleation promoter and inhibitor for the oxide surfaces.
5. Using reactive potentials, such as ReaxFF, allows for substrate-catalyst particle dynamics and interactions at typical CVD reaction temperatures. Implementation of algorithms that can potentially reach time scales used in experiments is crucial. Accelerated molecular dynamics and hybrid approaches such as MD + time-stamp force-biased Monte Carlo simulations can be used towards this goal.
6. MD simulations with particles' diameters above 2 nm may elucidate kinetic paths and relations not yet explored for the tangential vs. perpendicular growth mode. Additionally, above 2-3 nm, MWCNTs become more stable, and the mechanism for their nucleation can be studied.
7. Metal oxide substrates such as Alumina allow for diffusion of melting catalyst layers at high temperatures. The diffusion of metal atoms from reservoir conductive underlayers (Fe, Cu) through barrier layers (Al_2O_3, SiO_2) may enhance or inactivate the precursor decomposition. Molecular dynamics (MD) and DFT simulations can help study the effects of a coupled multi-layer system (particle + support + reservoir) and obtain the composition profile from the underlayer to the substrate's surface. The

formation of alloys or intermediate species may bring some light to the different SWCNT lengths observed experimentally.

REFERENCES

(1) He, M.; Zhang, S.; Zhang, J. Horizontal Single-Walled Carbon Nanotube Arrays: Controlled Synthesis, Characterizations, and Applications. *Chem. Rev.* **2020**, *120* (22), 12592–12684. https://doi.org/10.1021/acs.chemrev.0c00395.

(2) Iijima, S. Helical Microtubules of Graphitic Carbon. *Nature* **1991**, *354* (6348), 56–58. https://doi.org/10.1038/354056a0.

(3) Iijima, S.; Ichihashi, T. Single-Shell Carbon Nanotubes of 1-Nm Diameter. *Nature* **1993**, *363* (6430), 603–605. https://doi.org/10.1038/363603a0.

(4) Bethune, D. S.; Kiang, C. H.; de Vries, M. S.; Gorman, G.; Savoy, R.; Vazquez, J.; Beyers, R. Cobalt-Catalysed Growth of Carbon Nanotubes with Single-Atomic-Layer Walls. *Nature* **1993**, *363* (6430), 605–607. https://doi.org/10.1038/363605a0.

(5) Baughman, R. H. Carbon Nanotubes--the Route Toward Applications. *Science* **2002**, *297* (5582), 787–792. https://doi.org/10.1126/science.1060928.

(6) De Volder, M. F. L.; Tawfick, S. H.; Baughman, R. H.; Hart, A. J. Carbon Nanotubes: Present and Future Commercial Applications. *Science* **2013**, *339* (6119), 535–539. https://doi.org/10.1126/science.1222453.

(7) Li, Y. The Quarter-Century Anniversary of Carbon Nanotube Research. *ACS Nano* **2017**, *11* (1), 1–2. https://doi.org/10.1021/acsnano.7b00232.

(8) Castro Neto, A. H.; Guinea, F.; Peres, N. M. R.; Novoselov, K. S.; Geim, A. K. The Electronic Properties of Graphene. *Rev. Mod. Phys.* **2009**, *81* (1), 109–162. https://doi.org/10.1103/RevModPhys.81.109.

(9) Yakobson, B. I.; Brabec, C. J.; Bernholc, J. Nanomechanics of Carbon Tubes: Instabilities beyond Linear Response. *Phys. Rev. Lett.* **1996**, *76* (14), 2511–2514. https://doi.org/10.1103/PhysRevLett.76.2511.

(10) Dürkop, T.; Getty, S. A.; Cobas, E.; Fuhrer, M. S. Extraordinary Mobility in Semiconducting Carbon Nanotubes. *Nano Lett.* **2004**, *4* (1), 35–39. https://doi.org/10.1021/nl034841q.

(11) Wang, F. The Optical Resonances in Carbon Nanotubes Arise from Excitons. *Science* **2005**, *308* (5723), 838–841. https://doi.org/10.1126/science.1110265.

(12) Franklin, A. D. Nanomaterials in Transistors: From High-Performance to Thin-Film Applications. *Science* **2015**, *349* (6249), aab2750–aab2750. https://doi.org/10.1126/science.aab2750.

(13) Wu, Z. Transparent, Conductive Carbon Nanotube Films. *Science* **2004**, *305* (5688), 1273–1276. https://doi.org/10.1126/science.1101243.

(14) Avouris, P.; Chen, Z.; Perebeinos, V. Carbon-Based Electronics. *Nature Nanotech* **2007**, *2* (10), 605–615. https://doi.org/10.1038/nnano.2007.300.

(15) Sun, D.-M.; Liu, C.; Ren, W.-C.; Cheng, H.-M. A Review of Carbon Nanotube- and Graphene-Based Flexible Thin-Film Transistors. *Small* **2013**, *9* (8), 1188–1205. https://doi.org/10.1002/smll.201203154.

(16) Akinwande, D.; Petrone, N.; Hone, J. Two-Dimensional Flexible Nanoelectronics. *Nature Communications* **2014**, *5* (1). https://doi.org/10.1038/ncomms6678.

(17) Nasir, S.; Hussein, M.; Zainal, Z.; Yusof, N. Carbon-Based Nanomaterials/Allotropes: A Glimpse of Their Synthesis, Properties and Some Applications. *Materials* **2018**, *11* (2), 295. https://doi.org/10.3390/ma11020295.

(18) Peng, L.-M.; Zhang, Z.; Qiu, C. Carbon Nanotube Digital Electronics. *Nat Electron* **2019**, *2* (11), 499–505. https://doi.org/10.1038/s41928-019-0330-2.

(19) Van Dal, M.; Duriez, B.; Vellianitis, G.; Doornbos, G.; Oxland, R.; Holland, M.; Afzalian, A.; See, Y.; Passlack, M.; Diaz, C. *2014 IEEE International Electron Devices Meeting*; IEEE, 2014.

(20) Shulaker, M. M.; Hills, G.; Patil, N.; Wei, H.; Chen, H.-Y.; Wong, H.-S. P.; Mitra, S. Carbon Nanotube Computer. *Nature* **2013**, *501* (7468), 526–530. https://doi.org/10.1038/nature12502.

(21) Hills, G.; Lau, C.; Wright, A.; Fuller, S.; Bishop, M. D.; Srimani, T.; Kanhaiya, P.; Ho, R.; Amer, A.; Stein, Y.; Murphy, D.; Arvind; Chandrakasan, A.; Shulaker, M. M. Modern Microprocessor Built from Complementary Carbon Nanotube Transistors. *Nature* **2019**, *572* (7771), 595–602. https://doi.org/10.1038/s41586-019-1493-8.

(22) Van Noorden, R. Chemistry: The Trials of New Carbon. *Nature* **2011**, *469* (7328), 14–16. https://doi.org/10.1038/469014a.

(23) Dresslhaus, M. S.; Dresslhaus, G.; Eklund, P. C. Science of Fullerenes and Carbon Nanotubes. *San Diego, CA: Academic* **1996**.

(24) Thess, A.; Lee, R.; Nikolaev, P.; Dai, H.; Petit, P.; Robert, J.; Xu, C.; Lee, Y. H.; Kim, S. G.; Rinzler, A. G.; Colbert, D. T.; Scuseria, G. E.; Tomanek, D.; Fischer, J. E.; Smalley, R. E. Crystalline Ropes of Metallic Carbon Nanotubes. *Science* **1996**, *273* (5274), 483–487. https://doi.org/10.1126/science.273.5274.483.

(25) Bronikowski, M. J.; Willis, P. A.; Colbert, D. T.; Smith, K. A.; Smalley, R. E. Gas-Phase Production of Carbon Single-Walled Nanotubes from Carbon Monoxide via the HiPco Process: A Parametric Study. *Journal of Vacuum Science & Technology A: Vacuum, Surfaces, and Films* **2001**, *19* (4), 1800–1805. https://doi.org/10.1116/1.1380721.

(26) Bajwa, N.; Li, X.; Ajayan, P. M.; Vajtai, R. Mechanisms for Catalytic CVD Growth of Multiwalled Carbon Nanotubes. *Journal of Nanoscience and Nanotechnology* **2008**, *8* (11), 6054–6064. https://doi.org/10.1166/jnn.2008.SW02.

(27) MacKenzie, K. J.; Dunens, O. M.; Harris, A. T. An Updated Review of Synthesis Parameters and Growth Mechanisms for Carbon Nanotubes in Fluidized Beds. *Industrial & Engineering Chemistry Research* **2010**, *49* (11), 5323–5338. https://doi.org/10.1021/ie9019787.

(28) Serp, P.; Figueiredo, J. L. *Carbon Materials for Catalysis*; John Wiley & Sons, 2009.

(29) Tessonnier, J.-P.; Su, D. S. Recent Progress on the Growth Mechanism of Carbon Nanotubes: A Review. *ChemSusChem* **2011**, *4* (7), 824–847. https://doi.org/10.1002/cssc.201100175.

(30) He, M.; Zhang, S.; Zhang, J. Horizontal Single-Walled Carbon Nanotube Arrays: Controlled Synthesis, Characterizations, and Applications. *Chem. Rev.* **2020**, *120* (22), 12592–12684. https://doi.org/10.1021/acs.chemrev.0c00395.

(31) He, M.; Zhang, S.; Wu, Q.; Xue, H.; Xin, B.; Wang, D.; Zhang, J. Designing Catalysts for Chirality-Selective Synthesis of Single-Walled Carbon Nanotubes:

Past Success and Future Opportunity. *Adv. Mater.* **2019**, *31* (9), 1800805. https://doi.org/10.1002/adma.201800805.

(32) Kitiyanan, B.; Alvarez, W. E.; Harwell, J. H.; Resasco, D. E. Controlled Production of Single-Wall Carbon Nanotubes by Catalytic Decomposition of CO on Bimetallic Co–Mo Catalysts. *Chemical Physics Letters* **2000**, *317* (3–5), 497–503. https://doi.org/10.1016/S0009-2614(99)01379-2.

(33) Moisala, A.; Nasibulin, A. G.; Kauppinen, E. I. The Role of Metal Nanoparticles in the Catalytic Production of Single-Walled Carbon Nanotubes—a Review. *Journal of Physics: Condensed Matter* **2003**, *15* (42), S3011–S3035. https://doi.org/10.1088/0953-8984/15/42/003.

(34) Wang, X.; Ding, F. How a Solid Catalyst Determines the Chirality of the Single-Wall Carbon Nanotube Grown on It. *J. Phys. Chem. Lett.* **2019**, *10* (4), 735–741. https://doi.org/10.1021/acs.jpclett.9b00207.

(35) Mattevi, C.; Kim, H.; Chhowalla, M. A Review of Chemical Vapour Deposition of Graphene on Copper. *J. Mater. Chem.* **2011**, *21* (10), 3324–3334. https://doi.org/10.1039/C0JM02126A.

(36) Xu, Z.; Qiu, L.; Ding, F. The Kinetics of Chirality Assignment in Catalytic Single-Walled Carbon Nanotube Growth and the Routes towards Selective Growth. *Chem. Sci.* **2018**, *9* (11), 3056–3061. https://doi.org/10.1039/C7SC04714B.

(37) Li, M.; Liu, X.; Zhao, X.; Yang, F.; Wang, X.; Li, Y. Metallic Catalysts for Structure-Controlled Growth of Single-Walled Carbon Nanotubes. *Topics in Current Chemistry* **2017**, *375* (2). https://doi.org/10.1007/s41061-017-0116-9.

(38) Lanzani, G.; Nasibulin, A. G.; Laasonen, K.; Kauppinen, E. I. CO Dissociation and CO+O Reactions on a Nanosized Iron Cluster. *Nano Res.* **2009**, *2* (8), 660–670. https://doi.org/10.1007/s12274-009-9069-9.

(39) Diaz, M. C.; Jiang, H.; Kauppinen, E.; Sharma, R.; Balbuena, P. B. Can Single-Walled Carbon Nanotube Diameter Be Defined by Catalyst Particle Diameter? *J. Phys. Chem. C* **2019**, *123* (50), 30305–30317. https://doi.org/10.1021/acs.jpcc.9b07724.

(40) Yang, F.; Wang, X.; Li, M.; Liu, X.; Zhao, X.; Zhang, D.; Zhang, Y.; Yang, J.; Li, Y. Templated Synthesis of Single-Walled Carbon Nanotubes with Specific Structure. *Acc. Chem. Res.* **2016**, *49* (4), 606–615. https://doi.org/10.1021/acs.accounts.5b00485.

(41) Zhang, S.; Kang, L.; Wang, X.; Tong, L.; Yang, L.; Wang, Z.; Qi, K.; Deng, S.; Li, Q.; Bai, X.; Ding, F.; Zhang, J. Arrays of Horizontal Carbon Nanotubes of Controlled Chirality Grown Using Designed Catalysts. *Nature* **2017**, *543* (7644), 234–238. https://doi.org/10.1038/nature21051.

(42) Zhao, Q.; Xu, Z.; Hu, Y.; Ding, F.; Zhang, J. Chemical Vapor Deposition Synthesis of Near-Zigzag Single-Walled Carbon Nanotubes with Stable Tube-Catalyst Interface. *Sci. Adv.* **2016**, *2* (5), e1501729. https://doi.org/10.1126/sciadv.1501729.

(43) Gómez-Gualdrón, D. A.; Zhao, J.; Balbuena, P. B. Nanocatalyst Structure as a Template to Define Chirality of Nascent Single-Walled Carbon Nanotubes. *The Journal of Chemical Physics* **2011**, *134* (1), 014705. https://doi.org/10.1063/1.3509387.

(44) He, M.; Jiang, H.; Liu, B.; Fedotov, P. V.; Chernov, A. I.; Obraztsova, E. D.; Cavalca, F.; Wagner, J. B.; Hansen, T. W.; Anoshkin, I. V.; Obraztsova, E. A.; Belkin, A. V.; Sairanen, E.; Nasibulin, A. G.; Lehtonen, J.; Kauppinen, E. I. Chiral-Selective Growth of Single-Walled Carbon Nanotubes on Lattice-Mismatched Epitaxial Cobalt Nanoparticles. *Sci Rep* **2013**, *3* (1), 1460. https://doi.org/10.1038/srep01460.

(45) He, M.; Fedotov, P. V.; Chernov, A.; Obraztsova, E. D.; Jiang, H.; Wei, N.; Cui, H.; Sainio, J.; Zhang, W.; Jin, H.; Karppinen, M.; Kauppinen, E. I.; Loiseau, A. Chiral-Selective Growth of Single-Walled Carbon Nanotubes on Fe-Based Catalysts Using CO as Carbon Source. *Carbon* **2016**, *108*, 521–528. https://doi.org/10.1016/j.carbon.2016.07.048.

(46) He, M.; Wang, X.; Zhang, L.; Wu, Q.; Song, X.; Chernov, A. I.; Fedotov, P. V.; Obraztsova, E. D.; Sainio, J.; Jiang, H.; Cui, H.; Ding, F.; Kauppinen, E. Anchoring Effect of Ni2+ in Stabilizing Reduced Metallic Particles for Growing Single-Walled Carbon Nanotubes. *Carbon* **2018**, *128*, 249–256. https://doi.org/10.1016/j.carbon.2017.11.093.

(47) Harutyunyan, A. R.; Chen, G.; Paronyan, T. M.; Pigos, E. M.; Kuznetsov, O. A.; Hewaparakrama, K.; Kim, S. M.; Zakharov, D.; Stach, E. A.; Sumanasekera, G. U. Preferential Growth of Single-Walled Carbon Nanotubes with Metallic Conductivity. *Science* **2009**, *326* (5949), 116–120. https://doi.org/10.1126/science.1177599.

(48) Hata, K. Water-Assisted Highly Efficient Synthesis of Impurity-Free Single-Walled Carbon Nanotubes. *Science* **2004**, *306* (5700), 1362–1364. https://doi.org/10.1126/science.1104962.

(49) Magrez, A.; Seo, J. W.; Smajda, R.; Korbely, B.; Andresen, J. C.; Mionić, M.; Casimirius, S.; Forró, L. Low-Temperature, Highly Efficient Growth of Carbon Nanotubes on Functional Materials by an Oxidative Dehydrogenation Reaction. *ACS Nano* **2010**, *4* (7), 3702–3708. https://doi.org/10.1021/nn100279j.

(50) Shi, W.; Li, J.; Polsen, E. S.; Oliver, C. R.; Zhao, Y.; Meshot, E. R.; Barclay, M.; Fairbrother, D. H.; Hart, A. J.; Plata, D. L. Oxygen-Promoted Catalyst Sintering Influences Number Density, Alignment, and Wall Number of Vertically Aligned Carbon Nanotubes. *Nanoscale* **2017**, *9* (16), 5222–5233. https://doi.org/10.1039/C6NR09802A.

(51) Dai, H.; Rinzler, A. G.; Nikolaev, P.; Thess, A.; Colbert, D. T.; Smalley, R. E. Single-Wall Nanotubes Produced by Metal-Catalyzed Disproportionation of Carbon Monoxide. *Chemical Physics Letters* **1996**, *260* (3–4), 471–475. https://doi.org/10.1016/0009-2614(96)00862-7.

(52) Wu, K.; Niu, Y.; Zhang, Y.; Yong, Z.; Li, Q. Continuous Growth of Carbon Nanotube Films: From Controllable Synthesis to Real Applications. *Composites Part A: Applied Science and Manufacturing* **2021**, *144*, 106359. https://doi.org/10.1016/j.compositesa.2021.106359.

(53) Nasibulin, A. G.; Pikhitsa, P. V.; Jiang, H.; Kauppinen, E. I. Correlation between Catalyst Particle and Single-Walled Carbon Nanotube Diameters. *Carbon* **2005**, *43* (11), 2251–2257. https://doi.org/10.1016/j.carbon.2005.03.048.

(54) Liao, Y.; Jiang, H.; Wei, N.; Laiho, P.; Zhang, Q.; Khan, S. A.; Kauppinen, E. I. Direct Synthesis of Colorful Single-Walled Carbon Nanotube Thin Films. *J. Am. Chem. Soc.* **2018**, *140* (31), 9797–9800. https://doi.org/10.1021/jacs.8b05151.

(55) Eres, G.; Kinkhabwala, A. A.; Cui, H.; Geohegan, D. B.; Puretzky, A. A.; Lowndes, D. H. Molecular Beam-Controlled Nucleation and Growth of Vertically Aligned Single-Wall Carbon Nanotube Arrays. *J. Phys. Chem. B* **2005**, *109* (35), 16684–16694. https://doi.org/10.1021/jp051531i.

(56) Eres, G.; Rouleau, C. M.; Yoon, M.; Puretzky, A. A.; Jackson, J. J.; Geohegan, D. B. Model for Self-Assembly of Carbon Nanotubes from Acetylene Based on Real-Time Studies of Vertically Aligned Growth Kinetics. *J. Phys. Chem. C* **2009**, *113* (35), 15484–15491. https://doi.org/10.1021/jp9001127.

(57) Sugime, H.; Noda, S. Cold-Gas Chemical Vapor Deposition to Identify the Key Precursor for Rapidly Growing Vertically-Aligned Single-Wall and Few-Wall Carbon Nanotubes from Pyrolyzed Ethanol. *Carbon* **2012**, *50* (8), 2953–2960. https://doi.org/10.1016/j.carbon.2012.02.065.

(58) Zhong, G.; Hofmann, S.; Yan, F.; Telg, H.; Warner, J. H.; Eder, D.; Thomsen, C.; Milne, W. I.; Robertson, J. Acetylene: A Key Growth Precursor for Single-Walled Carbon Nanotube Forests. *J. Phys. Chem. C* **2009**, *113* (40), 17321–17325. https://doi.org/10.1021/jp905134b.

(59) Meshot, E. R.; Plata, D. L.; Tawfick, S.; Zhang, Y.; Verploegen, E. A.; Hart, A. J. Engineering Vertically Aligned Carbon Nanotube Growth by Decoupled Thermal Treatment of Precursor and Catalyst. *ACS Nano* **2009**, *3* (9), 2477–2486. https://doi.org/10.1021/nn900446a.

(60) Plata, D. L.; Meshot, E. R.; Reddy, C. M.; Hart, A. J.; Gschwend, P. M. Multiple Alkynes React with Ethylene To Enhance Carbon Nanotube Synthesis, Suggesting a Polymerization-like Formation Mechanism. *ACS Nano* **2010**, *4* (12), 7185–7192. https://doi.org/10.1021/nn101842g.

(61) Pint, C. L.; Sun, Z.; Moghazy, S.; Xu, Y.-Q.; Tour, J. M.; Hauge, R. H. Supergrowth of Nitrogen-Doped Single-Walled Carbon Nanotube Arrays: Active Species, Dopant Characterization, and Doped/Undoped Heterojunctions. *ACS Nano* **2011**, *5* (9), 6925–6934. https://doi.org/10.1021/nn201252z.

(62) Rao, R.; Pint, C. L.; Islam, A. E.; Weatherup, R. S.; Hofmann, S.; Meshot, E. R.; Wu, F.; Zhou, C.; Dee, N.; Amama, P. B.; Carpena-Nuñez, J.; Shi, W.; Plata, D. L.; Penev, E. S.; Yakobson, B. I.; Balbuena, P. B.; Bichara, C.; Futaba, D. N.; Noda, S.; Shin, H.; Kim, K. S.; Simard, B.; Mirri, F.; Pasquali, M.; Fornasiero, F.; Kauppinen, E. I.; Arnold, M.; Cola, B. A.; Nikolaev, P.; Arepalli, S.; Cheng,

H.-M.; Zakharov, D. N.; Stach, E. A.; Zhang, J.; Wei, F.; Terrones, M.; Geohegan, D. B.; Maruyama, B.; Maruyama, S.; Li, Y.; Adams, W. W.; Hart, A. J. Carbon Nanotubes and Related Nanomaterials: Critical Advances and Challenges for Synthesis toward Mainstream Commercial Applications. *ACS Nano* **2018**, *12* (12), 11756–11784. https://doi.org/10.1021/acsnano.8b06511.

(63) Gilbertson, L. M.; Zimmerman, J. B.; Plata, D. L.; Hutchison, J. E.; Anastas, P. T. Designing Nanomaterials to Maximize Performance and Minimize Undesirable Implications Guided by the Principles of Green Chemistry. *Chem. Soc. Rev.* **2015**, *44* (16), 5758–5777. https://doi.org/10.1039/C4CS00445K.

(64) Kolpak, A. M.; Grossman, J. C. Azobenzene-Functionalized Carbon Nanotubes As High-Energy Density Solar Thermal Fuels. *Nano Lett.* **2011**, *11* (8), 3156–3162. https://doi.org/10.1021/nl201357n.

(65) Kumar, R.; Singh, R. K.; Singh, D. P. Natural and Waste Hydrocarbon Precursors for the Synthesis of Carbon Based Nanomaterials: Graphene and CNTs. *Renewable and Sustainable Energy Reviews* **2016**, *58*, 976–1006. https://doi.org/10.1016/j.rser.2015.12.120.

(66) Shah, K. A.; Tali, B. A. Synthesis of Carbon Nanotubes by Catalytic Chemical Vapour Deposition: A Review on Carbon Sources, Catalysts and Substrates. *Materials Science in Semiconductor Processing* **2016**, *41*, 67–82. https://doi.org/10.1016/j.mssp.2015.08.013.

(67) Kumar, M.; Kakamu, K.; Okazaki, T.; Ando, Y. Field Emission from Camphor–Pyrolyzed Carbon Nanotubes. *Chemical Physics Letters* **2004**, *385* (3–4), 161–165. https://doi.org/10.1016/j.cplett.2003.12.064.

(68) Hata, K. Water-Assisted Highly Efficient Synthesis of Impurity-Free Single-Walled Carbon Nanotubes. *Science* **2004**, *306* (5700), 1362–1364. https://doi.org/10.1126/science.1104962.

(69) Ding, D.; Wang, J.; Cao, Z.; Dai, J. Synthesis of Carbon Nanostructures on Nanocrystalline Ni–Ni3P Catalyst Supported by SiC Whiskers. *Carbon* **2003**, *41* (3), 579–582. https://doi.org/10.1016/S0008-6223(02)00339-1.

(70) Murakami, T.; Sako, T.; Harima, H.; Kisoda, K.; Mitikami, K.; Isshiki, T. Raman Study of SWNTs Grown by CCVD Method on SiC. *Thin Solid Films* **2004**, *464–465*, 319–322. https://doi.org/10.1016/j.tsf.2004.06.037.

(71) Baker, R. Nucleation and Growth of Carbon Deposits from the Nickel Catalyzed Decomposition of Acetylene. *Journal of Catalysis* **1972**, *26* (1), 51–62. https://doi.org/10.1016/0021-9517(72)90032-2.

(72) Baker, R. Formation of Filamentous Carbon from Iron, Cobalt and Chromium Catalyzed Decomposition of Acetylene. *Journal of Catalysis* **1973**, *30* (1), 86–95. https://doi.org/10.1016/0021-9517(73)90055-9.

(73) Kumar, M.; Ando, Y. A Simple Method of Producing Aligned Carbon Nanotubes from an Unconventional Precursor – Camphor. *Chemical Physics Letters* **2003**, *374* (5–6), 521–526. https://doi.org/10.1016/S0009-2614(03)00742-5.

(74) Cheung, C. L.; Kurtz, A.; Park, H.; Lieber, C. M. Diameter-Controlled Synthesis of Carbon Nanotubes. *The Journal of Physical Chemistry B* **2002**, *106* (10), 2429–2433. https://doi.org/10.1021/jp0142278.

(75) Mattevi, C.; Wirth, C. T.; Hofmann, S.; Blume, R.; Cantoro, M.; Ducati, C.; Cepek, C.; Knop-Gericke, A.; Milne, S.; Castellarin-Cudia, C.; Dolafi, S.; Goldoni, A.; Schloegl, R.; Robertson, J. In-Situ X-Ray Photoelectron Spectroscopy Study of Catalyst−Support Interactions and Growth of Carbon Nanotube Forests. *J. Phys. Chem. C* **2008**, *112* (32), 12207–12213. https://doi.org/10.1021/jp802474g.

(76) Colomer, J.-F.; Stephan, C.; Lefrant, S.; Van Tendeloo, G.; Willems, I.; Kónya, Z.; Fonseca, A.; Laurent, C.; Nagy, J. B. Large-Scale Synthesis of Single-Wall Carbon Nanotubes by Catalytic Chemical Vapor Deposition (CCVD) Method. *Chemical Physics Letters* **2000**, *317* (1–2), 83–89. https://doi.org/10.1016/S0009-2614(99)01338-X.

(77) Hongo, H.; Yudasaka, M.; Ichihashi, T.; Nihey, F.; Iijima, S. Chemical Vapor Deposition of Single-Wall Carbon Nanotubes on Iron-Film-Coated Sapphire Substrates. *Chemical Physics Letters* **2002**, *361* (3–4), 349–354. https://doi.org/10.1016/S0009-2614(02)00963-6.

(78) Ward, J. W.; Wei, B. Q.; Ajayan, P. M. Substrate Effects on the Growth of Carbon Nanotubes by Thermal Decomposition of Methane. *Chemical Physics Letters* **2003**, *376* (5–6), 717–725. https://doi.org/10.1016/S0009-2614(03)01067-4.

(79) Ago, H.; Nakamura, K.; Imamura, S.; Tsuji, M. Growth of Double-Wall Carbon Nanotubes with Diameter-Controlled Iron Oxide Nanoparticles Supported on MgO. *Chemical Physics Letters* **2004**, *391* (4–6), 308–313. https://doi.org/10.1016/j.cplett.2004.04.110.

(80) Couteau, E.; Hernadi, K.; Seo, J. W.; Thiên-Nga, L.; Mikó, Cs.; Gaál, R.; Forró, L. CVD Synthesis of High-Purity Multiwalled Carbon Nanotubes Using CaCO3 Catalyst Support for Large-Scale Production. *Chemical Physics Letters* **2003**, *378* (1–2), 9–17. https://doi.org/10.1016/S0009-2614(03)01218-1.

(81) Willems, I.; Kónya, Z.; Colomer, J.-F.; Van Tendeloo, G.; Nagaraju, N.; Fonseca, A.; Nagy, J. B. Control of the Outer Diameter of Thin Carbon Nanotubes Synthesized by Catalytic Decomposition of Hydrocarbons. *Chemical Physics Letters* **2000**, *317* (1–2), 71–76. https://doi.org/10.1016/S0009-2614(99)01300-7.

(82) Szabó, A.; Méhn, D.; Kónya, Z.; Fonseca, A.; Nagy, J. B. "Wash and Go": Sodium Chloride as an Easily Removable Catalyst Support for the Synthesis of Carbon Nanotubes. *PhysChemComm* **2003**, *6* (10), 40–41. https://doi.org/10.1039/B305670H.

(83) Shao, X.; Prada, S.; Giordano, L.; Pacchioni, G.; Nilius, N.; Freund, H.-J. Tailoring the Shape of Metal Ad-Particles by Doping the Oxide Support. *Angew. Chem. Int. Ed.* **2011**, *50* (48), 11525–11527. https://doi.org/10.1002/anie.201105355.

(84) Rahmani Didar, B.; Balbuena, P. B. Reactivity of Cu and Co Nanoparticles Supported on Mo-Doped MgO. *Ind. Eng. Chem. Res.* **2019**, *58* (39), 18213–18222. https://doi.org/10.1021/acs.iecr.9b03517.

(85) Rao, R.; Pint, C. L.; Islam, A. E.; Weatherup, R. S.; Hofmann, S.; Meshot, E. R.; Wu, F.; Zhou, C.; Dee, N.; Amama, P. B.; Carpena-Nuñez, J.; Shi, W.; Plata, D. L.; Penev, E. S.; Yakobson, B. I.; Balbuena, P. B.; Bichara, C.; Futaba, D. N.; Noda, S.; Shin, H.; Kim, K. S.; Simard, B.; Mirri, F.; Pasquali, M.; Fornasiero, F.; Kauppinen, E. I.; Arnold, M.; Cola, B. A.; Nikolaev, P.; Arepalli, S.; Cheng, H.-M.; Zakharov, D. N.; Stach, E. A.; Zhang, J.; Wei, F.; Terrones, M.; Geohegan, D. B.; Maruyama, B.; Maruyama, S.; Li, Y.; Adams, W. W.; Hart, A. J. Carbon Nanotubes and Related Nanomaterials: Critical Advances and Challenges for Synthesis toward Mainstream Commercial Applications. *ACS Nano* **2018**, *12* (12), 11756–11784. https://doi.org/10.1021/acsnano.8b06511.

(86) Smalley, R. E.; Li, Y.; Moore, V. C.; Price, B. K.; Colorado, R.; Schmidt, H. K.; Hauge, R. H.; Barron, A. R.; Tour, J. M. Single Wall Carbon Nanotube Amplification: En Route to a Type-Specific Growth Mechanism. *J. Am. Chem. Soc.* **2006**, *128* (49), 15824–15829. https://doi.org/10.1021/ja065767r.

(87) Yao, Y.; Feng, C.; Zhang, J.; Liu, Z. "Cloning" of Single-Walled Carbon Nanotubes via Open-End Growth Mechanism. *Nano Lett.* **2009**, *9* (4), 1673–1677. https://doi.org/10.1021/nl900207v.

(88) Liu, J.; Wang, C.; Tu, X.; Liu, B.; Chen, L.; Zheng, M.; Zhou, C. Chirality-Controlled Synthesis of Single-Wall Carbon Nanotubes Using Vapour-Phase Epitaxy. *Nat Commun* **2012**, *3* (1), 1199. https://doi.org/10.1038/ncomms2205.

(89) Tu, X.; Manohar, S.; Jagota, A.; Zheng, M. DNA Sequence Motifs for Structure-Specific Recognition and Separation of Carbon Nanotubes. *Nature* **2009**, *460* (7252), 250–253. https://doi.org/10.1038/nature08116.

(90) Tu, X.; Hight Walker, A. R.; Khripin, C. Y.; Zheng, M. Evolution of DNA Sequences Toward Recognition of Metallic Armchair Carbon Nanotubes. *J. Am. Chem. Soc.* **2011**, *133* (33), 12998–13001. https://doi.org/10.1021/ja205407q.

(91) De Volder, M. F. L.; Vidaud, D. O.; Meshot, E. R.; Tawfick, S.; John Hart, A. Self-Similar Organization of Arrays of Individual Carbon Nanotubes and Carbon Nanotube Micropillars. *Microelectronic Engineering* **2010**, *87* (5–8), 1233–1238. https://doi.org/10.1016/j.mee.2009.11.139.

(92) Zhang, L.; Li, Z.; Tan, Y.; Lolli, G.; Sakulchaicharoen, N.; Requejo, F. G.; Mun, B. S.; Resasco, D. E. Influence of a Top Crust of Entangled Nanotubes on the Structure of Vertically Aligned Forests of Single-Walled Carbon Nanotubes. *Chem. Mater.* **2006**, *18* (23), 5624–5629. https://doi.org/10.1021/cm061783b.

(93) Javey, A.; Guo, J.; Wang, Q.; Lundstrom, M.; Dai, H. Ballistic Carbon Nanotube Field-Effect Transistors. *Nature* **2003**, *424* (6949), 654–657. https://doi.org/10.1038/nature01797.

(94) Kang, S. J.; Kocabas, C.; Ozel, T.; Shim, M.; Pimparkar, N.; Alam, M. A.; Rotkin, S. V.; Rogers, J. A. High-Performance Electronics Using Dense, Perfectly Aligned Arrays of Single-Walled Carbon Nanotubes. *Nature Nanotech* **2007**, *2* (4), 230–236. https://doi.org/10.1038/nnano.2007.77.

(95) Cao, Q.; Han, S.; Tulevski, G. S.; Zhu, Y.; Lu, D. D.; Haensch, W. Arrays of Single-Walled Carbon Nanotubes with Full Surface Coverage for High-Performance Electronics. *Nature Nanotech* **2013**, *8* (3), 180–186. https://doi.org/10.1038/nnano.2012.257.

(96) Shulaker, M. M.; Hills, G.; Patil, N.; Wei, H.; Chen, H.-Y.; Wong, H.-S. P.; Mitra, S. Carbon Nanotube Computer. *Nature* **2013**, *501* (7468), 526–530. https://doi.org/10.1038/nature12502.

(97) Cao, Q.; Tersoff, J.; Farmer, D. B.; Zhu, Y.; Han, S.-J. Carbon Nanotube Transistors Scaled to a 40-Nanometer Footprint. *Science* **2017**, *356* (6345), 1369–1372. https://doi.org/10.1126/science.aan2476.

(98) Brady, G. J.; Way, A. J.; Safron, N. S.; Evensen, H. T.; Gopalan, P.; Arnold, M. S. Quasi-Ballistic Carbon Nanotube Array Transistors with Current Density Exceeding Si and GaAs. *Sci. Adv.* **2016**, *2* (9), e1601240. https://doi.org/10.1126/sciadv.1601240.

(99) Lefebvre, J.; Ding, J.; Li, Z.; Finnie, P.; Lopinski, G.; Malenfant, P. R. L. High-Purity Semiconducting Single-Walled Carbon Nanotubes: A Key Enabling Material in Emerging Electronics. *Acc. Chem. Res.* **2017**, *50* (10), 2479–2486. https://doi.org/10.1021/acs.accounts.7b00234.

(100) Kocabas, C.; Kim, H. -s.; Banks, T.; Rogers, J. A.; Pesetski, A. A.; Baumgardner, J. E.; Krishnaswamy, S. V.; Zhang, H. Radio Frequency Analog Electronics Based on Carbon Nanotube Transistors. *Proceedings of the National Academy of Sciences* **2008**, *105* (5), 1405–1409. https://doi.org/10.1073/pnas.0709734105.

(101) Ryu, K.; Badmaev, A.; Wang, C.; Lin, A.; Patil, N.; Gomez, L.; Kumar, A.; Mitra, S.; Wong, H.-S. P.; Zhou, C. CMOS-Analogous Wafer-Scale Nanotube-on-Insulator Approach for Submicrometer Devices and Integrated Circuits Using Aligned Nanotubes. *Nano Lett.* **2009**, *9* (1), 189–197. https://doi.org/10.1021/nl802756u.

(102) Rutherglen, C.; Jain, D.; Burke, P. Nanotube Electronics for Radiofrequency Applications. *Nature Nanotech* **2009**, *4* (12), 811–819. https://doi.org/10.1038/nnano.2009.355.

(103) Park, S.; Vosguerichian, M.; Bao, Z. A Review of Fabrication and Applications of Carbon Nanotube Film-Based Flexible Electronics. *Nanoscale* **2013**, *5* (5), 1727. https://doi.org/10.1039/c3nr33560g.

(104) Cao, Q.; Kim, H.; Pimparkar, N.; Kulkarni, J. P.; Wang, C.; Shim, M.; Roy, K.; Alam, M. A.; Rogers, J. A. Medium-Scale Carbon Nanotube Thin-Film Integrated Circuits on Flexible Plastic Substrates. *Nature* **2008**, *454* (7203), 495–500. https://doi.org/10.1038/nature07110.

(105) Zhang, J.; Wang, C.; Zhou, C. Rigid/Flexible Transparent Electronics Based on Separated Carbon Nanotube Thin-Film Transistors and Their Application in Display Electronics. *ACS Nano* **2012**, *6* (8), 7412–7419. https://doi.org/10.1021/nn3026172.

(106) Chen, K.; Gao, W.; Emaminejad, S.; Kiriya, D.; Ota, H.; Nyein, H. Y. Y.; Takei, K.; Javey, A. Printed Carbon Nanotube Electronics and Sensor Systems. *Adv. Mater.* **2016**, *28* (22), 4397–4414. https://doi.org/10.1002/adma.201504958.

(107) Sun, D.; Timmermans, M. Y.; Tian, Y.; Nasibulin, A. G.; Kauppinen, E. I.; Kishimoto, S.; Mizutani, T.; Ohno, Y. Flexible High-Performance Carbon Nanotube Integrated Circuits. *Nature Nanotech* **2011**, *6* (3), 156–161. https://doi.org/10.1038/nnano.2011.1.

(108) Cao, C.; Andrews, J. B.; Franklin, A. D. Completely Printed, Flexible, Stable, and Hysteresis-Free Carbon Nanotube Thin-Film Transistors via Aerosol Jet Printing. *Adv. Electron. Mater.* **2017**, *3* (5), 1700057. https://doi.org/10.1002/aelm.201700057.

(109) Artukovic, E.; Kaempgen, M.; Hecht, D. S.; Roth, S.; Grüner, G. Transparent and Flexible Carbon Nanotube Transistors. *Nano Lett.* **2005**, *5* (4), 757–760. https://doi.org/10.1021/nl050254o.

(110) Ishikawa, F. N.; Chang, H.; Ryu, K.; Chen, P.; Badmaev, A.; Gomez De Arco, L.; Shen, G.; Zhou, C. Transparent Electronics Based on Transfer Printed Aligned Carbon Nanotubes on Rigid and Flexible Substrates. *ACS Nano* **2009**, *3* (1), 73–79. https://doi.org/10.1021/nn800434d.

(111) Yu, Y.; Luo, Y.; Guo, A.; Yan, L.; Wu, Y.; Jiang, K.; Li, Q.; Fan, S.; Wang, J. Flexible and Transparent Strain Sensors Based on Super-Aligned Carbon

Nanotube Films. *Nanoscale* **2017**, *9* (20), 6716–6723. https://doi.org/10.1039/C6NR09961K.

(112) Robinson, J. A.; Snow, E. S.; Bădescu, Ş. C.; Reinecke, T. L.; Perkins, F. K. Role of Defects in Single-Walled Carbon Nanotube Chemical Sensors. *Nano Lett.* **2006**, *6* (8), 1747–1751. https://doi.org/10.1021/nl0612289.

(113) Takahashi, T.; Takei, K.; Gillies, A. G.; Fearing, R. S.; Javey, A. Carbon Nanotube Active-Matrix Backplanes for Conformal Electronics and Sensors. *Nano Lett.* **2011**, *11* (12), 5408–5413. https://doi.org/10.1021/nl203117h.

(114) Gao, W.; Emaminejad, S.; Nyein, H. Y. Y.; Challa, S.; Chen, K.; Peck, A.; Fahad, H. M.; Ota, H.; Shiraki, H.; Kiriya, D.; Lien, D.-H.; Brooks, G. A.; Davis, R. W.; Javey, A. Fully Integrated Wearable Sensor Arrays for Multiplexed in Situ Perspiration Analysis. *Nature* **2016**, *529* (7587), 509–514. https://doi.org/10.1038/nature16521.

(115) Meshot, E. R.; Zwissler, D. W.; Bui, N.; Kuykendall, T. R.; Wang, C.; Hexemer, A.; Wu, K. J. J.; Fornasiero, F. Quantifying the Hierarchical Order in Self-Aligned Carbon Nanotubes from Atomic to Micrometer Scale. *ACS Nano* **2017**, *11* (6), 5405–5416. https://doi.org/10.1021/acsnano.6b08042.

(116) Murakami, Y.; Chiashi, S.; Miyauchi, Y.; Hu, M.; Ogura, M.; Okubo, T.; Maruyama, S. Growth of Vertically Aligned Single-Walled Carbon Nanotube Films on Quartz Substrates and Their Optical Anisotropy. *Chemical Physics Letters* **2004**, *385* (3–4), 298–303. https://doi.org/10.1016/j.cplett.2003.12.095.

(117) Li, W. Z.; Xie, S. S.; Qian, L. X.; Chang, B. H.; Zou, B. S.; Zhou, W. Y.; Zhao, R. A.; Wang, G. Large-Scale Synthesis of Aligned Carbon Nanotubes. *Science* **1996**, *274* (5293), 1701–1703. https://doi.org/10.1126/science.274.5293.1701.

(118) Kong, J.; Soh, H. T.; Cassell, A. M.; Quate, C. F.; Dai, H. Synthesis of Individual Single-Walled Carbon Nanotubes on Patterned Silicon Wafers. *Nature* **1998**, *395* (6705), 878–881. https://doi.org/10.1038/27632.

(119) Youn, S. K.; Park, H. G. Morphological Evolution of Fe–Mo Bimetallic Catalysts for Diameter and Density Modulation of Vertically Aligned Carbon Nanotubes. *J. Phys. Chem. C* **2013**, *117* (36), 18657–18665. https://doi.org/10.1021/jp402941u.

(120) Bachilo, S. M.; Balzano, L.; Herrera, J. E.; Pompeo, F.; Resasco, D. E.; Weisman, R. B. Narrow (n,m)-Distribution of Single-Walled Carbon Nanotubes Grown Using a Solid Supported Catalyst. *J. Am. Chem. Soc.* **2003**, *125* (37), 11186–11187. https://doi.org/10.1021/ja036622c.

(121) Xiang, R.; Einarsson, E.; Murakami, Y.; Shiomi, J.; Chiashi, S.; Tang, Z.; Maruyama, S. Diameter Modulation of Vertically Aligned Single-Walled Carbon Nanotubes. *ACS Nano* **2012**, *6* (8), 7472–7479. https://doi.org/10.1021/nn302750x.

(122) Sugime, H.; Noda, S.; Maruyama, S.; Yamaguchi, Y. Multiple "Optimum" Conditions for Co–Mo Catalyzed Growth of Vertically Aligned Single-Walled Carbon Nanotube Forests. *Carbon* **2009**, *47* (1), 234–241. https://doi.org/10.1016/j.carbon.2008.10.001.

(123) Chen, G.; Seki, Y.; Kimura, H.; Sakurai, S.; Yumura, M.; Hata, K.; Futaba, D. N. Diameter Control of Single-Walled Carbon Nanotube Forests from 1.3–3.0 Nm by Arc Plasma Deposition. *Sci Rep* **2015**, *4* (1), 3804. https://doi.org/10.1038/srep03804.

(124) Wyss, R. M.; Klare, J. E.; Park, H. G.; Noy, A.; Bakajin, O.; Lulevich, V. Water-Assisted Growth of Uniform 100 Mm Diameter SWCNT Arrays. *ACS Appl. Mater. Interfaces* **2014**, *6* (23), 21019–21025. https://doi.org/10.1021/am505692a.

(125) World's First Super-Growth Carbon Nanotube Mass Production Plant Opens https://www.aist.go.jp/aist_e/list/latest_research/2016/20160524/en20160524.html (accessed 2021 -10 -12).

(126) Rao, R.; Sharma, R.; Abild-Pedersen, F.; Nørskov, J. K.; Harutyunyan, A. R. Insights into Carbon Nanotube Nucleation: Cap Formation Governed by Catalyst Interfacial Step Flow. *Sci Rep* **2015**, *4* (1), 6510. https://doi.org/10.1038/srep06510.

(127) Hofmann, S.; Sharma, R.; Ducati, C.; Du, G.; Mattevi, C.; Cepek, C.; Cantoro, M.; Pisana, S.; Parvez, A.; Cervantes-Sodi, F.; Ferrari, A. C.; Dunin-Borkowski, R.; Lizzit, S.; Petaccia, L.; Goldoni, A.; Robertson, J. In Situ Observations of Catalyst Dynamics during Surface-Bound Carbon Nanotube Nucleation. *Nano Lett.* **2007**, *7* (3), 602–608. https://doi.org/10.1021/nl0624824.

(128) Kuznetsov, V. L.; Usoltseva, A. N.; Chuvilin, A. L.; Obraztsova, E. D.; Bonard, J.-M. Thermodynamic Analysis of Nucleation of Carbon Deposits on Metal Particles and Its Implications for the Growth of Carbon Nanotubes. *Physical Review B* **2001**, *64* (23). https://doi.org/10.1103/PhysRevB.64.235401.

(129) Artyukhov, V. I.; Penev, E. S.; Yakobson, B. I. Why Nanotubes Grow Chiral. *Nature Communications* **2014**, *5* (1). https://doi.org/10.1038/ncomms5892.

(130) Penev, E. S.; Artyukhov, V. I.; Yakobson, B. I. Extensive Energy Landscape Sampling of Nanotube End-Caps Reveals No Chiral-Angle Bias for Their Nucleation. *ACS Nano* **2014**, *8* (2), 1899–1906. https://doi.org/10.1021/nn406462e.

(131) Pigos, E.; Penev, E. S.; Ribas, M. A.; Sharma, R.; Yakobson, B. I.; Harutyunyan, A. R. Carbon Nanotube Nucleation Driven by Catalyst Morphology Dynamics. *ACS Nano* **2011**, *5* (12), 10096–10101. https://doi.org/10.1021/nn2040457.

(132) Zou, Y.; Li, Q.; Liu, J.; Jin, Y.; Liu, Y.; Qian, Q.; Jiang, K.; Fan, S. Diameter Distribution Control of Single-Walled Carbon Nanotubes by Etching Ferritin Nanoparticles. *Appl. Phys. Express* **2014**, *7* (5), 055102. https://doi.org/10.7567/APEX.7.055102.

(133) Ishida, M.; Hongo, H.; Nihey, F.; Ochiai, Y. Diameter-Controlled Carbon Nanotubes Grown from Lithographically Defined Nanoparticles. *Jpn. J. Appl. Phys.* **2004**, *43* (10B), L1356. https://doi.org/10.1143/JJAP.43.L1356.

(134) Jeong, G.-H.; Suzuki, S.; Kobayashi, Y.; Yamazaki, A.; Yoshimura, H.; Homma, Y. Size Control of Catalytic Nanoparticles by Thermal Treatment and Its Application to Diameter Control of Single-Walled Carbon Nanotubes. *Applied Physics Letters* **2007**, *90* (4), 043108. https://doi.org/10.1063/1.2433024.

(135) Yang, F.; Wang, X.; Zhang, D.; Yang, J.; Luo, D.; Xu, Z.; Wei, J.; Wang, J.-Q.; Xu, Z.; Peng, F.; Li, X.; Li, R.; Li, Y.; Li, M.; Bai, X.; Ding, F.; Li, Y. Chirality-Specific Growth of Single-Walled Carbon Nanotubes on Solid Alloy Catalysts. *Nature* **2014**, *510* (7506), 522–524. https://doi.org/10.1038/nature13434.

(136) Zhang, S.; Kang, L.; Wang, X.; Tong, L.; Yang, L.; Wang, Z.; Qi, K.; Deng, S.; Li, Q.; Bai, X.; Ding, F.; Zhang, J. Arrays of Horizontal Carbon Nanotubes of Controlled Chirality Grown Using Designed Catalysts. *Nature* **2017**, *543* (7644), 234–238. https://doi.org/10.1038/nature21051.

(137) Tibbetts, G. G. Why Are Carbon Filaments Tubular? *Journal of Crystal Growth* **1984**, *66* (3), 632–638. https://doi.org/10.1016/0022-0248(84)90163-5.

(138) Schebarchov, D.; Hendy, S. C.; Ertekin, E.; Grossman, J. C. Interplay of Wetting and Elasticity in the Nucleation of Carbon Nanotubes. *Physical Review Letters* **2011**, *107* (18). https://doi.org/10.1103/PhysRevLett.107.185503.

(139) Fiawoo, M.-F. C.; Bonnot, A.-M.; Amara, H.; Bichara, C.; Thibault-Pénisson, J.; Loiseau, A. Evidence of Correlation between Catalyst Particles and the Single-Wall Carbon Nanotube Diameter: A First Step towards Chirality Control. *Physical Review Letters* **2012**, *108* (19). https://doi.org/10.1103/PhysRevLett.108.195503.

(140) Bachilo, S. M.; Balzano, L.; Herrera, J. E.; Pompeo, F.; Resasco, D. E.; Weisman, R. B. Narrow (*n* , *m*)-Distribution of Single-Walled Carbon Nanotubes Grown Using a Solid Supported Catalyst. *J. Am. Chem. Soc.* **2003**, *125* (37), 11186–11187. https://doi.org/10.1021/ja036622c.

(141) Lolli, G.; Zhang, L.; Balzano, L.; Sakulchaicharoen, N.; Tan, Y.; Resasco, D. E. Tailoring (*n* , *m*) Structure of Single-Walled Carbon Nanotubes by Modifying Reaction Conditions and the Nature of the Support of CoMo Catalysts. *J. Phys. Chem. B* **2006**, *110* (5), 2108–2115. https://doi.org/10.1021/jp056095e.

(142) He, M.; Chernov, A. I.; Fedotov, P. V.; Obraztsova, E. D.; Sainio, J.; Rikkinen, E.; Jiang, H.; Zhu, Z.; Tian, Y.; Kauppinen, E. I.; Niemelä, M.; Krause, A. O. I. Predominant (6,5) Single-Walled Carbon Nanotube Growth on a Copper-Promoted Iron Catalyst. *J. Am. Chem. Soc.* **2010**, *132* (40), 13994–13996. https://doi.org/10.1021/ja106609y.

(143) Fouquet, M.; Bayer, B. C.; Esconjauregui, S.; Blume, R.; Warner, J. H.; Hofmann, S.; Schlögl, R.; Thomsen, C.; Robertson, J. Highly Chiral-Selective Growth of Single-Walled Carbon Nanotubes with a Simple Monometallic Co Catalyst. *Phys. Rev. B* **2012**, *85* (23), 235411. https://doi.org/10.1103/PhysRevB.85.235411.

(144) Wang, H.; Wei, L.; Ren, F.; Wang, Q.; Pfefferle, L. D.; Haller, G. L.; Chen, Y. Chiral-Selective $CoSO_4/SiO_2$ Catalyst for (9,8) Single-Walled Carbon Nanotube Growth. *ACS Nano* **2013**, *7* (1), 614–626. https://doi.org/10.1021/nn3047633.

(145) Artyukhov, V. I.; Penev, E. S.; Yakobson, B. I. Why Nanotubes Grow Chiral. *Nat Commun* **2014**, *5* (1), 4892. https://doi.org/10.1038/ncomms5892.

(146) Liu, Y.; Dobrinsky, A.; Yakobson, B. I. Graphene Edge from Armchair to Zigzag: The Origins of Nanotube Chirality? *Phys. Rev. Lett.* **2010**, *105* (23), 235502. https://doi.org/10.1103/PhysRevLett.105.235502.

(147) Ding, F.; Harutyunyan, A. R.; Yakobson, B. I. Dislocation Theory of Chirality-Controlled Nanotube Growth. *PNAS* **2009**, *106* (8), 2506–2509. https://doi.org/10.1073/pnas.0811946106.

(148) Chao, H.-Y.; Jiang, H.; Ospina-Acevedo, F.; Balbuena, P. B.; Kauppinen, E. I.; Cumings, J.; Sharma, R. A Structure and Activity Relationship for Single-Walled Carbon Nanotube Growth Confirmed by *in Situ* Observations and Modeling. *Nanoscale* **2020**, *12* (42), 21923–21931. https://doi.org/10.1039/D0NR05916A.

(149) Friesner, R. A. Ab Initio Quantum Chemistry: Methodology and Applications. *PNAS* **2005**, *102* (19), 6648–6653. https://doi.org/10.1073/pnas.0408036102.

(150) Sholl, D. S.; Steckel, J. A. *Density Functional Theory: A Practical Introduction*; Wiley: Hoboken, N.J, 2009.

(151) Lee, J. G. *Computational Materials Science: An Introduction*; 2011.

(152) Miller, D. A. B. *Quantum Mechanics for Scientists and Engineers*; Cambridge University Press: Cambridge ; New York, 2008.

(153) Fulde, P. *Electron Correlations in Molecules and Solids*; Cardona, M., Fulde, P., von Klitzing, K., Queisser, H.-J., Merlin, R., Störmer, H., Series Eds.; Springer Series in Solid-State Sciences; Springer Berlin Heidelberg: Berlin, Heidelberg, 1995; Vol. 100. https://doi.org/10.1007/978-3-642-57809-0.

(154) Tomita, N.; Ten-no, S.; Tanimura, Y. Ab Initio Molecular Orbital Calculations by the Resonating Hartree-Fock Approach: Superposition of Non-Orthogonal Slater Determinants. *Chemical Physics Letters* **1996**, *263* (5), 687–690. https://doi.org/10.1016/S0009-2614(96)01266-3.

(155) Hohenberg, P.; Kohn, W. Inhomogeneous Electron Gas. *Phys. Rev.* **1964**, *136* (3B), B864–B871. https://doi.org/10.1103/PhysRev.136.B864.

(156) Johnson, B. G.; Gill, P. M. W.; Pople, J. A. The Performance of a Family of Density Functional Methods. *The Journal of Chemical Physics* **1993**, *98* (7), 5612–5626. https://doi.org/10.1063/1.464906.

(157) Becke, A. D. Density-Functional Exchange-Energy Approximation with Correct Asymptotic Behavior. *Phys. Rev. A* **1988**, *38* (6), 3098–3100. https://doi.org/10.1103/PhysRevA.38.3098.

(158) Becke, A. D. Density-functional Thermochemistry. III. The Role of Exact Exchange. *The Journal of Chemical Physics* **1993**, *98* (7), 5648–5652. https://doi.org/10.1063/1.464913.

(159) Kohn, W.; Sham, L. J. Self-Consistent Equations Including Exchange and Correlation Effects. *Phys. Rev.* **1965**, *140* (4A), A1133–A1138. https://doi.org/10.1103/PhysRev.140.A1133.

(160) Schleder, G. R.; Padilha, A. C. M.; Acosta, C. M.; Costa, M.; Fazzio, A. From DFT to Machine Learning: Recent Approaches to Materials Science–a Review. *J. Phys. Mater.* **2019**, *2* (3), 032001. https://doi.org/10.1088/2515-7639/ab084b.

(161) Payne, M. C.; Teter, M. P.; Allan, D. C.; Arias, T. A.; Joannopoulos, J. D. Iterative Minimization Techniques for *Ab Initio* Total-Energy Calculations: Molecular Dynamics and Conjugate Gradients. *Rev. Mod. Phys.* **1992**, *64* (4), 1045–1097. https://doi.org/10.1103/RevModPhys.64.1045.

(162) Grimme, S. Semiempirical GGA-Type Density Functional Constructed with a Long-Range Dispersion Correction. *Journal of Computational Chemistry* **2006**, *27* (15), 1787–1799. https://doi.org/10.1002/jcc.20495.

(163) Hubbard, J. Electron Correlations in Narrow Energy Bands. *Proc. R. Soc. Lond. A* **1963**, *276* (1365), 238–257. https://doi.org/10.1098/rspa.1963.0204.

(164) Anisimov, V. I.; Zaanen, J.; Andersen, O. K. Band Theory and Mott Insulators: Hubbard *U* Instead of Stoner *I*. *Phys. Rev. B* **1991**, *44* (3), 943–954. https://doi.org/10.1103/PhysRevB.44.943.

(165) Dudarev, S. L.; Botton, G. A.; Savrasov, S. Y.; Humphreys, C. J.; Sutton, A. P. Electron-Energy-Loss Spectra and the Structural Stability of Nickel Oxide: An LSDA+U Study. *Phys. Rev. B* **1998**, *57* (3), 1505–1509. https://doi.org/10.1103/PhysRevB.57.1505.

(166) Phillips, J. C.; Kleinman, L. New Method for Calculating Wave Functions in Crystals and Molecules. *Phys. Rev.* **1959**, *116* (2), 287–294. https://doi.org/10.1103/PhysRev.116.287.

(167) Blöchl, P. E. Projector Augmented-Wave Method. *Physical Review B* **1994**, *50* (24), 17953–17979. https://doi.org/10.1103/PhysRevB.50.17953.

(168) Troullier, N.; Martins, J. L. Efficient Pseudopotentials for Plane-Wave Calculations. *Phys. Rev. B* **1991**, *43* (3), 1993–2006. https://doi.org/10.1103/PhysRevB.43.1993.

(169) Vanderbilt, D. Soft Self-Consistent Pseudopotentials in a Generalized Eigenvalue Formalism. *Phys. Rev. B* **1990**, *41* (11), 7892–7895. https://doi.org/10.1103/PhysRevB.41.7892.

(170) Lejaeghere, K.; Bihlmayer, G.; Björkman, T.; Blaha, P.; Blügel, S.; Blum, V.; Caliste, D.; Castelli, I. E.; Clark, S. J.; Dal Corso, A.; de Gironcoli, S.; Deutsch, T.; Dewhurst, J. K.; Di Marco, I.; Draxl, C.; Dułak, M.; Eriksson, O.; Flores-Livas, J. A.; Garrity, K. F.; Genovese, L.; Giannozzi, P.; Giantomassi, M.; Goedecker, S.; Gonze, X.; Grånäs, O.; Gross, E. K. U.; Gulans, A.; Gygi, F.; Hamann, D. R.; Hasnip, P. J.; Holzwarth, N. A. W.; Iuşan, D.; Jochym, D. B.; Jollet, F.; Jones, D.; Kresse, G.; Koepernik, K.; Küçükbenli, E.; Kvashnin, Y. O.; Locht, I. L. M.; Lubeck, S.; Marsman, M.; Marzari, N.; Nitzsche, U.; Nordström, L.; Ozaki, T.; Paulatto, L.; Pickard, C. J.; Poelmans, W.; Probert, M. I. J.; Refson, K.; Richter, M.; Rignanese, G.-M.; Saha, S.; Scheffler, M.; Schlipf, M.; Schwarz, K.; Sharma, S.; Tavazza, F.; Thunström, P.; Tkatchenko, A.; Torrent, M.; Vanderbilt, D.; van Setten, M. J.; Van Speybroeck, V.; Wills, J. M.; Yates, J. R.; Zhang, G.-X.; Cottenier, S. Reproducibility in Density Functional Theory Calculations of Solids. *Science* **2016**, *351* (6280), aad3000. https://doi.org/10.1126/science.aad3000.

(171) Bloch, F. Über die Quantenmechanik der Elektronen in Kristallgittern. *Z. Physik* **1929**, *52* (7–8), 555–600. https://doi.org/10.1007/BF01339455.

(172) Henkelman, G.; Jónsson, H. Improved Tangent Estimate in the Nudged Elastic Band Method for Finding Minimum Energy Paths and Saddle Points. *The Journal of Chemical Physics* **2000**, *113* (22), 9978–9985. https://doi.org/10.1063/1.1323224.

(173) Henkelman, G.; Uberuaga, B. P.; Jónsson, H. A Climbing Image Nudged Elastic Band Method for Finding Saddle Points and Minimum Energy Paths. *The Journal of Chemical Physics* **2000**, *113* (22), 9901–9904. https://doi.org/10.1063/1.1329672.

(174) Ding, F.; Harutyunyan, A. R.; Yakobson, B. I. Dislocation Theory of Chirality-Controlled Nanotube Growth. *Proceedings of the National Academy of Sciences* **2009**, *106* (8), 2506–2509. https://doi.org/10.1073/pnas.0811946106.

(175) Reich, S.; Li, L.; Robertson, J. Epitaxial Growth of Carbon Caps on Ni for Chiral Selectivity. *physica status solidi (b)* **2006**, *243* (13), 3494–3499. https://doi.org/10.1002/pssb.200669224.

(176) Gibbs, J. W. *Elementary Principles in Statistical Mechanics*; Courier Corporation, 2014.

(177) Kudin, K. N.; Scuseria, G. E.; Yakobson, B. I. C 2 F , BN, and C Nanoshell Elasticity from Ab Initio Computations. *Physical Review B* **2001**, *64* (23). https://doi.org/10.1103/PhysRevB.64.235406.

(178) Adams, G. B.; Sankey, O. F.; Page, J. B.; O'Keeffe, M.; Drabold, D. A. Energetics of Large Fullerenes: Balls, Tubes, and Capsules. *Science* **1992**, *256* (5065), 1792–1795. https://doi.org/10.1126/science.256.5065.1792.

(179) Sawada, S.; Hamada, N. Energetics of Carbon Nano-Tubes. *Solid State Communications* **1992**, *83* (11), 917–919. https://doi.org/10.1016/0038-1098(92)90911-R.

(180) Robertson, D. H.; Brenner, D. W.; Mintmire, J. W. Energetics of Nanoscale Graphitic Tubules. *Physical Review B* **1992**, *45* (21), 12592–12595. https://doi.org/10.1103/PhysRevB.45.12592.

(181) Gülseren, O.; Yildirim, T.; Ciraci, S. Systematic Ab Initio Study of Curvature Effects in Carbon Nanotubes. *Physical Review B* **2002**, *65* (15). https://doi.org/10.1103/PhysRevB.65.153405.

(182) Jourdain, V.; Bichara, C. Current Understanding of the Growth of Carbon Nanotubes in Catalytic Chemical Vapour Deposition. *Carbon* **2013**, *58*, 2–39. https://doi.org/10.1016/j.carbon.2013.02.046.

(183) *Handbook of Mathematical Functions: With Formulas, Graphs, and Mathematical Tables*, 9. Dover print.; [Nachdr. der Ausg. von 1972].; Abramowitz, M., Stegun, I. A., Eds.; Dover books on mathematics; Dover Publ: New York, NY, 2013.

(184) Perdew, J. P.; Burke, K.; Ernzerhof, M. Generalized Gradient Approximation Made Simple. *Physical Review Letters* **1996**, *77* (18), 3865–3868. https://doi.org/10.1103/PhysRevLett.77.3865.

(185) Kresse, G.; Joubert, D. From Ultrasoft Pseudopotentials to the Projector Augmented-Wave Method. *Physical Review B* **1999**, *59* (3), 1758–1775. https://doi.org/10.1103/PhysRevB.59.1758.

(186) Monkhorst, H. J.; Pack, J. D. Special Points for Brillouin-Zone Integrations. *Physical Review B* **1976**, *13* (12), 5188–5192. https://doi.org/10.1103/PhysRevB.13.5188.

(187) Li, B.; Chen, L.; Pan, X. Spin-Flip Phenomena at the Co|graphene|Co Interfaces. *Appl. Phys. Lett.* **2011**, *98* (13), 133111. https://doi.org/10.1063/1.3571553.

(188) Swart, J. C. W.; van Steen, E.; Ciobícă, I. M.; van Santen, R. A. Interaction of Graphene with FCC–Co(111). *Phys. Chem. Chem. Phys.* **2009**, *11* (5), 803–807. https://doi.org/10.1039/B814664K.

(189) Khomyakov, P. A.; Giovannetti, G.; Rusu, P. C.; Brocks, G.; van den Brink, J.; Kelly, P. J. First-Principles Study of the Interaction and Charge Transfer between Graphene and Metals. *Phys. Rev. B* **2009**, *79* (19), 195425. https://doi.org/10.1103/PhysRevB.79.195425.

(190) Vanin, M.; Mortensen, J. J.; Kelkkanen, A. K.; Garcia-Lastra, J. M.; Thygesen, K. S.; Jacobsen, K. W. Graphene on Metals: A van Der Waals Density Functional Study. *Phys. Rev. B* **2010**, *81* (8), 081408. https://doi.org/10.1103/PhysRevB.81.081408.

(191) Xu, Z.; Buehler, M. J. Interface Structure and Mechanics between Graphene and Metal Substrates: A First-Principles Study. *J. Phys.: Condens. Matter* **2010**, *22* (48), 485301. https://doi.org/10.1088/0953-8984/22/48/485301.

(192) Fuentes-Cabrera, M.; Baskes, M. I.; Melechko, A. V.; Simpson, M. L. Bridge Structure for the Graphene/Ni(111) System: A First Principles Study. *Phys. Rev. B* **2008**, *77* (3), 035405. https://doi.org/10.1103/PhysRevB.77.035405.

(193) Zhao, W.; Kozlov, S. M.; Höfert, O.; Gotterbarm, K.; Lorenz, M. P. A.; Viñes, F.; Papp, C.; Görling, A.; Steinrück, H.-P. Graphene on Ni(111): Coexistence of Different Surface Structures. *J. Phys. Chem. Lett.* **2011**, *2* (7), 759–764. https://doi.org/10.1021/jz200043p.

(194) Christian, M. S.; Otero-de-la-Roza, A.; Johnson, E. R. Adsorption of Graphene to Nickel (111) Using the Exchange-Hole Dipole Moment Model. *Carbon* **2017**, *118*, 184–191. https://doi.org/10.1016/j.carbon.2017.03.024.

(195) Janthon, P.; Viñes, F.; Kozlov, S. M.; Limtrakul, J.; Illas, F. Theoretical Assessment of Graphene-Metal Contacts. *The Journal of Chemical Physics* **2013**, *138* (24), 244701. https://doi.org/10.1063/1.4807855.

(196) Rosei, R.; De Crescenzi, M.; Sette, F.; Quaresima, C.; Savoia, A.; Perfetti, P. Structure of Graphitic Carbon on Ni(111): A Surface Extended-Energy-Loss Fine-Structure Study. *Phys. Rev. B* **1983**, *28* (2), 1161–1164. https://doi.org/10.1103/PhysRevB.28.1161.

(197) Gamo, Y.; Nagashima, A.; Wakabayashi, M.; Terai, M.; Oshima, C. Atomic Structure of Monolayer Graphite Formed on Ni(111). *Surface Science* **1997**, *374* (1–3), 61–64. https://doi.org/10.1016/S0039-6028(96)00785-6.

(198) Kawanowa, H.; Ozawa, H.; Yazaki, T.; Gotoh, Y.; Souda, R. Structure Analysis of Monolayer Graphite on Ni(111) Surface by Li^{+} -Impact Collision Ion Scattering Spectroscopy. *Jpn. J. Appl. Phys.* **2002**, *41* (Part 1, No. 10), 6149–6152. https://doi.org/10.1143/JJAP.41.6149.

(199) Restuccia, P.; Righi, M. C. Tribochemistry of Graphene on Iron and Its Possible Role in Lubrication of Steel. *Carbon* **2016**, *106*, 118–124. https://doi.org/10.1016/j.carbon.2016.05.025.

(200) Vinogradov, N. A.; Zakharov, A. A.; Kocevski, V.; Rusz, J.; Simonov, K. A.; Eriksson, O.; Mikkelsen, A.; Lundgren, E.; Vinogradov, A. S.; Mårtensson, N.; Preobrajenski, A. B. Formation and Structure of Graphene Waves on Fe(110). *Phys. Rev. Lett.* **2012**, *109* (2), 026101. https://doi.org/10.1103/PhysRevLett.109.026101.

(201) Picher, M.; Lin, P. A.; Gomez-Ballesteros, J. L.; Balbuena, P. B.; Sharma, R. Nucleation of Graphene and Its Conversion to Single-Walled Carbon Nanotubes. *Nano Letters* **2014**, *14* (11), 6104–6108. https://doi.org/10.1021/nl501977b.

(202) Christian, M. S.; Otero-de-la-Roza, A.; Johnson, E. R. Adsorption of Graphene to Metal (111) Surfaces Using the Exchange-Hole Dipole Moment Model. *Carbon* **2017**, *124*, 531–540. https://doi.org/10.1016/j.carbon.2017.08.077.

(203) Steinmann, S. N.; Corminboeuf, C. A Generalized-Gradient Approximation Exchange Hole Model for Dispersion Coefficients. *The Journal of Chemical Physics* **2011**, *134* (4), 044117. https://doi.org/10.1063/1.3545985.

(204) Steinmann, S. N.; Corminboeuf, C. Comprehensive Benchmarking of a Density-Dependent Dispersion Correction. *Journal of Chemical Theory and Computation* **2011**, *7* (11), 3567–3577. https://doi.org/10.1021/ct200602x.

(205) Reich, S.; Maultzsch, J.; Thomsen, C.; Ordejón, P. Tight-Binding Description of Graphene. *Phys. Rev. B* **2002**, *66* (3), 035412. https://doi.org/10.1103/PhysRevB.66.035412.

(206) Burgos, J. C.; Reyna, H.; Yakobson, B. I.; Balbuena, P. B. Interplay of Catalyst Size and Metal−Carbon Interactions on the Growth of Single-Walled Carbon Nanotubes. *The Journal of Physical Chemistry C* **2010**, *114* (15), 6952–6958. https://doi.org/10.1021/jp911905p.

(207) Ribas, M. A.; Ding, F.; Balbuena, P. B.; Yakobson, B. I. Nanotube Nucleation versus Carbon-Catalyst Adhesion–Probed by Molecular Dynamics Simulations. *The Journal of Chemical Physics* **2009**, *131* (22), 224501. https://doi.org/10.1063/1.3266947.

(208) Yakobson, B. I.; Brabec, C. J.; Bernholc, J. Nanomechanics of Carbon Tubes: Instabilities beyond Linear Response. *Physical Review Letters* **1996**, *76* (14), 2511–2514. https://doi.org/10.1103/PhysRevLett.76.2511.

(209) Huang, Y.; Wu, J.; Hwang, K. C. Thickness of Graphene and Single-Wall Carbon Nanotubes. *Physical Review B* **2006**, *74* (24). https://doi.org/10.1103/PhysRevB.74.245413.

(210) Zang, J.-L.; Yuan, Q.; Wang, F.-C.; Zhao, Y.-P. A Comparative Study of Young's Modulus of Single-Walled Carbon Nanotube by CPMD, MD and First

Principle Simulations. *Computational Materials Science* **2009**, *46* (3), 621–625. https://doi.org/10.1016/j.commatsci.2009.04.007.

(211) Cai, J.; Wang, C. Y.; Yu, T.; Yu, S. Wall Thickness of Single-Walled Carbon Nanotubes and Its Young's Modulus. *Physica Scripta* **2009**, *79* (2), 025702. https://doi.org/10.1088/0031-8949/79/02/025702.

(212) Vodenitcharova, T.; Zhang, L. C. Effective Wall Thickness of a Single-Walled Carbon Nanotube. *Physical Review B* **2003**, *68* (16). https://doi.org/10.1103/PhysRevB.68.165401.

(213) Hernández, E.; Goze, C.; Bernier, P.; Rubio, A. Elastic Properties of C and B x C y N z Composite Nanotubes. *Physical Review Letters* **1998**, *80* (20), 4502–4505. https://doi.org/10.1103/PhysRevLett.80.4502.

(214) Lu, J. P. Elastic Properties of Carbon Nanotubes and Nanoropes. *Physical Review Letters* **1997**, *79* (7), 1297–1300. https://doi.org/10.1103/PhysRevLett.79.1297.

(215) Krishnan, A.; Dujardin, E.; Ebbesen, T. W.; Yianilos, P. N.; Treacy, M. M. J. Young's Modulus of Single-Walled Nanotubes. *Physical Review B* **1998**, *58* (20), 14013–14019. https://doi.org/10.1103/PhysRevB.58.14013.

(216) Salvetat, J.-P.; Briggs, G.; Bonard, J.-M.; Bacsa, R.; Kulik, A.; Stöckli, T.; Burnham, N.; Forró, L. Elastic and Shear Moduli of Single-Walled Carbon Nanotube Ropes. *Physical Review Letters* **1999**, *82* (5), 944–947. https://doi.org/10.1103/PhysRevLett.82.944.

(217) Tombler, T. W.; Zhou, C.; Alexseyev, L.; Kong, J.; Dai, H.; Liu, L.; Jayanthi, C. S.; Tang, M.; Wu, S.-Y. Reversible Electromechanical Characteristics of Carbon Nanotubes Underlocal-Probe Manipulation. *Nature* **2000**, *405* (6788), 769–772. https://doi.org/10.1038/35015519.

(218) Wong, E. W.; Sheehan, P. E.; Lieber, C. M. Nanobeam Mechanics: Elasticity, Strength, and Toughness of Nanorods and Nanotubes. *Science* **1997**, *277* (5334), 1971–1975. https://doi.org/10.1126/science.277.5334.1971.

(219) Hafner, J. H.; Bronikowski, M. J.; Azamian, B. R.; Nikolaev, P.; Rinzler, A. G.; Colbert, D. T.; Smith, K. A.; Smalley, R. E. Catalytic Growth of Single-Wall

Carbon Nanotubes from Metal Particles. *Chemical Physics Letters* **1998**, *296* (1–2), 195–202. https://doi.org/10.1016/S0009-2614(98)01024-0.

(220) Burgos, J. C.; Jones, E.; Balbuena, P. B. Effect of the Metal−Substrate Interaction Strength on the Growth of Single-Walled Carbon Nanotubes. *J. Phys. Chem. C* **2011**, *115* (15), 7668–7675. https://doi.org/10.1021/jp200919j.

(221) Gómez-Gualdrón, D. A.; Balbuena, P. B. Characterization of Carbon Atomistic Pathways during Single-Walled Carbon Nanotube Growth on Supported Metal Nanoparticles. *Carbon* **2013**, *57*, 298–309. https://doi.org/10.1016/j.carbon.2013.01.077.

(222) Magnin, Y.; Zappelli, A.; Amara, H.; Ducastelle, F.; Bichara, C. Size Dependent Phase Diagrams of Nickel-Carbon Nanoparticles. *Phys. Rev. Lett.* **2015**, *115* (20), 205502. https://doi.org/10.1103/PhysRevLett.115.205502.

(223) He, M.; Jiang, H.; Liu, B.; Fedotov, P. V.; Chernov, A. I.; Obraztsova, E. D.; Cavalca, F.; Wagner, J. B.; Hansen, T. W.; Anoshkin, I. V.; Obraztsova, E. A.; Belkin, A. V.; Sairanen, E.; Nasibulin, A. G.; Lehtonen, J.; Kauppinen, E. I. Chiral-Selective Growth of Single-Walled Carbon Nanotubes on Lattice-Mismatched Epitaxial Cobalt Nanoparticles. *Scientific Reports* **2013**, *3* (1). https://doi.org/10.1038/srep01460.

(224) He, M.; Magnin, Y.; Jiang, H.; Amara, H.; Kauppinen, E. I.; Loiseau, A.; Bichara, C. Growth Modes and Chiral Selectivity of Single-Walled Carbon Nanotubes. *Nanoscale* **2018**, *10* (14), 6744–6750. https://doi.org/10.1039/C7NR09539B.

(225) Song, J.; Du, G.; Song, C.; Zhao, J.; Feng, S.; Zheng, J.; Zhu, Z. Identification and Technical Accessibility of the Carbon Self-Assembly Concept Hidden in Catalytic Carbon Nanotube Evolution. *J. Mater. Chem.* **2009**, *19* (41), 7725. https://doi.org/10.1039/b912203f.

(226) Rümmeli, M. H.; Borowiak-Palen, E.; Gemming, T.; Pichler, T.; Knupfer, M.; Kalbác, M.; Dunsch, L.; Jost, O.; Silva, S. R. P.; Pompe, W.; Büchner, B. Novel Catalysts, Room Temperature, and the Importance of Oxygen for the Synthesis of Single-Walled Carbon Nanotubes. *Nano Lett.* **2005**, *5* (7), 1209–1215. https://doi.org/10.1021/nl050692v.

(227) Rümmeli, M. H.; Schäffel, F.; Kramberger, C.; Gemming, T.; Bachmatiuk, A.; Kalenczuk, R. J.; Rellinghaus, B.; Büchner, B.; Pichler, T. Oxide-Driven Carbon Nanotube Growth in Supported Catalyst CVD. *J. Am. Chem. Soc.* **2007**, *129* (51), 15772–15773. https://doi.org/10.1021/ja0779405.

(228) Mazzoni, M. S. C.; Chacham, H.; Ordejón, P.; Sánchez-Portal, D.; Soler, J. M.; Artacho, E. Energetics of the Oxidation and Opening of a Carbon Nanotube. *Phys. Rev. B* **1999**, *60* (4), R2208–R2211. https://doi.org/10.1103/PhysRevB.60.R2208.

(229) Błoński, P.; Kiejna, A. Structural, Electronic, and Magnetic Properties of Bcc Iron Surfaces. *Surface Science* **2007**, *601* (1), 123–133. https://doi.org/10.1016/j.susc.2006.09.013.

(230) Kresse, G.; Furthmüller, J. Efficient Iterative Schemes for Ab Initio Total-Energy Calculations Using a Plane-Wave Basis Set. *Phys. Rev. B* **1996**, *54* (16), 11169–11186. https://doi.org/10.1103/PhysRevB.54.11169.

(231) Meng, Y.; Liu, X.-W.; Huo, C.-F.; Guo, W.-P.; Cao, D.-B.; Peng, Q.; Dearden, A.; Gonze, X.; Yang, Y.; Wang, J.; Jiao, H.; Li, Y.; Wen, X.-D. When Density Functional Approximations Meet Iron Oxides. *J. Chem. Theory Comput.* **2016**, *12* (10), 5132–5144. https://doi.org/10.1021/acs.jctc.6b00640.

(232) van de Loosdrecht, J.; Botes, F. G.; Ciobica, I. M.; Ferreira, A.; Gibson, P.; Moodley, D. J.; Saib, A. M.; Visagie, J. L.; Weststrate, C. J.; Niemantsverdriet, J. W. 7.20 - Fischer–Tropsch Synthesis: Catalysts and Chemistry. In *Comprehensive Inorganic Chemistry II (Second Edition)*; Reedijk, J., Poeppelmeier, K., Eds.; Elsevier: Amsterdam, 2013; pp 525–557. https://doi.org/10.1016/B978-0-08-097774-4.00729-4.

(233) Moyer, K.; Zohair, M.; Eaves-Rathert, J.; Douglas, A.; Pint, C. L. Oxygen Evolution Activity Limits the Nucleation and Catalytic Growth of Carbon Nanotubes from Carbon Dioxide Electrolysis via Molten Carbonates. *Carbon* **2020**, *165*, 90–99. https://doi.org/10.1016/j.carbon.2020.04.037.

(234) Tripathi, N.; Islam, S. S. A New Approach for Orientation-Controlled Growth of CNTs: An in-Depth Analysis on the Role of Oxygen Plasma Treatment to Catalyst. *Appl Nanosci* **2017**, *7* (3–4), 125–129. https://doi.org/10.1007/s13204-017-0549-z.

(235) Teblum, E.; Gofer, Y.; Pint, C. L.; Nessim, G. D. Role of Catalyst Oxidation State in the Growth of Vertically Aligned Carbon Nanotubes. *J. Phys. Chem. C* **2012**, *116* (46), 24522–24528. https://doi.org/10.1021/jp305169b.

(236) Grimme, S.; Antony, J.; Ehrlich, S.; Krieg, H. A Consistent and Accurate Ab Initio Parametrization of Density Functional Dispersion Correction (DFT-D) for the 94 Elements H-Pu. *The Journal of Chemical Physics* **2010**, *132* (15), 154104. https://doi.org/10.1063/1.3382344.

(237) Grimme, S.; Ehrlich, S.; Goerigk, L. Effect of the Damping Function in Dispersion Corrected Density Functional Theory. *J. Comput. Chem.* **2011**, *32* (7), 1456–1465. https://doi.org/10.1002/jcc.21759.

(238) Yang, F.; Wang, M.; Zhang, D.; Yang, J.; Zheng, M.; Li, Y. Chirality Pure Carbon Nanotubes: Growth, Sorting, and Characterization. *Chem. Rev.* **2020**, *120* (5), 2693–2758. https://doi.org/10.1021/acs.chemrev.9b00835.

(239) Zhang, S.; Kang, L.; Wang, X.; Tong, L.; Yang, L.; Wang, Z.; Qi, K.; Deng, S.; Li, Q.; Bai, X.; Ding, F.; Zhang, J. Arrays of Horizontal Carbon Nanotubes of Controlled Chirality Grown Using Designed Catalysts. *Nature* **2017**, *543* (7644), 234–238. https://doi.org/10.1038/nature21051.

(240) Gómez-Gualdrón, D. A.; Balbuena, P. B. The Role of Cap Chirality in the Mechanism of Growth of Single-Wall Carbon Nanotubes. *Nanotechnology* **2008**, *19* (48), 485604. https://doi.org/10.1088/0957-4484/19/48/485604.

(241) Gómez-Gualdrón, D. A.; Balbuena, P. B. Growth of Chiral Single-Walled Carbon Nanotube Caps in the Presence of a Cobalt Cluster. *Nanotechnology* **2009**, *20* (21), 215601. https://doi.org/10.1088/0957-4484/20/21/215601.

(242) Gómez-Gualdrón, D. A.; Balbuena, P. B. Effect of Metal Cluster-Cap Interactions on the Catalyzed Growth of Single-Wall Carbon Nanotubes. *J. Phys. Chem. C* **2009**, *113* (2), 698–709. https://doi.org/10.1021/jp808457j.

(243) Burgos, J. C.; Jones, E.; Balbuena, P. B. Effect of the Metal−Substrate Interaction Strength on the Growth of Single-Walled Carbon Nanotubes. *The Journal of Physical Chemistry C* **2011**, *115* (15), 7668–7675. https://doi.org/10.1021/jp200919j.

(244) Rahmati, M.; Safdari, M.-S.; Fletcher, T. H.; Argyle, M. D.; Bartholomew, C. H. Chemical and Thermal Sintering of Supported Metals with Emphasis on Cobalt Catalysts During Fischer–Tropsch Synthesis. *Chem. Rev.* **2020**, *120* (10), 4455–4533. https://doi.org/10.1021/acs.chemrev.9b00417.

(245) Esconjauregui, S.; Whelan, C. M.; Maex, K. The Reasons Why Metals Catalyze the Nucleation and Growth of Carbon Nanotubes and Other Carbon Nanomorphologies. *Carbon* **2009**, *47* (3), 659–669. https://doi.org/10.1016/j.carbon.2008.10.047.

(246) Hernadi, K.; Fonseca, A.; Nagy, J. B.; Siska, A.; Kiricsi, I. Production of Nanotubes by the Catalytic Decomposition of Different Carbon-Containing Compounds. *Applied Catalysis A: General* **2000**, *199* (2), 245–255. https://doi.org/10.1016/S0926-860X(99)00561-X.

(247) Li, Q.; Yan, H.; Zhang, J.; Liu, Z. Effect of Hydrocarbons Precursors on the Formation of Carbon Nanotubes in Chemical Vapor Deposition. *Carbon* **2004**, *42* (4), 829–835. https://doi.org/10.1016/j.carbon.2004.01.070.

(248) Murakami, Y.; Chiashi, S.; Miyauchi, Y.; Hu, M.; Ogura, M.; Okubo, T.; Maruyama, S. Growth of Vertically Aligned Single-Walled Carbon Nanotube Films on Quartz Substrates and Their Optical Anisotropy. *Chemical Physics Letters* **2004**, *385* (3–4), 298–303. https://doi.org/10.1016/j.cplett.2003.12.095.

(249) Maruyama, S.; Kojima, R.; Miyauchi, Y.; Chiashi, S.; Kohno, M. Low-Temperature Synthesis of High-Purity Single-Walled Carbon Nanotubes from Alcohol. *Chemical Physics Letters* **2002**, *360* (3–4), 229–234. https://doi.org/10.1016/S0009-2614(02)00838-2.

(250) Nikolaev, P.; Bronikowski, M. J.; Bradley, R. K.; Rohmund, F.; Colbert, D. T.; Smith, K. A.; Smalley, R. E. Gas-Phase Catalytic Growth of Single-Walled Carbon Nanotubes from Carbon Monoxide. *Chemical Physics Letters* **1999**, *313* (1–2), 91–97. https://doi.org/10.1016/S0009-2614(99)01029-5.

(251) Zhang, G.; Mann, D.; Zhang, L.; Javey, A.; Li, Y.; Yenilmez, E.; Wang, Q.; McVittie, J. P.; Nishi, Y.; Gibbons, J.; Dai, H. Ultra-High-Yield Growth of Vertical Single-Walled Carbon Nanotubes: Hidden Roles of Hydrogen and Oxygen. *Proceedings of the National Academy of Sciences* **2005**, *102* (45), 16141–16145. https://doi.org/10.1073/pnas.0507064102.

(252) Hussain, A.; Liao, Y.; Zhang, Q.; Ding, E.-X.; Laiho, P.; Ahmad, S.; Wei, N.; Tian, Y.; Jiang, H.; Kauppinen, E. I. Floating Catalyst CVD Synthesis of Single Walled Carbon Nanotubes from Ethylene for High Performance Transparent Electrodes. *Nanoscale* **2018**, *10* (20), 9752–9759. https://doi.org/10.1039/C8NR00716K.

(253) Zhong, G.; Hofmann, S.; Yan, F.; Telg, H.; Warner, J. H.; Eder, D.; Thomsen, C.; Milne, W. I.; Robertson, J. Acetylene: A Key Growth Precursor for Single-Walled Carbon Nanotube Forests. *J. Phys. Chem. C* **2009**, *113* (40), 17321–17325. https://doi.org/10.1021/jp905134b.

(254) Huh, Y.; Green, M. L. H.; Kim, Y. H.; Lee, J. Y.; Lee, C. J. Control of Carbon Nanotube Growth Using Cobalt Nanoparticles as Catalyst. *Applied Surface Science* **2005**, *249* (1–4), 145–150. https://doi.org/10.1016/j.apsusc.2004.11.059.

(255) De Volder, M. F. L.; Tawfick, S. H.; Baughman, R. H.; Hart, A. J. Carbon Nanotubes: Present and Future Commercial Applications. *Science* **2013**, *339* (6119), 535–539. https://doi.org/10.1126/science.1222453.

(256) He, M.; Zhang, S.; Zhang, J. Horizontal Single-Walled Carbon Nanotube Arrays: Controlled Synthesis, Characterizations, and Applications. *Chem. Rev.* **2020**, *120* (22), 12592–12684. https://doi.org/10.1021/acs.chemrev.0c00395.

(257) Wang, Y.; Qiu, L.; Zhang, L.; Tang, D.-M.; Ma, R.; Wang, Y.; Zhang, B.; Ding, F.; Liu, C.; Cheng, H.-M. Precise Identification of the Active Phase of Cobalt Catalyst for Carbon Nanotube Growth by *In Situ* Transmission Electron Microscopy. *ACS Nano* **2020**, *14* (12), 16823–16831. https://doi.org/10.1021/acsnano.0c05542.

(258) Lin, M.; Ying Tan, J. P.; Boothroyd, C.; Loh, K. P.; Tok, E. S.; Foo, Y.-L. Direct Observation of Single-Walled Carbon Nanotube Growth at the Atomistic Scale. *Nano Lett.* **2006**, *6* (3), 449–452. https://doi.org/10.1021/nl052356k.

(259) Hofmann, S.; Sharma, R.; Ducati, C.; Du, G.; Mattevi, C.; Cepek, C.; Cantoro, M.; Pisana, S.; Parvez, A.; Cervantes-Sodi, F.; Ferrari, A. C.; Dunin-Borkowski, R.; Lizzit, S.; Petaccia, L.; Goldoni, A.; Robertson, J. In Situ Observations of Catalyst Dynamics during Surface-Bound Carbon Nanotube Nucleation. *Nano Letters* **2007**, *7* (3), 602–608. https://doi.org/10.1021/nl0624824.

(260) Hofmann, S.; Blume, R.; Wirth, C. T.; Cantoro, M.; Sharma, R.; Ducati, C.; Hävecker, M.; Zafeiratos, S.; Schnoerch, P.; Oestereich, A.; Teschner, D.; Albrecht, M.; Knop-Gericke, A.; Schlögl, R.; Robertson, J. State of Transition Metal Catalysts During Carbon Nanotube Growth. *The Journal of Physical Chemistry C* **2009**, *113* (5), 1648–1656. https://doi.org/10.1021/jp808560p.

(261) Yoshida, H.; Takeda, S.; Uchiyama, T.; Kohno, H.; Homma, Y. Atomic-Scale In-Situ Observation of Carbon Nanotube Growth from Solid State Iron Carbide Nanoparticles. *Nano Lett.* **2008**, *8* (7), 2082–2086. https://doi.org/10.1021/nl080452q.

(262) Bayer, B. C.; Bosworth, D. A.; Michaelis, F. B.; Blume, R.; Habler, G.; Abart, R.; Weatherup, R. S.; Kidambi, P. R.; Baumberg, J. J.; Knop-Gericke, A.; Schloegl, R.; Baehtz, C.; Barber, Z. H.; Meyer, J. C.; Hofmann, S. In Situ Observations of Phase Transitions in Metastable Nickel (Carbide)/Carbon Nanocomposites. *J. Phys. Chem. C* **2016**, *120* (39), 22571–22584. https://doi.org/10.1021/acs.jpcc.6b01555.

(263) Lin, P. A.; Gomez-Ballesteros, J. L.; Burgos, J. C.; Balbuena, P. B.; Natarajan, B.; Sharma, R. Direct Evidence of Atomic-Scale Structural Fluctuations in Catalyst Nanoparticles. *Journal of Catalysis* **2017**, *349*, 149–155. https://doi.org/10.1016/j.jcat.2017.03.009.

(264) Dembélé, K.; Bahri, M.; Melinte, G.; Hirlimann, C.; Berliet, A.; Maury, S.; Gay, A.-S.; Ersen, O. Insight by In Situ Gas Electron Microscopy on the Thermal Behaviour and Surface Reactivity of Cobalt Nanoparticles. *ChemCatChem* **2018**, *10* (18), 4004–4009. https://doi.org/10.1002/cctc.201800854.

(265) Zhang, L.; He, M.; Hansen, T. W.; Kling, J.; Jiang, H.; Kauppinen, E. I.; Loiseau, A.; Wagner, J. B. Growth Termination and Multiple Nucleation of Single-Wall Carbon Nanotubes Evidenced by *in Situ* Transmission Electron Microscopy. *ACS Nano* **2017**, *11* (5), 4483–4493. https://doi.org/10.1021/acsnano.6b05941.

(266) Lobo, L. S. Catalytic Carbon Formation: Clarifying the Alternative Kinetic Routes and Defining a Kinetic Linearity for Sustained Growth Concept. *Reac Kinet Mech Cat* **2016**, *118* (2), 393–414. https://doi.org/10.1007/s11144-016-0993-x.

(267) Diaz, M. C.; Balbuena, P. B. On the Role of Surface Oxygen during Nascent Single-Walled Carbon Nanotube Cap Spreading and Tube Nucleation on Iron Catalysts. *Carbon* **2021**, *184*, 470–478. https://doi.org/10.1016/j.carbon.2021.08.049.

(268) Chao, H.-Y.; Jiang, H.; Cumings, J.; Sharma, R. *In-Situ* Measurements of Single Walled Carbon Nanotube Growth Reveal the Structures of Active and Inactive Catalyst Nanoparticles. *Microsc Microanal* **2019**, *25* (S2), 1452–1453. https://doi.org/10.1017/S1431927619007992.

(269) Dong, W.; Liu, J.; Zhu, H.; Ding, Y.; Pei, Y.; Liu, J.; Du, H.; Jiang, M.; Liu, T.; Su, H.; Li, W. Co–Co $_2$ C and Co–Co $_2$ C/AC Catalysts for Hydroformylation of 1-Hexene under Low Pressure: Experimental and Theoretical Studies. *J. Phys. Chem. C* **2014**, *118* (33), 19114–19122. https://doi.org/10.1021/jp504215y.

(270) Eres, G.; Kinkhabwala, A. A.; Cui, H.; Geohegan, D. B.; Puretzky, A. A.; Lowndes, D. H. Molecular Beam-Controlled Nucleation and Growth of Vertically Aligned Single-Wall Carbon Nanotube Arrays. *J. Phys. Chem. B* **2005**, *109* (35), 16684–16694. https://doi.org/10.1021/jp051531i.

(271) Kimura, H.; Goto, J.; Yasuda, S.; Sakurai, S.; Yumura, M.; Futaba, D. N.; Hata, K. Unexpectedly High Yield Carbon Nanotube Synthesis from Low-Activity Carbon Feedstocks at High Concentrations. *ACS Nano* **2013**, *7* (4), 3150–3157. https://doi.org/10.1021/nn305513e.

(272) Mo, Y. H.; Kibria, A. K. M. F.; Nahm, K. S. The Growth Mechanism of Carbon Nanotubes from Thermal Cracking of Acetylene over Nickel Catalyst Supported on Alumina. *Synthetic Metals* **2001**, *122* (2), 443–447. https://doi.org/10.1016/S0379-6779(00)00565-8.

(273) Ramsvik, T.; Borg, A.; Venvik, H. J.; Hansteen, F.; Kildemo, M.; Worren, T. Acetylene Chemisorption and Decomposition on the Co() Single Crystal Surface. *Surface Science* **2002**, *499* (2–3), 183–192. https://doi.org/10.1016/S0039-6028(01)01795-2.

(274) Zhang, M.; Huang, H.; Yu, Y. Insight into the Mechanism of Ethylene Decomposition Over Co(0001) Surface: Formation of Carbon Species. *Catal Lett* **2019**, *149* (3), 744–752. https://doi.org/10.1007/s10562-019-02676-z.

(275) Gong, J.; Cao, C.; Sun, R.; Cui, L.; Gao, R.; Hao, H. A DFT Insight into the Tuning Effect of Potassium Promoter on the Formation of Carbon Atoms via Carburization Gases Dissociation on Iron-Based Catalysts. *Catalysts* **2020**, *10* (5), 527. https://doi.org/10.3390/catal10050527.

(276) Ojeda, M.; Nabar, R.; Nilekar, A. U.; Ishikawa, A.; Mavrikakis, M.; Iglesia, E. CO Activation Pathways and the Mechanism of Fischer–Tropsch Synthesis. *Journal of Catalysis* **2010**, *272* (2), 287–297. https://doi.org/10.1016/j.jcat.2010.04.012.

(277) Yang, J.; Qi, Y.; Zhu, J.; Zhu, Y.-A.; Chen, D.; Holmen, A. Reaction Mechanism of CO Activation and Methane Formation on Co Fischer–Tropsch Catalyst: A Combined DFT, Transient, and Steady-State Kinetic Modeling. *Journal of Catalysis* **2013**, *308*, 37–49. https://doi.org/10.1016/j.jcat.2013.05.018.

(278) Pei, Y.-P.; Liu, J.-X.; Zhao, Y.-H.; Ding, Y.-J.; Liu, T.; Dong, W.-D.; Zhu, H.-J.; Su, H.-Y.; Yan, L.; Li, J.-L.; Li, W.-X. High Alcohols Synthesis via Fischer–Tropsch Reaction at Cobalt Metal/Carbide Interface. *ACS Catal.* **2015**, *5* (6), 3620–3624. https://doi.org/10.1021/acscatal.5b00791.

(279) Shaikjee, A.; Coville, N. J. The Synthesis, Properties and Uses of Carbon Materials with Helical Morphology. *Journal of Advanced Research* **2012**, *3* (3), 195–223. https://doi.org/10.1016/j.jare.2011.05.007.

(280) Essenhigh, K. A.; Utkin, Y. G.; Bernard, C.; Adamovich, I. V.; William Rich, J. Gas-Phase Boudouard Disproportionation Reaction between Highly Vibrationally Excited CO Molecules. *Chemical Physics* **2006**, *330* (3), 506–514. https://doi.org/10.1016/j.chemphys.2006.09.033.

(281) Bremmer, G. M.; Zacharaki, E.; Sjåstad, A. O.; Navarro, V.; Frenken, J. W. M.; Kooyman, P. J. In Situ TEM Observation of the Boudouard Reaction: Multi-Layered Graphene Formation from CO on Cobalt Nanoparticles at Atmospheric Pressure. *Faraday Discuss.* **2017**, *197*, 337–351. https://doi.org/10.1039/C6FD00185H.

(282) Peressi, M. Interaction of Carbon Monoxide with Cu Nanoclusters Grown on Alumina Surface. *Il Nuovo Cimento C* **2015**, *38* (2), 1–8. https://doi.org/10.1393/ncc/i2015-15068-3.

(283) Sauer, J.; Ugliengo, P.; Garrone, E.; Saunders, V. R. Theoretical Study of van Der Waals Complexes at Surface Sites in Comparison with the Experiment. *Chem. Rev.* **1994**, *94* (7), 2095–2160. https://doi.org/10.1021/cr00031a014.

(284) Baranek, P.; Pinarello, G.; Pisani, C.; Dovesi, R. Ab Initio Study of the Cation Vacancy at the Surface and in Bulk MgO. *Phys. Chem. Chem. Phys.* **2000**, *2* (17), 3893–3901. https://doi.org/10.1039/b003590o.

(285) Ferrari, A. M.; Pacchioni, G. Electronic Structure of F and V Centers on the MgO Surface. *J. Phys. Chem.* **1995**, *99* (46), 17010–17018. https://doi.org/10.1021/j100046a029.

(286) Kantorovich, L. N.; Holender, J. M.; Gillan, M. J. The Energetics and Electronic Structure of Defective and Irregular Surfaces on MgO. *Surface Science* **1995**, *343* (3), 221–239. https://doi.org/10.1016/0039-6028(95)00844-6.

(287) Diwald, O.; Sterrer, M.; Knözinger, E. Site Selective Hydroxylation of the MgO Surface. *Phys. Chem. Chem. Phys.* **2002**, *4* (12), 2811–2817. https://doi.org/10.1039/b110334b.

(288) Ulmann, M.; De Tacconi, N. R.; Augustynski, J. Behavior of Surface Peroxo Species in the Photoreactions at Titanium Dioxide. *J. Phys. Chem.* **1986**, *90* (24), 6523–6530. https://doi.org/10.1021/j100282a022.

(289) Tuller, H. L.; Bishop, S. R. Point Defects in Oxides: Tailoring Materials Through Defect Engineering. *Annu. Rev. Mater. Res.* **2011**, *41* (1), 369–398. https://doi.org/10.1146/annurev-matsci-062910-100442.

(290) Noda, S.; Hasegawa, K.; Sugime, H.; Kakehi, K.; Zhang, Z.; Maruyama, S.; Yamaguchi, Y. Millimeter-Thick Single-Walled Carbon Nanotube Forests: Hidden Role of Catalyst Support. *Jpn. J. Appl. Phys.* **2007**, *46* (No. 17), L399–L401. https://doi.org/10.1143/JJAP.46.L399.

APPENDIX A

SUPPLEMENTAL INFORMATION CHAPTER III

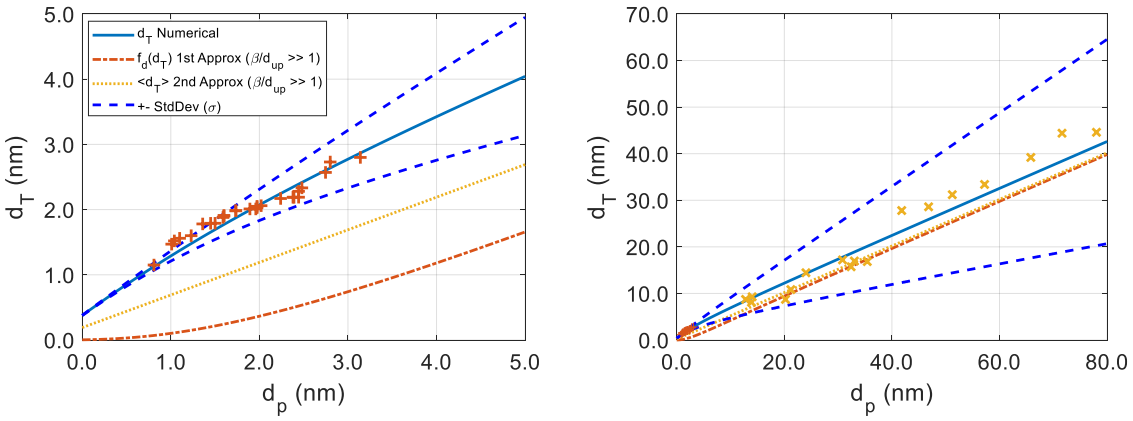

Figure A.11. Reduced functions obtained for the case ($\boldsymbol{\beta / d_{up} \gg 1}$) scenario in the dimensional analysis. Both approximations were compared against Tibbets's experimental set (Right) and Diaz et al. experimental data (Left).

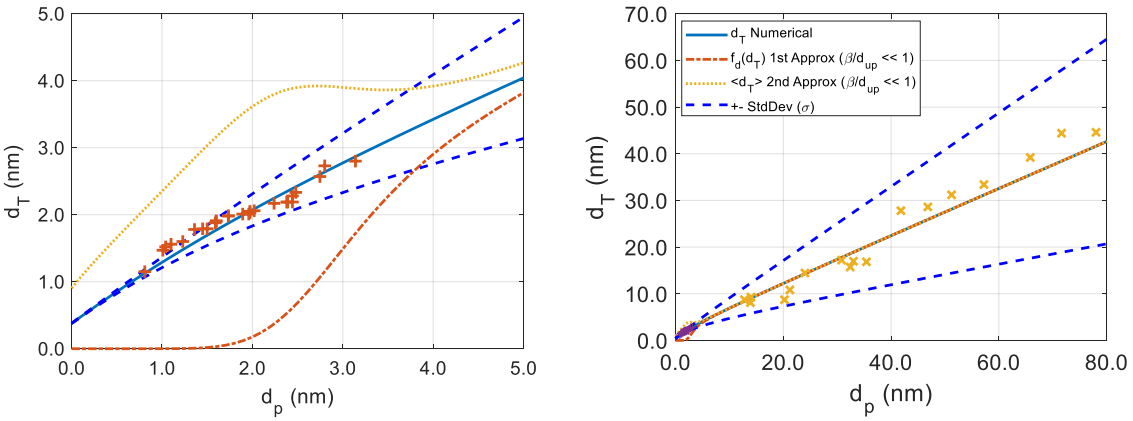

Figure A.12. Reduced functions obtained for the second case ($\boldsymbol{\beta / d_{up} \ll 1}$) scenario in the dimensional analysis. Both approximations were compared against Tibbets's experimental set (Right) and Diaz et al. experimental data (Left).

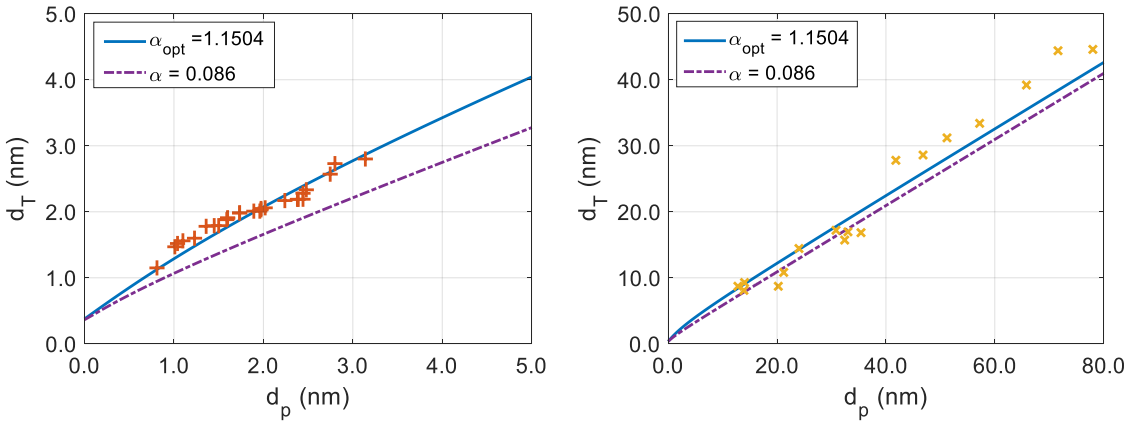

Figure A.13. Optimization of the parameter $\boldsymbol{\alpha}$. (+) High-resolution TEM experimental Data from Diaz et al[39]. (x) Data collected from Tibbets[137]. A comparison between the optimized value $\boldsymbol{\alpha_{opt}}$ and the value from Gulseren et al[181] is shown.

APPENDIX B

SUPPLEMENTAL INFORMATION CHAPTER IV

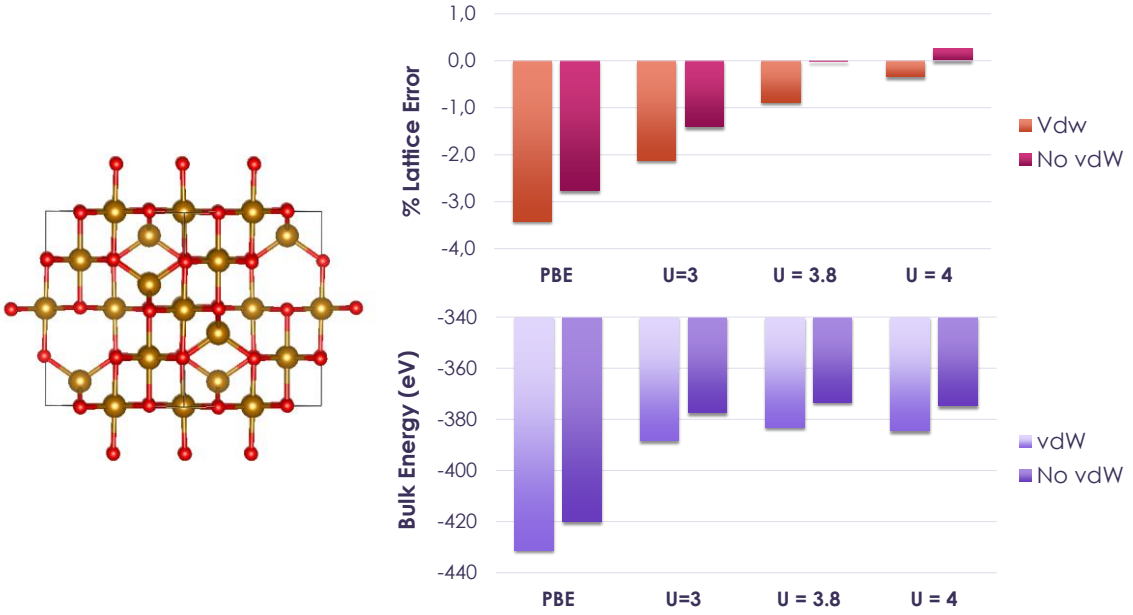

Figure B.14. Initial Calibration of the Hubbard U Parameter. [Left] Bulk structure of Iron Oxide. [Right] Lattice and Bulk energy error using different U values.

APPENDIX C

SUPPLEMENTAL INFORMATION CHAPTER V

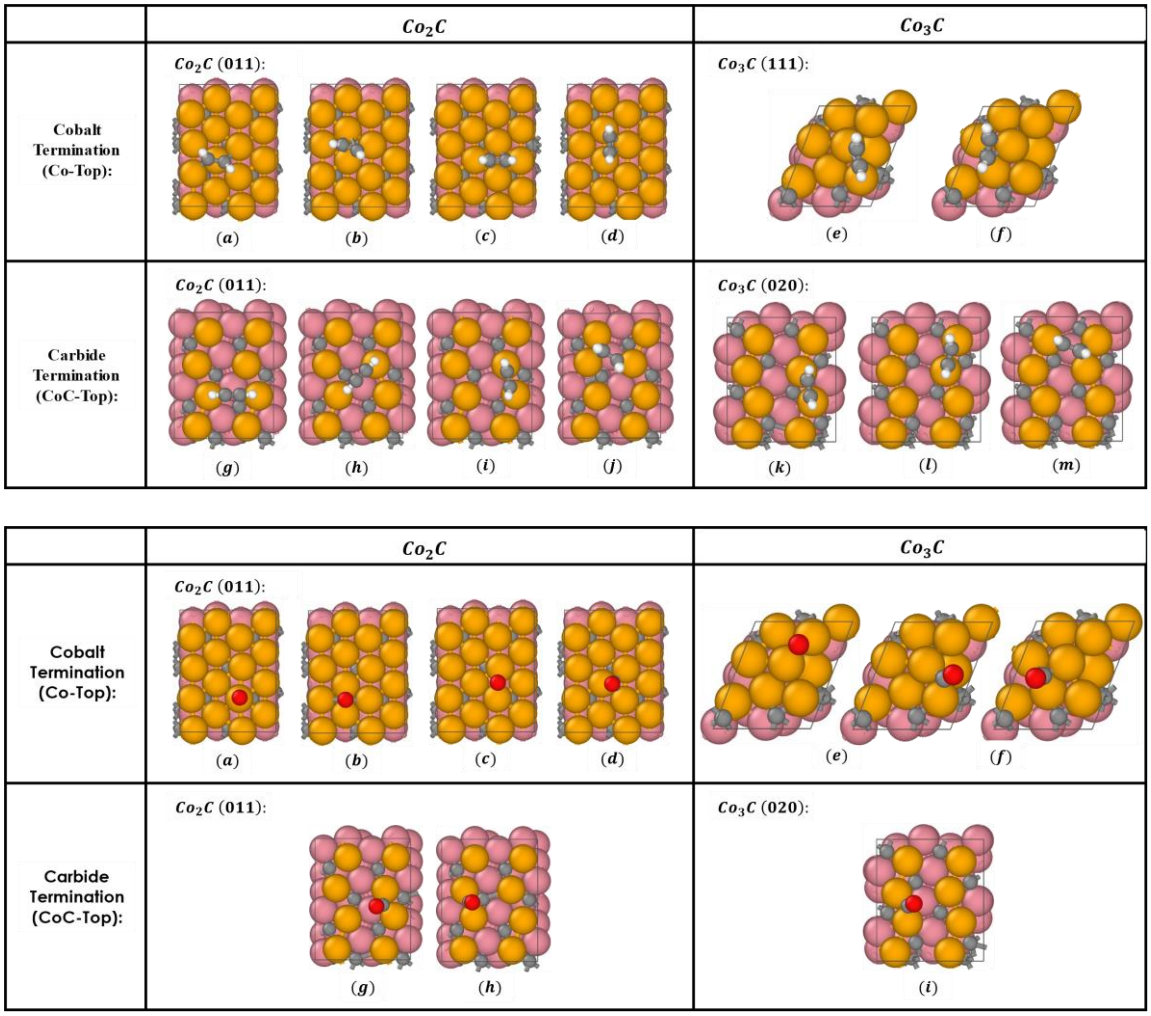

Figure C.15. Different tested adsorption sites for acetylene and CO

Positions g and h for the C_2H_2 adsorption showed the overall lower interaction energy, in fact the molecule is almost completed detached from the surface.